Institute of Mathematics and Physics

Aberystwyth University

Dynamical, Rheological and Thermal Studies of High Temperature Oxide Liquids

PhD Thesis

of

Vũ Văn Quang

Contents

Acknowledgments

I would like to thank many people who have helped me during the course of my PhD. I wish first to thank Aberystwyth University and the Daresbury laboratory for giving me both the opportunity and financial support to achieve this PhD project.

I would like to express my deep gratitude to my supervisor, Prof. Neville Greaves, for his patience, dedication, commitment, guidance, optimism and communicative scientific enthusiasm. I am extremely lucky to find a supervisor who can take on the multiple roles of editor, friend and mentor. His kindness and encouragement bring up my confidence into challenging, interesting and important fields of physics. I have received a warm welcome since the beginning from him and his wife, Jennifer Greaves, who was also my first English teacher in the UK. With her lectures (and many cups of tea), my English has improved to near comprehensibility.

I thank also all the staff at the Synchrotron Radiation Source, especially Dr. Chris Martin, for their support before, during and after the experiments. I would like to thank all my friends and colleagues from UWA. Dr. Martin Wilding is my great source of information about glasses and polyamorphism. Dr. Florian Karl with his talent in both physics and computer skills has helped me in the design of this thesis using Latex (a software that keeps me away from editing number of equation, reference and so on). Dr. Dave Langstaff who has a talent in both physics and IT, has helped me in the LabVIEW software. He also shared his interests in aerodynamic levitator experiments. Thanks to my office mate, Twilight Barnardo, for IDL code. The biggest contribution to the design of the aerodynamics levitator was made by Steve Fearn.

As I came to Aberystwyth from France, where I spent two years for my MSc, I would like to say "Merci" to all the people who contributed to my studying in France as well

as to the move from France to Wales. My thanks also go to Dr. Odile Majérus who has introduced me to this PhD proposal. Odile spent a lot of time explaining the topic to me and also the social life in Aber which she had already experienced during her postdoc course. I also learned a lot from discussions with Dr. Louis Hennet during the time in Daresbury, Grenoble, Orléans and Aberystwyth. Further back in time, my deep thanks must go to Prof. Mireille Tadjeddine who with her great help, since I was in the Hanoi University of Education, secured the scholarships for my two years in France.

My great thanks go to Dr. Chris Morrell and his family for their warm welcome since my first arrival in Aberystwyth. I have a very good time in discussing my PhD thesis with him. I appreciate that he also shares his interest in my PhD topic. I will miss his lovely kids where in "their countries" they are called William, Tom and Eddy.

I offer my special thanks to my family in Vietnam who have supported me in everything I have done with their love. Anything good that I have achieved in my 21 years as a student is no more than just to make them feel proud of me. And as I have been a lucky guy so far in my life, I have found my "Flower", Nguyen Phuong Hoa, who has been with me through all the hardest times of my PhD preparation. By the time I was able to finalise the thesis corrections, she had become my wife.

To the memory of my father

Dòng sông nhỏ mang trong mình khát vọng chở hạt muối tới đại dương…
(The smallest brook has the ambition to bring a grain of salt to the ocean)

List of Figures

List of Tables

Chapter 1

Introduction

In everyday life, we are familiar with glass. Their applications spread from uses such as lenses, prisms, mirrors for optics, windshields for cars and windows for houses, to glass fibres for telecommunications. Glass is everywhere in modern life. Traditionally, glass is made from quenching its liquid counterpart from very high temperature. Therefore, studies of glass-forming in liquid state are important in controlling and predicting the behaviour of the ensuing glass.

At Aberystwyth, an aerodynamic levitator has been designed, in combination with X-ray scattering, to study the properties of refractory oxide solids and ultrahigh temperature liquids such as alumina and yttria aluminates. This thesis focuses on the study of dynamical, rheological and thermal properties of alumina as an example to demonstrate the theory and experimental method.

Levitated solids and liquids are approximately spherical with typical diameter of around $2\,mm$. Placing the levitated sample in a synchrotron radiation X-ray beam enables X-ray scattering to be measured, both at small and wide angles. This enables the nanostructure to be measured as well as disorder in the interatomic order. In addition, the heat released from the supercooled state can be quantified from the exothermic rise measured by the pyrometer.

Viscosity and surface tension of liquids are related to the vibration of the drops under

gravity. A high-speed camera has been used to record sample images in the real time in order to characterise these vibrations. We have developed a double-piezo insertion through which the gas jet passes. The double-piezo, connected with a frequency generator, introduces the accoustic waves into the gas flow which then levitates and excites the sample vibrating simultaneously. By scanning the excited frequencies and using sample images recorded from the high-speed camera, we have measured the viscosity of liquid alumina.

The outline of this thesis is as follows. The opening chapter introduces the importance of the study glass-forming liquids and the current problems needed to be solved. **Chapter 2** covers the background into various states of matter. We give a brief review of some properties in solid (crystals and glass) and then the melting process, before going further to our main area, the liquid state of glass-forming materials. **Chapter 3** represents an overview of the experimental methods that are used to study the dynamical, rheological and thermal properties of ultrahigh temperature liquids. The emphasis of this chapter is on the aerodynamic levitator combined with X-ray scattering techniques. **Chapter 4** is primarily concerned with the measurement of rheological properties for and alumina liquid such as density and viscosity. The temperature range in the liquid state gets deeper in the supercooled liquid to the point that crystallisation occurs. Further investigation about density fluctuations in the liquid state is shown in **Chapter 5**. Thermal properties are investigated and a new method of measuring the latent heat of recalescence is represented in **Chapter 6**. The advantage of using an optical pyrometer compared to the traditional methods used in Differential Scanning Calorimetry, become obvious in the supercooled state where the crystallisation would otherwise occur at the contact of the sample and sample container. For dynamical properties, **Chapter 7** introduces the measurement of the Debye-Waller factors using the structure factors from X-ray diffraction. Finally, **Chapter 8** concludes and discusses the possible areas of new work in the future.

Chapter 2

Background

2.1 Introduction

Depending on the condition of temperature and pressure or historical process, a material can be in different states. This section takes into account a brief review of crystalline, glassy, liquid and supercooled liquid (excluding gaseous) states of matter: the difference and transition between them. They are distinguished in both atomic structural arrangement and dynamical behaviour and also in both intensive and extensive thermo-dynamic properties. Figure 2.1 shows a diagram of enthalpy (or volume) of these states versus temperature at ambient pressure.

By heating a solid up to the melting temperature, T_m (for crystal) and glass transition temperature, T_g (for glass), its liquid and supercooled liquid counterpart will be obtained. Following the order of heating then cooling process, a crystal (or glass) can reach to its liquid state and normally returns to a crystal (or glass) itself. But depending on some specific conditions during cooling, a liquid can "decide" which state (crystalline or glassy) to form. This means that a crystal can become a glass via its liquid counterpart and vice versa. When we cool a liquid, the enthalpy decrease and the constituent atoms will arrange to the structural equilibrium as at the temperature the liquid is held. Normally, when the temperature is lower than the melting temperature of crystal, T_m, the liquid will crystallize and release an amount of heat called heat of fusion. The enthalpy of system

decreases abruptly and the heat capacity is also changed. Continuing the cooling process, the enthalpy of crystal decreases but with different slope compared to that of liquid.

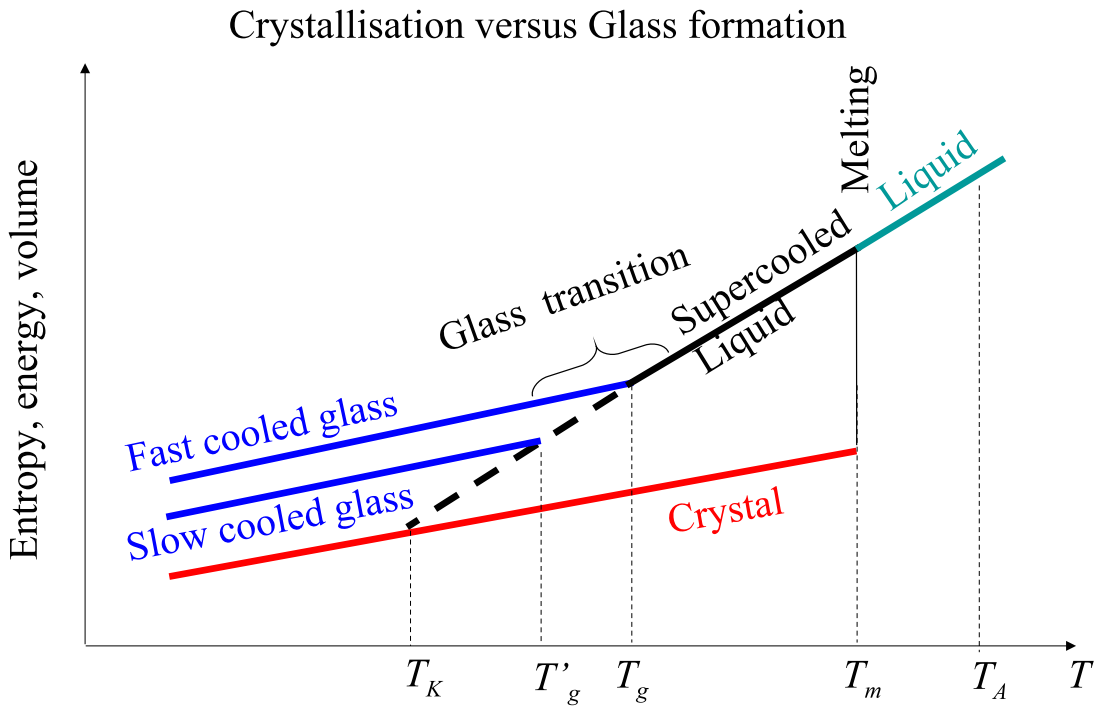

Figure 2.1: Schematics of thermo-dynamic properties as potential energy, configurational entropy and volume as a function of temperature for the liquids, supercooled liquid, glassy and crystalline states.

If the sample does not crystallize at melting temperature, T_m, it will remain in the state called supercooled liquid. It becomes more viscous as the temperature decreases. The time that atoms achieve a new equilibrium at new temperature gets longer. In some cases, this time is as long as the experimental time available. If the vitrification process is unsuccessful due to the nucleation, the supercooled liquid will release an amount of latent heat called the heat of fusion and crystallize. When the recrystallization is very rapid, light will be emitted on reheating. This process is called recalescence. If this is

slow, the melt will crystallise at T_m with an abrupt change in volume. However, when it is sufficiently rapid, the liquid melt passes through T_m to the supercooled liquid state and a glass might be created at T_g. The value T_g is not well defined depending on the variable rate of cooling: the faster cooling rate produces the higher T_g and vice versa. This process is called vitrification. Neither the transition from supercooled liquid to glass nor the transition from glass to supercooled liquid displays the sharpness characteristic of crystal melting. When the cooling rate is sufficiently low and the crystallization is still avoided, the excess energy of glass compared to crystal is also reduced. In this case a glass with lower configuration entropy can be obtained at lower glass transition temperature (figure 2.1). The lowest glass transition temperature, where the excess energy vanishes, is predicted to be Kauzemann temperature, T_K, [18].

2.2 Solids

2.2.1 Crystal structure

The word "crystal" comes from Greek (*krustallas*) and means "solidified by the cold". However this meaning does not cover whole geometry and dynamical properties of the crystal. Geome-trically, crystal is a solid where the constituent atoms, molecules or ions are packed in regular order and in all three spatial dimensions. It can be built by repeating a certain unit of pattern called unit cell. The triple periodicity is a fundamental property of a crystal. Any crystal could be generated by repeating its unit cells through translations of a certain lattice called the *direct* lattice. Figure 2.2 illustrates the structure of a crystal in two dimensions. All constituent atoms are in periodical arrangement.

Crystals are characterized by the kind of their unit cell including the position of atoms within the unit cell and their space symmetry. Depending on the arrangement of the atoms within the unit cell, we can distinguish primitive (P), face centered (F), body centered

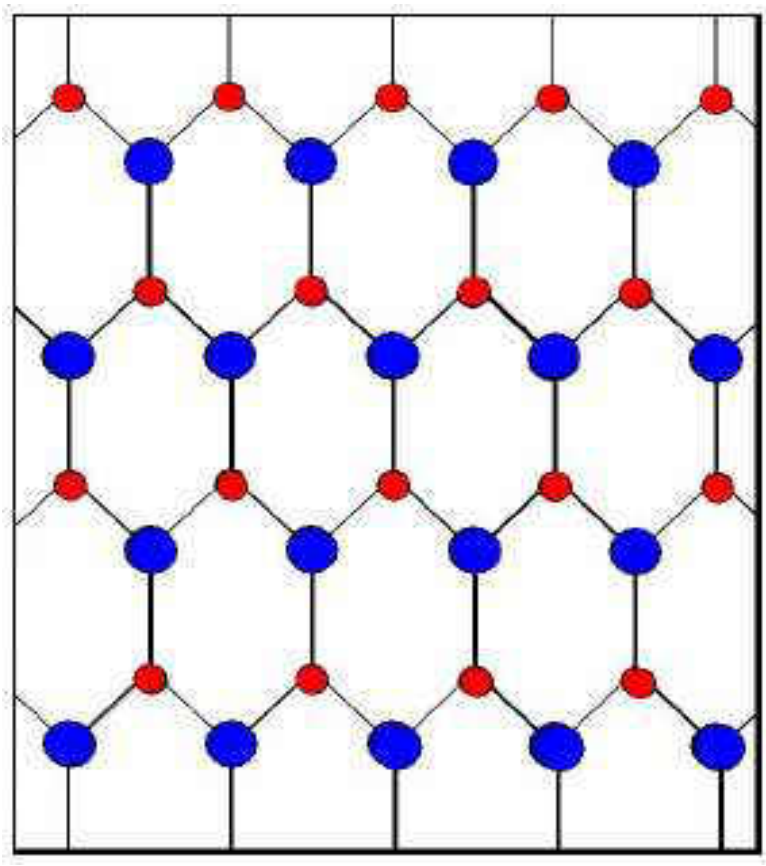

Figure 2.2: Crystalline structure in 2 dimensions of a diatomic crystal

(I), or rhombohedral (R) crystal lattice types. The combination of these crystal types and systems gives rise to the 14 Bravais lattices. The space symmetry is coupled giving 230 possible space groups. There are seven crystal systems that are listed in table 2.1

2.2.2 Reciprocal space and X-ray crystallography

To describe the morphology of a crystal, the simplest way is to associate, with each set of lattice planes parallel to a natural face of crystal, a vector drawn from a given origin and normal to these corresponding lattice planes. To complete the description it is sufficient to give to each vector a length related to the spacing between these lattice planes. This polar diagram (origin and vector) is the geometric basic for the so-called reciprocal lattice. On the other hand, the essential tool to study a crystal is the diffraction of a wave with a

Crystal System	Unit cell parameters	Space lattice	Essential symmetry
Cubic	a=b=c; $\alpha = \beta = \gamma = 90\,^\circ$	P F I	4 three-fold axis
Rhombohedra	a=b=c; $\alpha = \beta = \gamma \neq 90\,^\circ$	P	1 three-fold axis
Orthorhombic	$a \neq b \neq c$; $\alpha = \beta = \gamma = 120\,^\circ$	P F I C	3 three-fold axis
Tetragonal	$a = b \neq c$; $\alpha = \beta = \gamma = 90\,^\circ$	P I	1 four-fold axis
Hexagonal	$a = b \neq c$; $\alpha = \beta = 90\,^\circ; \gamma = 120\,^\circ$	P	1 six-fold axis
Monoclinic	$a \neq b \neq c; \alpha = \beta = 90\,^\circ$; $\gamma = 120\,^\circ$	P C	1 two-fold axis
Triclinic	$a \neq b \neq c; \alpha \neq \beta \neq \gamma \neq 90\,^\circ$	P	None

Table 2.1: Seven crystal systems with the corresponding essential symmetry elements and possible space lattice group

wavelength of the same order of magnitude to that of the lattice spacing. The diffraction spots are associated to the nodes of reciprocal lattice. It is also the lattice in which vibrational, electronic and magnetic properties are considered.

Reciprocal lattice is directly related to real lattice, i.e. we could build a reciprocal lattice ($\mathbf{a}^*$, $\mathbf{b}^*$, $\mathbf{c}^*$) from a real lattice ($\boldsymbol{a}$, $\boldsymbol{b}$, $\boldsymbol{c}$) and vice versa. Thus we have the relation between these primitive vectors of two lattices:

$$\mathbf{a}^* = 2\pi \frac{\mathbf{b} \wedge \mathbf{c}}{\mathbf{a}(\mathbf{b} \wedge \mathbf{c})} \quad \mathbf{b}^* = 2\pi \frac{\mathbf{c} \wedge \mathbf{a}}{\mathbf{b}(\mathbf{c} \wedge \mathbf{a})} \quad \mathbf{c}^* = 2\pi \frac{\mathbf{a} \wedge \mathbf{b}}{\mathbf{c}(\mathbf{a} \wedge \mathbf{b})} \tag{2.1}$$

Note that $\mathbf{a}(\mathbf{b} \wedge \mathbf{c})$ is the volume of the primitive unit cell in real lattice, so the units of $\mathbf{a}^*$, $\mathbf{b}^*$ and $\mathbf{c}^*$ are inverse distance, typically Å^{-1}. In solid state physics, reciprocal lattice is often referred to as Fourier Space. Each reciprocal lattice point is connected to the origin by a reciprocal lattice vector, $\boldsymbol{G}$, where

$$\mathbf{G} = h\mathbf{a}^* + k\mathbf{b}^* + l\mathbf{c}^* \tag{2.2}$$

and h, k, l are integers.

By definition, we have also the following relations:

$$\mathbf{a}\mathbf{a}^* = 2\pi \frac{(\mathbf{b} \wedge \mathbf{c})\mathbf{a}}{\mathbf{a}(\mathbf{b} \wedge \mathbf{c})} = 2\pi; \ \mathbf{b}\mathbf{b}^* = \mathbf{c}\mathbf{c}^* = 2\pi \tag{2.3}$$

$$\mathbf{a}^*\mathbf{b} = 2\pi \frac{(\mathbf{b} \wedge \mathbf{c})\mathbf{b}}{\mathbf{a}(\mathbf{b} \wedge \mathbf{c})} = 0; \ \mathbf{a}^*\mathbf{c} = \mathbf{b}^*\mathbf{a} \ldots = 0 \tag{2.4}$$

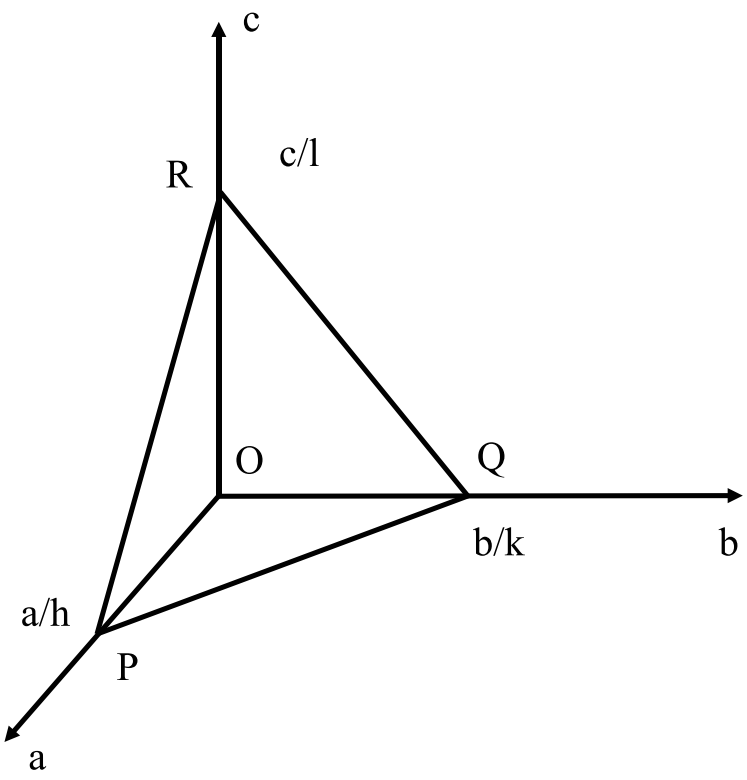

Figure 2.3: The indexing of crystal faces and plans

Hence $\mathbf{a}^*$ is perpendicular to $\boldsymbol{b}$ and $\boldsymbol{c}$, $\mathbf{b}^*$ is perpendicular to $\boldsymbol{c}$ and $\boldsymbol{a}$, and $\mathbf{c}^*$ is perpendicular to $\boldsymbol{a}$ and $\boldsymbol{b}$. Reciprocal lattice has some other properties such as:

- The reciprocal lattice of the reciprocal lattice is the direct lattice
- The direct lattice is used to describe the atomic positions in the crystal; the reciprocal lattice is used to describe the position of the diffracted peaks. Hence, a diffraction pattern of a crystal is a map of its reciprocal lattice.
- When the crystal rotates, both direct and reciprocal lattice rotate in the same way.
- The length of the reciprocal lattice vector, $|\boldsymbol{G}|$, is equal to 2 divided by the interplanar distance d_{hkl} for net planes (hkl): $|\boldsymbol{G}| = 2 \,/\, d_{hkl}$.

The various lattice planes are classified using Miller indices. The definition of the Miller indices is determined by the magnitude of a, b and c at the point of interception of the lattice plane. Figure 2.3 illustrates a lattice plane cutting through the three axes (a, b and c). the intercepts OP, OQ and OR can be defined as fractions of a/h, b/k and c/l of the lengths of the axes. Hence the Miller index for the plane is given as (hkl).

In an X-ray diffraction experiment, from the separation of the diffraction peaks, it is possible to deduce the spacing between lines on the grating; their structure can also be obtained by measurement of the relative intensities of the diffraction peaks. The minimum separating spaces between these lines, however, is limited by the wavelength of diffraction wave (approximately larger than half of the wavelength). The wavelength of X-rays is typically 1 Å, comparable to the interatomic distances in solids. Similarly, X-ray diffraction peaks provide information about the size of the unit cell and their relative intensities can be used to determine the atomic structural arrangement within the unit cell.

2.2.3 Glass structure

Traditionally, glass can be understood as a frozen liquid whose entropy is reduced in a manner that it does not crystallize. That means that the structural rearrangement falls out of equilibrium. Compared to a crystal, a glass possesses a greater energy stored in its structure. The bond-lengths and bond-angles are modified such that the long-range periodicity is nonexistent. For covalently bonded network such as silica glasses, the Continuous Random Network (CRN) model is useful to describe their structure [1]. In this model, constituent atoms link with each other and form continuous rings of different sizes surrounding hollow spaces. For modified glasses such as alkali, alkaline earth-silicate, the Modified Random Network (MRN) [2] is however more suitable in describing them.

Continuous Random Network: Figure 2.4 represents an example of a binary glassy

system in 2 dimensions. In the case of SiO_2 glasses, each Si atom (small dot) is bonded with four O atoms and each O atom (large dot) is bonded with two Si atoms. The fourth bond of Si can be imaged as out of this 2D picture plan. The linked atoms make an empty circle that represents hollow spaces.

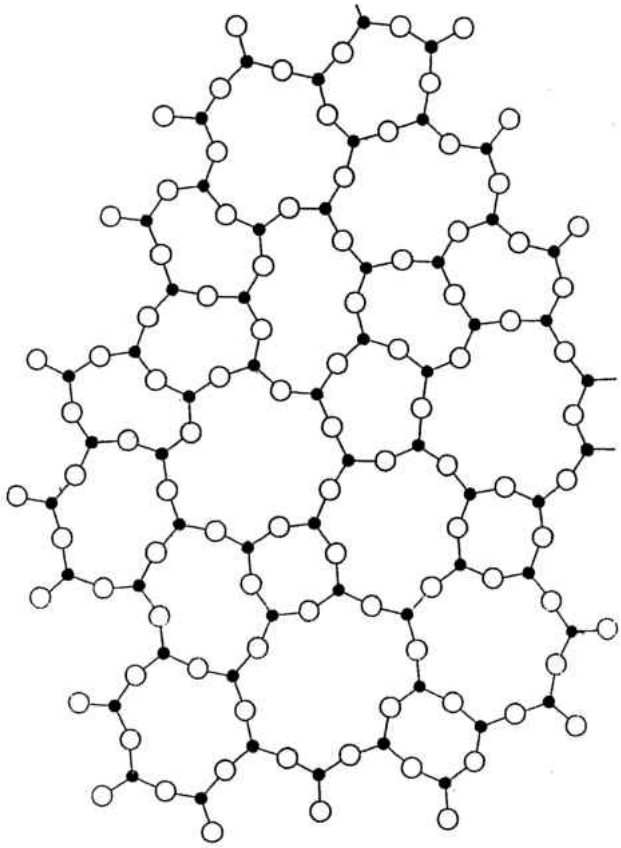

Figure 2.4: Continuous random network (CRN) in glassy structure according to the rules of Zachariasen [1]

Modified Random Network: The so-called network-forming cation, such as alkalis, alkaline-earth ions, is given for cations like Si which in association with oxygen form the CRN. The connectivity of the oxide network is disrupted, therefore "non-bridging" oxygens, that are linked to only one network-forming cations, are created. The Modified Random Network (MRN) of Greaves [2] is based on the different sizes of network-forming and network-modifying polyhedra that are measured, and results in the network and mod-

ifier components being microsegregated, with the modifier ions forming channels within a depolymerised network structure as shown in figure 2.5.

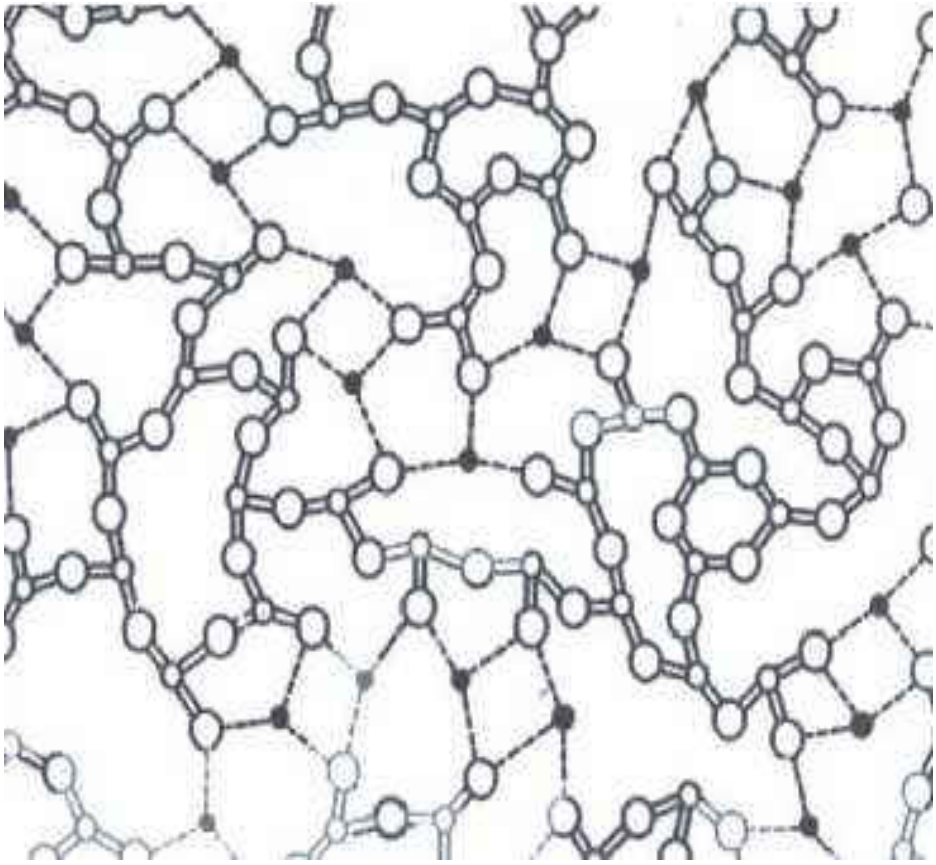

Figure 2.5: Modified random network model for the structure of a modified silicate glass [2]

2.3 Dynamics in solids and melting

2.3.1 Specific heat of solid by Dulong-Petit and by Einstein Model

From the classical point of view, the energy of a vibrating atom of mass m includes its potential and kinetic energy:

$$E_1 = \frac{1}{2}mv_x^2 + \frac{1}{2}mv_y^2 + \frac{1}{2}mv_z^2 + \frac{1}{2}kx^2 + \frac{1}{2}ky^2 + \frac{1}{2}kz^2 \qquad (2.5)$$

After the classical statistical mechanics-equipartition theorem, in thermal equilibrium

each quadratic term in E_1 has an average energy $\frac{1}{2}k_BT$, so the average energy of an atom $\bar{E_1} = 3k_BT$. For a solid which contains N atoms, the energy of solid will be $E = 3Nk_BT$ or $3N_Ak_BT$ for a mole. The specific heat at constant volume per mole is:

$$C_V = \left(\frac{\partial E}{\partial T}\right)_V = 3N_Ak_B \approx 25Jmol^{-1}K^{-1} \tag{2.6}$$

This law of Dulong-Petite is approximately obeyed by most solids at high temperature. However, by the Middle of 19^{th} century, it was clear that $C_V \to 0$ as $T \to 0\,\mathrm{K}$ for solids.

The energy of a harmonic oscillator (or a lattice mode) of angular frequency ω and at temperature T, in the viewpoint of quantum physics, is given by:

$$\bar{\epsilon} = \sum_n p_n\epsilon_n \tag{2.7}$$

where ϵ_n is an energy level of the oscillator,$\epsilon_n = (n + \frac{1}{2})\hbar\omega$, and p_n is the occupation of energy level n (probability of the oscillator being in this level) as given by the Boltzmann factor.

$$\bar{\epsilon} = \frac{\sum_n (n + \frac{1}{2})\hbar\omega \exp\left[-(n + \frac{1}{2})\hbar\omega/k_BT\right]}{\sum_n \exp\left[-(n + \frac{1}{2})\hbar\omega/k_BT\right]} \tag{2.8}$$

A neat way to calculate this function is to note it in form:

$$\bar{\epsilon} = k_BT^2\frac{1}{T}\frac{\partial Z}{\partial T} \tag{2.9}$$

where

$$\begin{aligned} Z &= \textstyle\sum_n \exp\left[-(n + \frac{1}{2})\hbar\omega/k_BT\right] \\ &= e^{\hbar\omega/2k_BT}(1 + e^{-\hbar\omega/2k_BT} + e^{-2\hbar\omega/2k_BT} + ...) \\ Z &= e^{\hbar\omega/2k_BT}(1 - e^{-\hbar\omega/2k_BT})^{-1} \end{aligned} \tag{2.10}$$

Inserting equation 2.10 into equation 2.9 , the energy of a harmonic oscillator is:

$$\bar{\epsilon} = \frac{1}{2}\hbar\omega + \frac{\hbar\omega}{e^{-\hbar\omega/k_BT} - 1} \tag{2.11}$$

The first term is the energy of zero point and second term includes the temperature. The heat capacity of a harmonic oscillator is derived from equation 2.11:

$$C_V = \frac{d\bar{\epsilon}}{dT} = k^B(\frac{\hbar\omega}{k_BT})^2\frac{e^{\hbar\omega/2k_BT}}{(e^{\hbar\omega/2k_BT}-1)^2} \tag{2.12}$$

The application of quantum theory in calculating the specific heat of solids was due to A. Einstein [3]. He made a simplifying assumption that all $3N$ vibrational modes of a three-dimensional solid of N atoms had the same angular frequency. So the specific heat of whole solid is $3N$ time of equation 2.12. The model gives the correct limit at high temperature ($\hbar\omega/k_BT << 1$), a value of heat capacity $3Nk_B$ (=$3R$ for a mole of solid as found empirically by Dulong and Petit). It also shows that the heat capacity tends to zero as $T \rightarrow 0K$, but at the temperature near $T = 0K$ it did not agree with the experiments. The experimental result in figure 2.6 shows that the value of specific heat calculated from the Einstein model tends to zero quicker than that in the experimental measurement. This can be corrected in the Debye model.

2.3.2 Specific heat by Debye model

We now take into account the distribution of vibration frequencies in a solid. The energy of lattice vibrations is obtained by integrating the energy of a single oscillator over the distribution of vibrational frequencies:

$$E = \int_0^\infty \left(\frac{1}{2}\hbar\omega + \frac{\hbar\omega}{e^{\hbar\omega/k_BT}-1}\right) g(\omega)d\omega \tag{2.13}$$

The number of modes dn found in the interval between (ω, k) and $(\omega + d\omega, k + dk)$ is $dn = g(\omega)d\omega = g(k)dk$. We will first find this by examining the allowed values of k then we will be able to calculate a value of $g(\omega)$ for the Debye model and evaluate the specific heat.

$$g(\omega) = \frac{V\omega^2}{2\pi^2 v_s^3} \tag{2.14}$$

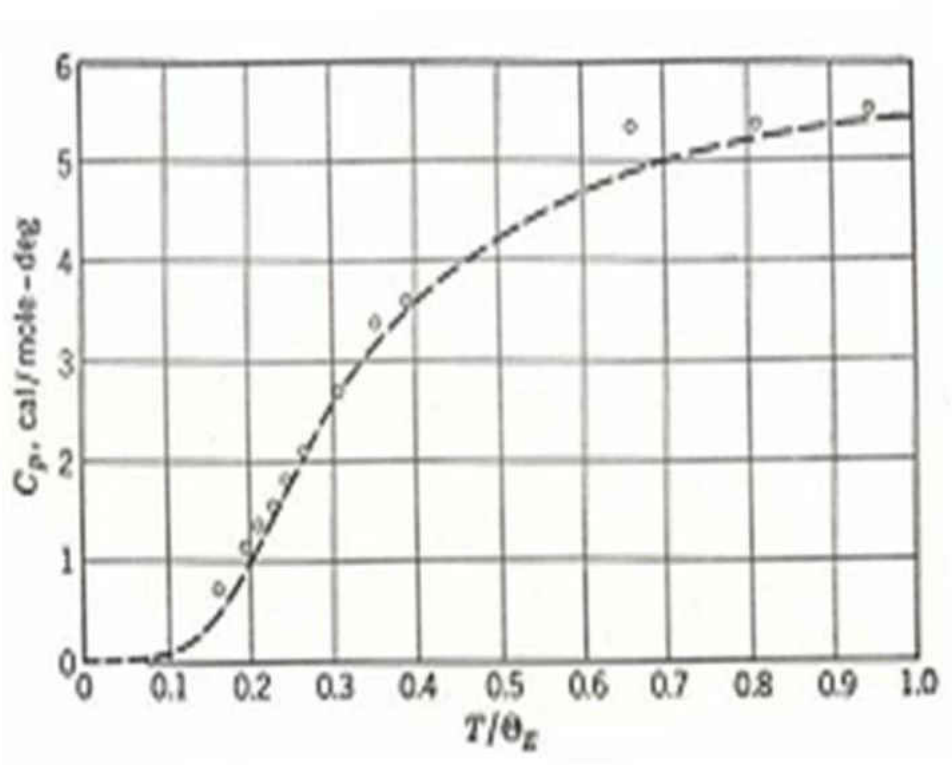

Figure 2.6: Comparison of experimental values of the specific heat of diamond and values calculated on the Einstein model using [3]

where v_s depends on the direction of propagation so that we must regard the factor $1/v_s^3$ as an average over all directions.

Since there are N atoms in the solid, there are N unique vibrational modes for each polarization. For three polarizations, that requires:

$$\int_0^{\omega_{max}} g(\omega)d\omega = 3N\frac{V}{2\pi^2 v_s^3}\int_0^{\omega_{max}} \omega^2 d\omega = 3N\frac{V}{2\pi^2 v_s^3} = \frac{9N}{\omega_{max}^3} \tag{2.15}$$

$$\omega_{max} = v_s\left(\frac{18\pi^2 N}{V}\right)^{1/3} = \omega_D \tag{2.16}$$

ω_D is the Debye cut-off frequency. Inserting the density of state of the equation 2.16 into the equation 2.13 for the energy of lattice vibrations gives:

$$E = \frac{V}{2\pi^2 v_s^3}\int_0^{\omega_D}\left(\frac{1}{2}\hbar\omega + \frac{\hbar\omega}{e^{\hbar\omega/k_B T}-1}\right)\omega^2 d\omega \tag{2.17}$$

$$E = \frac{9}{8}N\hbar\omega_D + \frac{9N}{\omega_D^3}\int_0^{\omega_D} \frac{\hbar\omega^3 d\omega}{e^{\hbar\omega/k_BT-1}} \tag{2.18}$$

We introduce the variable $x = \Theta_D/T$ where $\Theta_D = \hbar\omega/k_B$ is the Debye temperature, the heat capacity is obtained by differentiating equation 2.18 with respect to temperature:

$$C_V = 9Nk_B\left(\frac{T}{\Theta_D}\right)^3 \int_0^{\Theta_D/T} \frac{x^4 e^x dx}{(e^x-1)^2} \tag{2.19}$$

This expression agrees with the experiment at low temperature in figure 2.6

2.3.3 Lindemann's law

For the harmonic oscillators in the Debye model, there is a mean square displacement for vibration around the averaged position of the average atom [19]:

$$< \mu^2 >= 9T\hbar^2/k_B\bar{m}\Theta_D^2 \tag{2.20}$$

where k_B is Boltzmann constant, Θ_D is the Debye temperature that relates to the molar volume, V, and speed of sound v_l (longitudinal) and v_t (transverse), namely:

$$\Theta_D = \frac{h}{k_B}\left\{\frac{4\pi V}{9}\left(\frac{1}{v_l^3}+\frac{2}{v_t^3}\right)\right\}^{-1/3} \tag{2.21}$$

Since V increases and v_l, v_t decrease with temperature, the Debye temperature Θ_D always decreases as temperature rises (equation 2.21). As the result $< \mu^2 >$ increases with temperature (equation 2.20).

In the Debye model, the average interatomic distance $\bar{r}$ is directly related to the molar volume which is, in alumina, for example:

$$\bar{r} = \left(\frac{V}{5N_A}\right)^{1/3} \tag{2.22}$$

where N_A is the Avogadro number. Formally simple crystalline solids, the ratio $< \mu^2 > /\bar{r} \approx 10\%$ at the melting point. This is referred to as Lindemann's law [20, 19].

2.4 Molten and supercooled liquids of glass-forming materials

2.4.1 Viscosity and fragility

In the very high temperature regime the liquid melt is ergodic (its physical properties are independent of the historical process). The constituent atoms are completely in random arrangement and freely diffused. A liquid becomes more viscous with decreasing of temperature and the glass is the limit of this process. From Maxwell's theory [10], [14] the viscosity of liquid, η, is related to the infinite frequency (instantaneous) modulus, G_{HF} , and relaxation time, τ, through the equation: $\eta = G_{HF}\tau$. At very high temperatures, the viscosity tends to converge to the value $10^{-5}\,Pas$ which corresponds to structural relaxation times of $10\,fs$ equivalent to phonon frequencies of around $10^{14}\,Hz$. Formally, the viscosity is defined as $10^{12}\,Pas$ at glass transition temperature, T_g. The viscosity of strong liquids have an Arrhenius relation to temperature (i.e. $\log\eta$ versus $1/T$ is aprroximate to a straight line). Fragile liquids show dramatic changes in viscosity with respect to the temperature-the slope of $\log\eta$ versus $1/T$ increasing rapidly as the glass transition is approached (figure 2.7).

From the Angell plot (figure 2.7), compared to the strong liquid, the fragile liquid has a greater change in its viscosity when approaching the glass transition temperature, T_g. This change can be seen as the slope variation of viscosity-temperature curve near T_g. It is quantified by an index called kinetic fragility, m, which is defined as:

$$m = lim_{T \to T_g} \frac{d(log\eta)}{d(T_g/T)} \tag{2.23}$$

Figure 2.7 also represents a wide range of glass-forming liquid fragility from strong liquids like silica ($m \approx 20$) to fragile liquids like metal halides ($m \approx 200$). The relation between kinetic fragility in glass-forming liquids with the rigidity and vibrational proper-

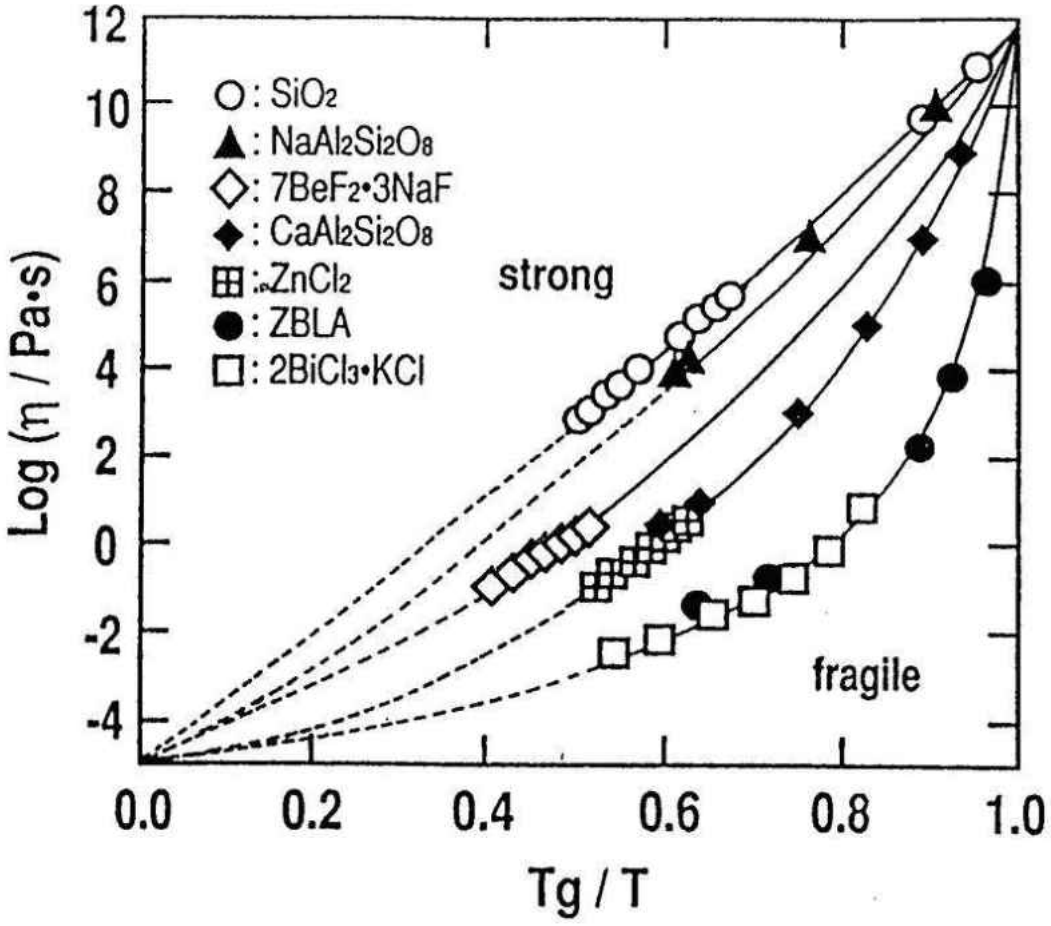

Figure 2.7: Angel plot of logarithm of liquid viscosity, $\eta/Pa.s$, of wide range strong and fragile glass-forming liquids as a function of temperature scaled to the glass transition temperature T_g [4]

ties in corresponding glass is discussed later. It is also necessary to distinguish the kinetic and thermo-dynamic fragility which has similar equation:

$$n = lim_{T \to T_g} \frac{d(logS)}{d(T_g/T)} \tag{2.24}$$

where $S = S_{ex}(T)/S_{ex}(Tg)$ and S_{ex} is the excess entropy of glass-forming liquid with respect to the corresponding crystal (figure 2.1). In term of potential energy landscape, the kinetic fragility, m, relates to the number of minima, i.e. there are more structural configurations in a fragile liquid (figure 2.8). The potential energy is a function of particle coordinates. For a system of N particles the number of minima is fewer than $3N+1$, the

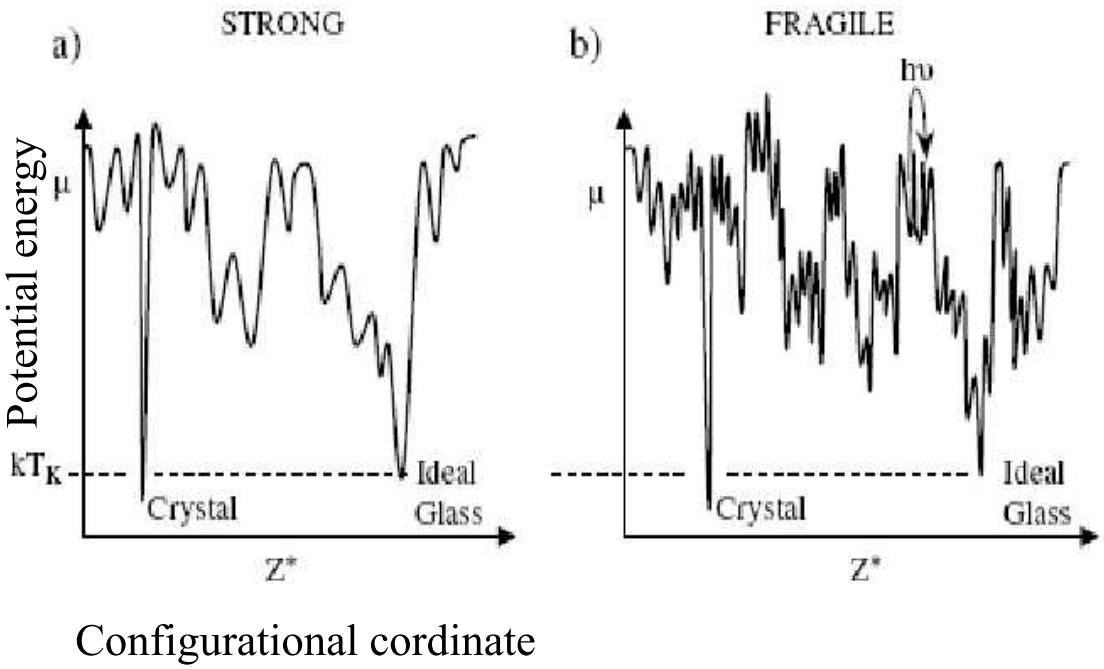

Figure 2.8: Energy landscape for strong and fragile liquids. The vertical axe is the potential energy and the horizontal is configurational cordinate (Z^*) of all atoms. The ideal glass is to be of similar energy to the corresponding crystal. Liquids are distinguished by the curvature of the energy landscape, fragile liquids having shaper minima than strong liquids.

possibilities of structural configurations. When glass-forming liquid is cooled relatively rapid, due to the lack of the thermal of vibrational energy required to activate the system to a deeper minimum, it will get trapped in a local minimum. If the cooling process is sufficiently slow, the system might occupy the deepest minimum but not crystallize and form an ideal glass where the configurational entropy vanishes. The glasses have greater entropy than the crystals and appear as metastable in the energy landscape. The thermodynamic fragility, n, represents the variation in the heights of activation energy barriers between these minima. Compared to the fragile liquid, the strong liquid gets broader minima.

2.4.2 Density fluctuations

Glasses, in the traditional way of forming, result from quenching their counterpart liquids. Therefore, they can contain some levels of local fluctuating which are either density fluctuations, or composition fluctuations, or both. In the current studies of oxide liquids such as alumina and yttrium-aluminates, we focus on the density fluctuations of oxide liquids. Figure 2.9 represents a simulating result of density fluctuation in Y_2O_3- Al_2O_3 (AY20) glass [54]. The cell volume V of AY20 liquid fluctuating as a function of time above the melting point at 2400 K. ΔV is indicated, bounded by ± 2 standard deviations (dash line). The density contrast $\Delta\rho/\rho$. is ≈ 0.025 which is similar to the experimental value reported for density fluctuations frozen in to silica glass [52].

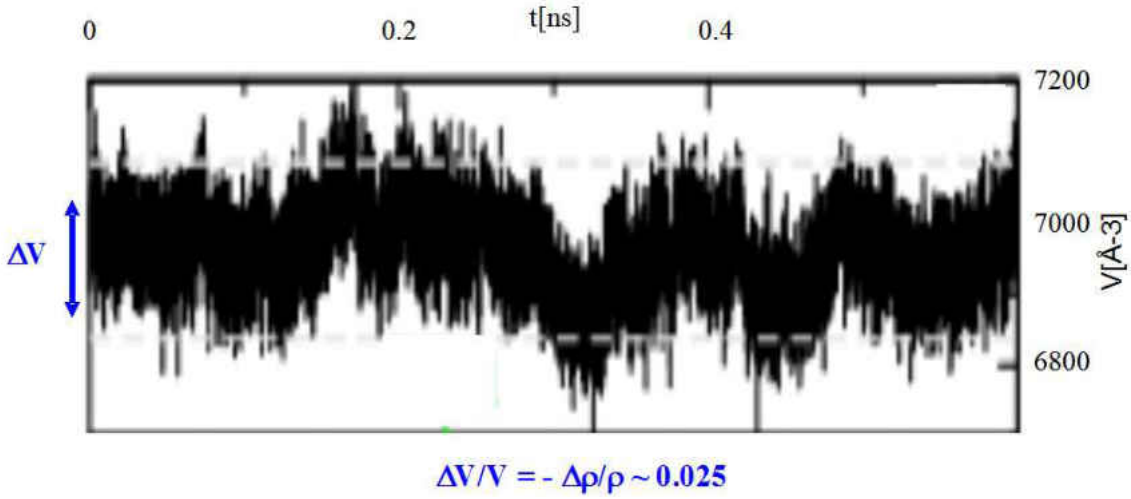

Figure 2.9: Random volume fluctuations observed for an AY20 of the whole cell volume for a short (0.6 ns) section of the whole molecular dynamics simulation at 2400 K. The light dashed curves show the locations of the volumes two standard deviations away from the mean volume. Reproduced with permission from [54]

In any system, the local density ρ of material is not uniform on a microscopic scale but contains a small derivation, ρ_0 relative to the average density, $\Delta\rho$.

$$\rho = \rho_0 + \Delta\rho \tag{2.25}$$

This inhomogeneity is necessary in maintaining the equilibrium process and the mean

square value of the fluctuations is obtained from thermodynamics [21]:

$$< \Delta\rho^2 >= \frac{\rho_0^2 k_B T}{V} K_T \tag{2.26}$$

where V is the average volume of fluctuating elements, k_B is Boltzman's constant, T is the absolute temperature, and K_T is the isothermal compressibility. If K_T is known, the fluctuation level present in the liquid at a given temperature can be evaluated. The fluc-

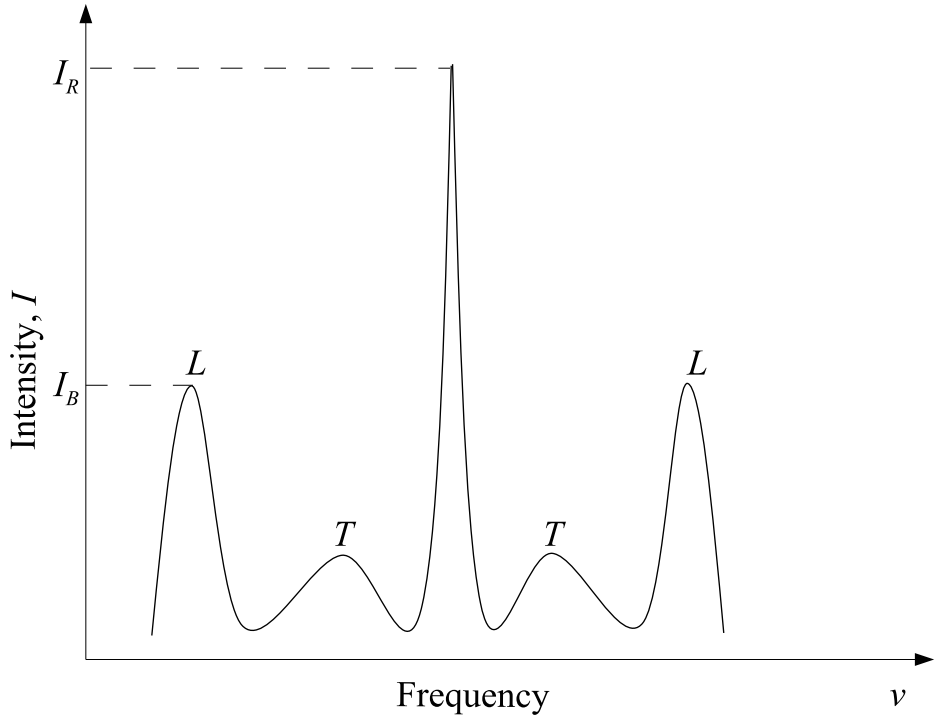

Figure 2.10: Brillouin scattering spectrum (schematic), ν_0 is the Rayleigh frequency; (L), (T) are Brillouin lines due to longitudinal and transverse phonons respectively.

tuating level can be evaluated from Brillouin scattering and small-angle X-rays scattering (SAXS). In measurements of light scattering, the specimen is illuminated by monochromatic light polarised perpendicular to the scattering plane. The schematic of Brillouin scattering spectrum is shown in figure 2.10. The Landau-Placzeck ratio, R_{LP}, is constituted by the scattered intensities between Rayleigh I_R and Brillouin I_B intensities:

$$R_{LP} = \frac{I_R}{I_B} \tag{2.27}$$

and the fluctuation level can be obtained:

$$V < \Delta\rho^2 > /\rho_0^2 = (1 + R_{LP})\frac{kT}{\rho_0 \nu^2} \tag{2.28}$$

where ν is the speed of sound.

Measurements by Schroeder [22] for vitreous SiO_2 at $T = 300\,\mathrm{K}$ provide $R_{LP} = 23.3$, $\nu = 5.92\ 10^5 cms^{-1}$ which gives $V < \Delta\rho^2 > /\rho_0^2 = 1.29\ 10^{-24} cm^3$. For a 20 Å cube, the preceding value corresponds to a relative variation: $\sqrt[2]{< \Delta\rho^2 >}/\rho_0 = 0.012$ or 1.2%.

In SAXS, the scattered intensity I_0 extrapolated to zero scattering angle is:

$$I_0 = \frac{V}{N} < \rho_e^2 > \tag{2.29}$$

where $< \rho_e^2 >$ is the mean squared variation of the average electron density, N is the number of scattering unit in a volume V. The electron density is also the usual density, therefore:

$$V \left\langle \Delta\rho^2 \right\rangle / \rho_o^2 = S(0)/\rho_o = I(0)/ \left(\rho_o \sum_{\alpha}^{N} W_{\alpha\beta\ldots}^2 \right) \tag{2.30}$$

where $\sum_{\alpha}^{N} W_{\alpha\beta\ldots}^2$ is the average cross-section for the different atoms present weighted according to the composition [14].

Chapter 3

Experimental Methods

3.1 Introduction

Studies of the liquid state are of obvious fundamental interest and are also important in technological applications since the supercooled and molten liquid are essential stages in various industrial processes (glass forming, single crystal growing, steel making, etc). Most physical properties of materials in the liquid state are related to their structure and dynamics at atomic scale. Thus it is important to develop experiments that probe the local environment of the atoms in materials which may often melt at very high temperatures.

X-rays and neutron sources provide radiation with wavelengths of the order of interatomic distance and are useful to probe atomic structure in the sample. Contactless experimental methods achieve freedom from contamination of sample with containers. Supercooling of the liquid is facilitated by avoiding crystallization process at melting temperature which otherwise would occur at the interface with the container. Windows in conventional furnaces can restrict the solid angle for both incident and diffracted beams. By contrast, contactless windowless furnaces allow well-controlled structural investigation of the supercooled liquid and melt of refractory materials at very high temperatures. They oppose gravity with the levitating forces, for instance columbic, electromagnetic, ultrasonic.

The ability of levitation techniques to access very high temperatures, maintain speci-

men purity without containment has created new opportunities to investigate the molten and supercooled liquid states. Recently, these techniques have been combined with intense X-ray radiation and neutron scattering methods to provide structural information at the atomic and nano-scale levels. In this chapter, levitation techniques are reviewed. Emphasis is placed on aerodynamic levitation coupled with CO_2 laser heating.

3.2 Levitator furnaces

In this section, we first review different levitators that have been applied to perform high temperature experiments. We then describe in more detail the aerodynamic levitator furnace which has been used for the structural studies of refractory oxides in this project.

3.2.1 Electrostatic levitation

The electrostatic levitation (ESL) furnace was developed by Rhim *et al* [23] for microgravity experiments and an advanced levitator furnace is described by Rulision *et al* [24]. Rhim's group has levitated and melted refractory metals such as zirconium [25], titanium [26], silicon [27] and germanium [28]. They also measured thermo-physical properties such as density [29], isobaric heat capacity [30], surface tension, viscosity [31] and electrical resistivity [32]. This method used the Coulomb force between charged sample and electrodes to levitate and a laser system to melt the sample. The sample was stabilized through an optical sensor and electrode system. Two telephoto cameras were used to record the sample images for thermo physical properties measurements. Figure 3.1 shows an ESL furnace used by Ishikawa *et al* [6]. The ESL furnace was enclosed in a stainless steel chamber that was evacuated to a pressure of around $10^{-5}\,Pa$. The chamber housed a pair of parallel disc electrodes, typically $10\,mm$ apart, between which a spherical sample was levitated. The sample was positively charged by electron emission, e.g. from laser heating [13]. The top and bottom electrodes were maintained electrically negative and

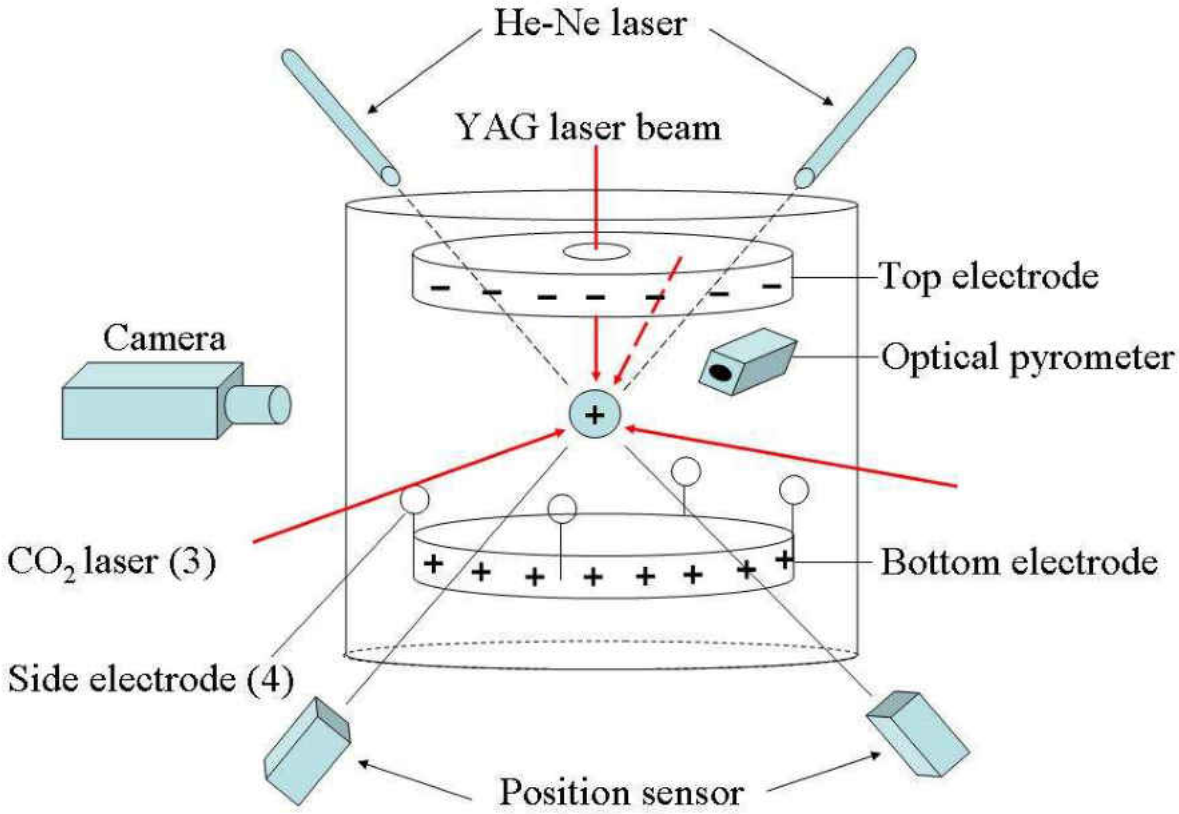

Figure 3.1: Schematic view of the electrostatic levitation furnace adapted from [6]

positive respectively. To levitate a typical sample whose size of 2mm in diameter, an electrical field of between 8 to 15 $kV\ m^{-1}$ was necessary in order to overcome gravity. The electric field between the plates generated columbic force to control the vertical position (z) of the specimen. In addition, four spherical electrodes distributed around the bottom electrode were used for horizontal control (x and y). Since the electrostatic scheme could not produce a potential minimum, a feedback position control system was necessary. This system was achieved with two orthogonally arranged He-Ne lasers (632.8 nm) that projected sample images onto two optical sensors. The sample shadow covered the optical sensor area. The sample position information read by optical sensors was then fed to a computer and analysed by a program which controlled the voltage supply of electrode

system. Thus the sample was maintained at a fixed position in time. The feedback rate was 720 Hz for the z direction and 30 Hz for the x and y directions.

Sample heating was achieved using two CO_2 lasers (100 W, 10.6 μm) and a Nd:YAG (520 W, 1.064 μm). One CO_2 laser beam was focused directly to the sample whereas the other CO_2 laser beam was divided by two portions. These three beams hit the sample separately by 120 ° in horizontal plan. The higher power Nd:YAG laser was used to melt the sample with melting temperature higher than 2000 K. This laser beam was focused vertically to the sample through the hole in the top electrode. This quasi-tetrahedral multiple beam configuration enhanced temperature homogeneity. Once the sample was levitated, the laser power was gradually increased until the sample was fully melted.

Sample temperature data were measured using a pyrometer of single colour (0.96 μm, 120 Hz), equipped with a band stop filter at 1.064 μm to remove any noise coming from the Nd:YAG laser. The apparent temperature, obtained from the pyrometer, was calibrated using Wien's law.

Charged-coupled-device video camera of high-resolution black and white equipped with a telephoto objective and a high-pass filter at 450 nm were used to obtain magnified views of the sample. After experiment, the video images were digitized and the sample radius was extracted from each image. The images were then matched with the temperature curve. In a spherical assumption, the volume of sample was obtained from the radius, and because the mass was known, the density could be found as a function of temperature. The recorded images were calibrated by levitating the sphere with a precisely known radius under identical experimental conditions.

3.2.2 Electromagnetic levitation

Like ESL, Electromagnetic Levitation (EML) can be used to levitate and melt refractory metals and alloys but without the need of laser for heating. EML method has enabled

some investigations in supercooled liquid and melt states of electrical resistivity [33], short-range order of iron [7] and the composition dependence of phase in Ni-V alloys[34]. Figure 3.2 shows a schematic view of an EML furnace which has been used for neutron

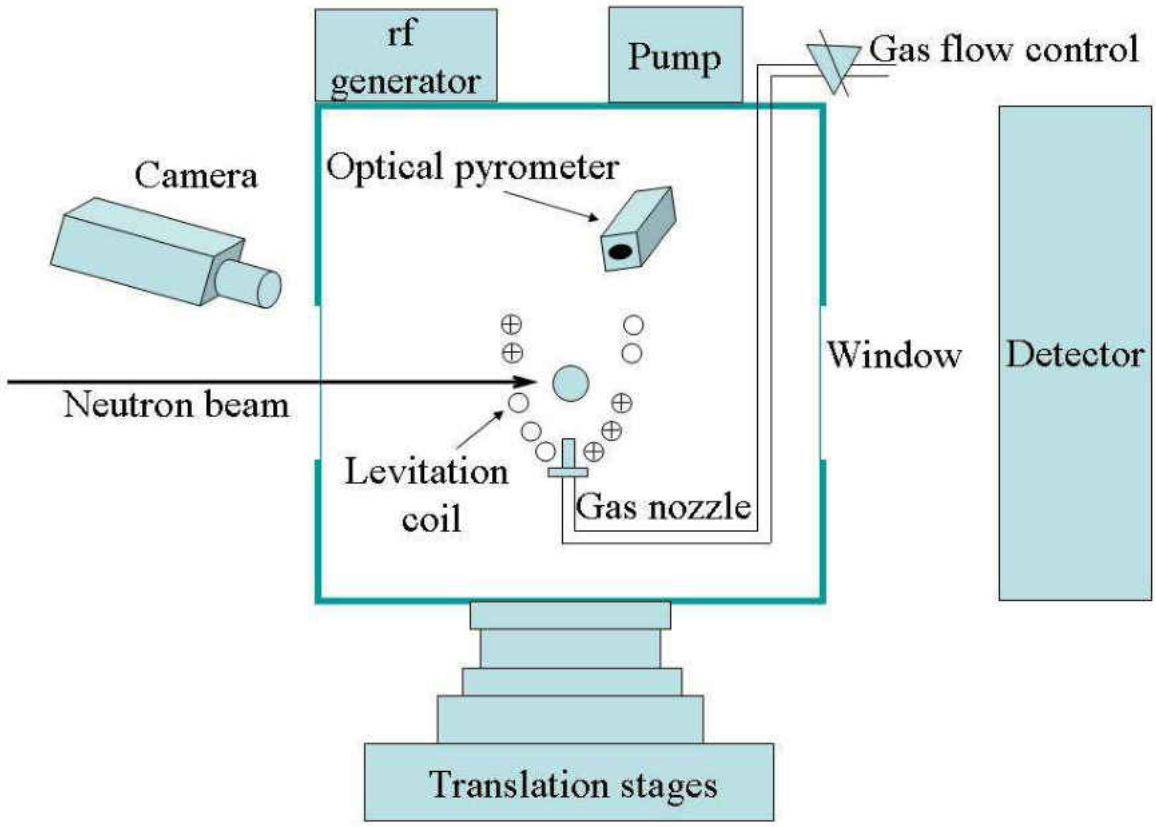

Figure 3.2: The electromagnetic levitator furnace for neutron scattering adapted from [7]

scattering [7]. The translation stages were used to place the sample in the beam. A video camera was integrated with the furnace to check the sample position. To avoid any disturbance to the diffraction measurements, the sample movement should be small (less than $1\,mm$). The levitation chamber was equipped with a window of $1.5\,mm$ thickness of aluminum for neutron or high energy synchrotron radiation scattering. The window covered an angle of $200\,^\circ$ around the vertical axis of the levitation chamber allowing the scattered neutron beam to be countered by the detector in wide angle. The temperature

of the sample was measured by an optical pyrometer.

The levitation coil system was a water-cooled copper coil especially designed for this kind of diffraction experiment. The coil contained five windings at the lower part and four counter-windings in at the top part for sample stabilization. The space between the lower windings and the counter-windings was broad enough to have an unobstructed view of the sample in the beam direction. The levitation coils were powered by an rf generator with a maximum output power of $5\,kW$. The operating frequency depended on the inductivity of the used levitation coil system and typically was at approximately $150\,kHz$. The rf field induced eddy currents in the electrically conductive sample which, together with the field, generated Lorentz forces that opposed gravity. According to Lenz's rule this force pointed in the direction of a low magnetic field strength which can be adjusted such that gravity is compensated. The sample was levitated in solid and liquid states. Electromagnetic forces can also induce deformation and mixing which are useful for homogenization in the liquid state of the sample. This technique allowed the spherical sample of 6-10 mm in diameter to be levitated.

The furnace was enclosed in an ultra-high-vacuum chamber that was evacuated to a pressure of $10^{-7}\,mbar$ by a pump placed on the top of the chamber. Afterwards it was backfilled with processing gas of 99.99999% purity [7] via gas flow control. The pressure inside the chamber during diffraction experiment was maintained at around 1 bar. Depending on the processed sample material pure He or a He(4% H_2) mixture has been used as processing gas. The processing gas flowing over the sample surface was used to reduce the sample temperature instead of reducing the rf power that can change the sample stabilization. The gas nozzle was installed at a distance of 4-8 mm below the sample.

3.2.3 Ultrasonic levitation

The capacity of the ultrasonic levitator (USL) to measure weight change [8] and density[35] and has been demonstrated. The ultrasonic levitation method can be used as a preparative method for melting phase reactions [35, 36]. Figure 3.3 shows a sketch of the experiment adapted from ref [8]. In the levitator, a piston transducer generated a cylindrical sound field, enclosed within a glass tube and a concave reflector positioned opposite to the transducer. The levitator operates at a frequency of 57 kHz. The sample was levitated in the centre of glass tube by standing wave field. The sample is situated in one of the wave nodes.

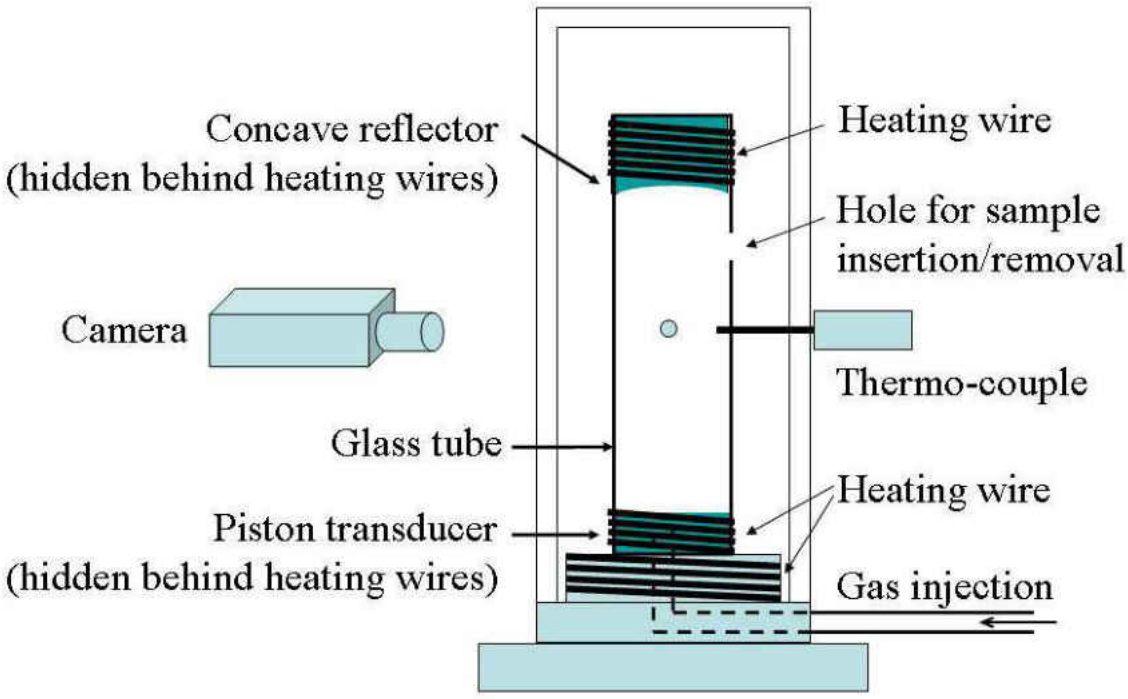

Figure 3.3: Sketch of an Ultrasonic levitator adapted from ref [8]

The whole reaction chamber is heated by high electrical resistance wires. Heat is transferred from the wires to the sample through radiation and thermal contact between the sample and the reactive gas inside the reaction chamber. The gas can be introduced

symmetrically into the cylindrical sound field through the gas inlet.

The ultrasonic levitator furnace has been usually used to levitate and melt the spherical samples of small diameter ($1\,mm$-$30\,\mu m$) [8] and low melting temperature , for example o-terphenyl (OTP) which melts at $331\,K$ [36]. A constant and uniform temperature in the reaction chamber is necessary, when working close to dew point of the reactive gas. The sample temperature was measured by a thermo-couple whose head was placed close to the glass tube to avoid disturbance to the sound field.

A camera with a long focal length lens has been used for measurement and recording the size, shape and position of the sample. The camera operates at a distance of $86\,mm$ from the levitated sample.

3.2.4 Aerodynamic levitator

Aerodynamic levitation (ADL) furnaces have been developed recently [37] and have been used in X-ray [38] and neutron [39] scattering experiments. These have been adapted for the structural investigation of refractory oxides to be described later. The furnace was designed for *in-situ* measurement in combining with small angle X-ray scattering (SAXS) and wide angle X-ray scattering (WAXS) at very high temperature.

.

The arrangement of Aberystwyth aerodynamic levitator furnace in the experimental station multi-pole wiggler (MPW) 6.2 of the synchrotron radiation source (SRS) will be described later (section 3.3). Figure 3.4 shows a close-up of the levitator furnace on which the spherical sample floats on a stream of high purity argon. The gas from the pressurized gas cylinder ($200\,bar$) is reduced in pressure to 1bar through a standard gas regulator and then flows through the levitator nozzle. The convergent/divergent conical nozzle shapes the gas jet which exerts a force on the surface of the sample that opposes gravity. The gas flow rate is controlled with a flowmeter. Flow rate can be varied up to $30\,l\,mn^{-1}$ with

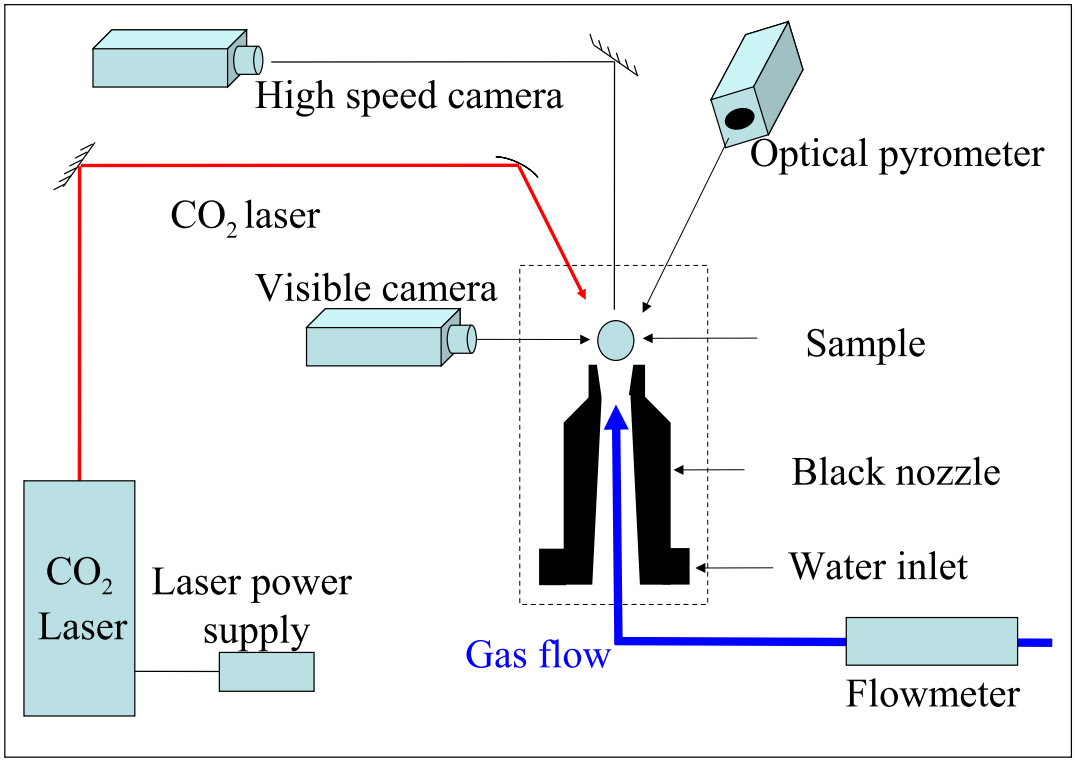

Figure 3.4: General close-up of aerodynamic levitator showing the gas flow, laser heating, pyrometer and camera.

steps of $0.003\,l\ mn^{-1}$, but typically $3\,l\ mn^{-1}$ is used. By adjusting this rate, the sample can be levitated and stabilized in the equilibrium position. The spherical sample whose size is around 1-3 mm of diameter can be freely supported. A stream of water passes through the nozzle for cooling down the nozzle which absorbs the radiation heat from the sample.

The heating system for the aerodynamic levitator furnace comprises a continuous wave CO_2 laser (125 W, 10.6 μm), which is suitable for non-metal materials such as refractory oxides that absorb strongly the infrared. Laser power is altered by the power supply (UC-2000 laser controller module). The first mirror is flat to reduce the laser flux intensity on the second mirror which has the focal length of 160 mm. Laser beam size is 4.4 mm.

The sample is placed at a distance of 80 mm. The laser beam size at sample position is 2.0 mm which covers the whole sample surface in crystalline as well as liquid state allowing more homogenneity in the temperature of the sample. The sample is very stable levitated during melting. Temperatures up to 3000 K have been achieved for a 2 mm alumina sphere. For alignment purposes, a 5 mW He-Ne laser producing a red light around 650 nm is superimposed on the CO_2 laser axe by means of an in-built zinc selenide beam combiner.

Two visible and microscope cameras have been integrated in the levitator furnace to visualize the sample position. The microscope camera has magnified zoom lens of 5X and a welding filter allowing the sample visualization to be achieved even at very high temperature. The aerodynamic levitator furnace can also be combined with a high-speed camera allowing critical processes such as recalescence or melting to be studied. The recorded video file will be digitalized in one-by-one frame that can be used for thermo-physical property measurements. The rate of image recording can reach up to 37000 $f.s^{-1}$ but typically a rate of 900 $f.s^{-1}$ is used for viscosity and surface tension measurements (section 4.3).

.

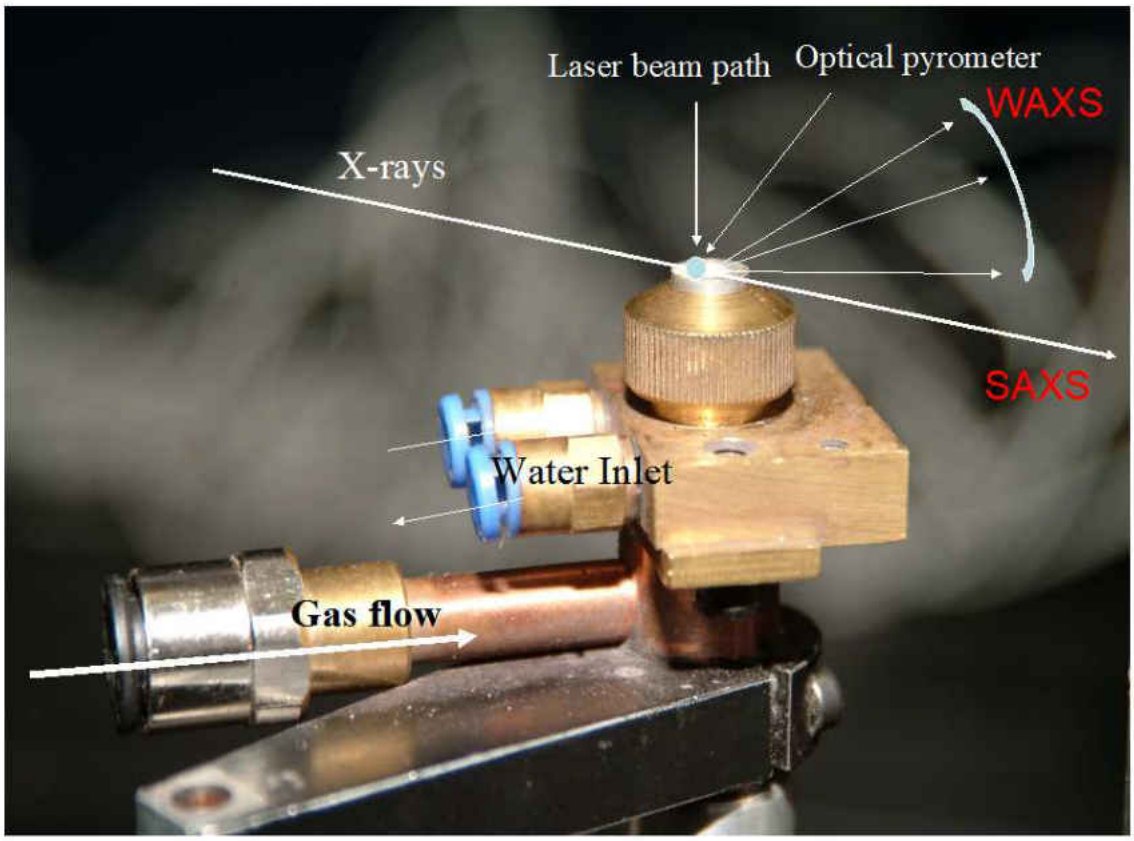

Figure 3.5: Aberystwyth aerodynamic levitator contains a convergent/divergent nozzle, a water-cooling copper base, and gas flow tube.

3.3 Experimental arrangement

X-rays generated tangentially from the synchrotron radiation source (SRS) were fed into the experimental stations through an optical system. The optical system contains reflecting mirrors, monochromator and several slits for X-ray beam collimating, focusing and wavelength selection purposes. The aerodynamic levitation furnace was placed in the experimental hutch (figure 3.6).

3.3.1 Synchrotron radiation source

Synchrotron radiation source (SRS) usually employs a dedicated *storage ring*. Electrons are accelerated and injected in the storage ring; then they are maintained at a fixed energy

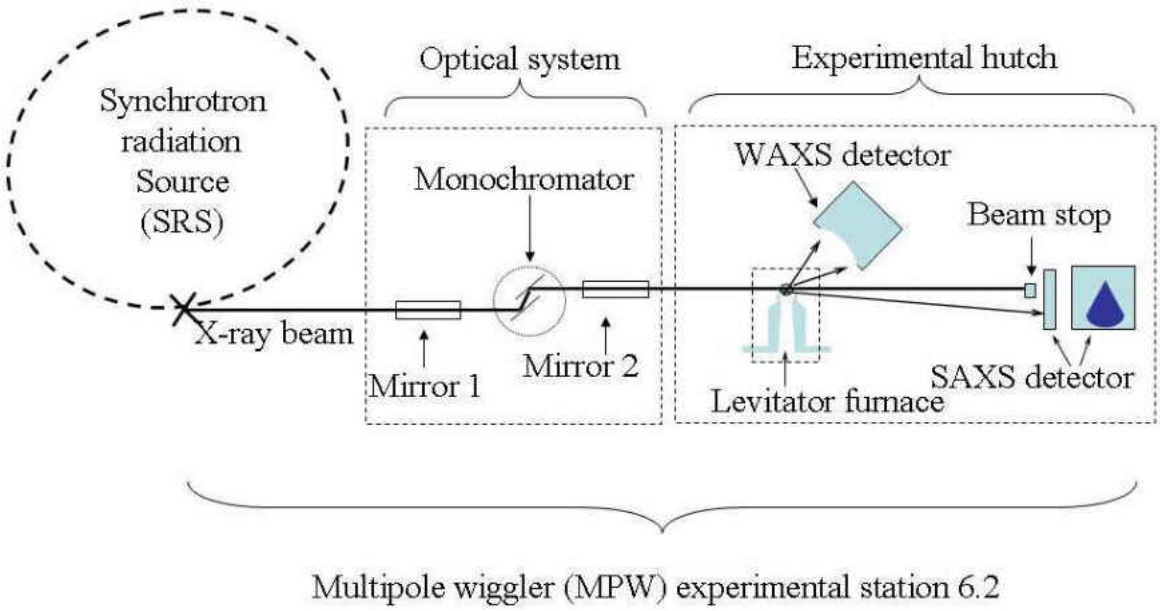

Figure 3.6: Schematic view of experimental setup with aerodynamic levitation furnace in MPW6.2 at the SRS

by application of the magnetic field. Synchrotron radiation is electromagnetic radiation emitting tangentially from the beam orbit where electrons are accelerated angularly. Electron energy and electron beam current are two main characters of a synchrotron radiation source. Electrons are slowly scattered out of the beam orbit both by electron-electron interaction (important in low energy machines) and by collision with gas molecules inside the tube even under high vacuum conditions. In consequence, the electron beam current and hence the synchrotron radiation intensity decays exponentially. Refilling the storage ring is required every 12-24 h. The energy lost from the electron beam due to emission of the synchrotron radiation is replenished by radio frequency power provided by a klystron. Figure 3.7 shows the layout of the SRS, Daresbury laboratory. The storage ring is operated at high vacuum (less than 10^{-9} $torr$). The electron beam is bent by a succession of powerful magnets separated by straight sections. An accelerating electron can emit electromagnetic radiation. In this case, when a magnetic field is applied to change the electron curvature, electrons have an angular acceleration, and thus emit radiation. At

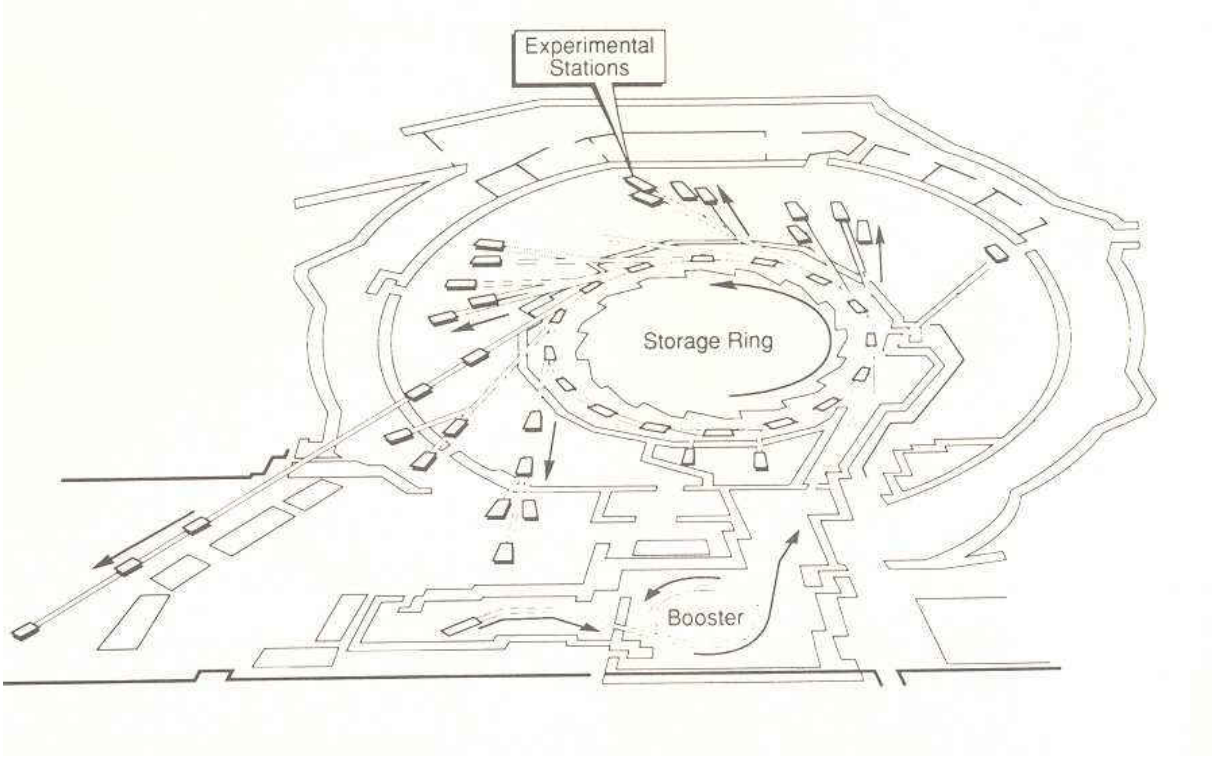

Figure 3.7: Layout of the SRS, Daresbury laboratory showing the storage ring, the beam lines and experimental stations [70].

the SRS, there are sixteen 1.2 T magnets which bend the 2 GeV electron beam through a radius of 5 m.

Additional magnetic devices (wigglers and undulators) can be inserted in the straight sections to alter the electron beam curvature (like the skier trajectory) to provide much more intense radiation. The synchrotron radiation is then fed into the experimental stations in a very small angle called the photo opening angle. The incident X-ray flux of the station 6.2 at the SRS was generated from a ten-pole wiggler which has been installed in straight section 6. The total photo flux has been calculated at the focus (Figure 3.8). The absorption of Be windows and air path are included. The peak at around 8 keV has the maximum flux of the order of 10^{12} *photons/s/0.01%* band-pass with the beam current of 200 mA. The practical photo energy range (5 keV to 18 keV) was defined by beryllium window absorption at low energy and the high energy flux limit from the 2 T magnetic

poles of the insertion device.

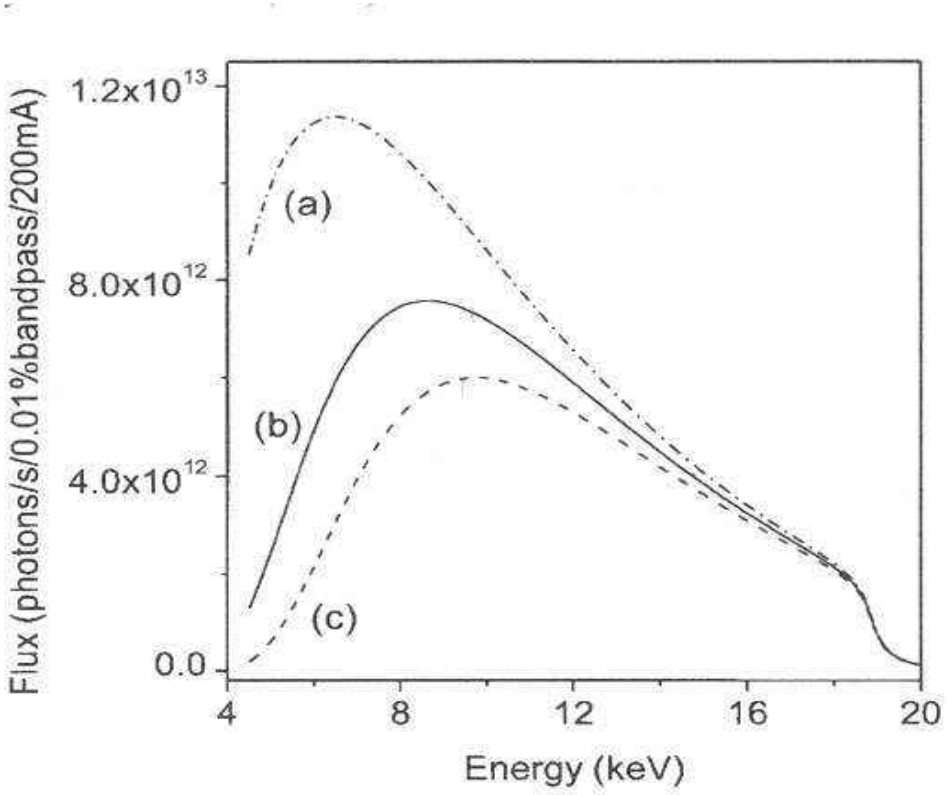

Figure 3.8: Total photon flux calculated as a function of energy in the focused beam with the inclusion of (a) 0.6 *mm* Be for the beamline windows, (b) 0.6 *mm* Be and 25 *cm* air and (c) 0.6 *mm* Be and 50 *mm* air with the SR machine running at 200 *mA* [9].

3.3.2 The optical system

Because of the large distance from the source to the experiment, which may be 20-30 *m*, focusing optics are often employed to exploit the extreme brilliance of the source. Figure 3.9 shows a general view of the optical system in MPW6.2 station at the SRS. Station MPW6.2 receives a horizontal fan of radiation from 0.5 to 4.5 *mrad* and a vertical fan of 1.4 *mrad* as defined by a water-cooled aperture at a distance 12.88 *m* from the source. This produces a beam 3.8 *mm* high and 67.5 *mm* wide at the first Si mirror in the optical system. The output X-ray beam from the source was then collimated by the first of

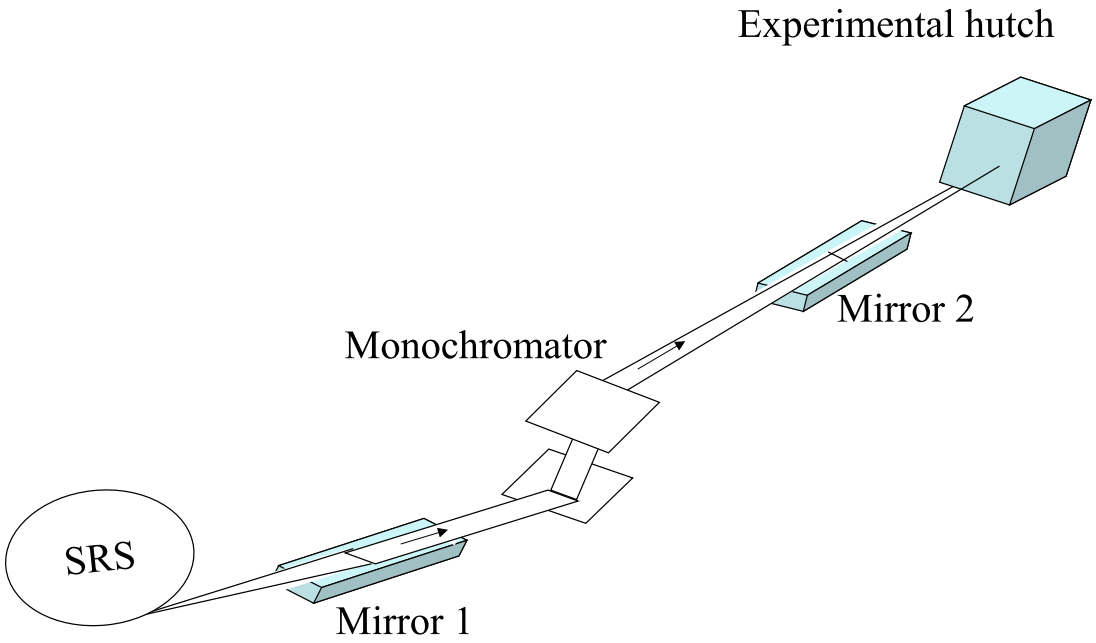

Figure 3.9: The overall layout of the optical system in the MPW6.2 station at the SRS

two identical planar, cylindrically bent, Si mirrors (1220 mm x 120 mm x 50 mm with a 500 Å rhodium coating). The beam afterwards was generally parallel. The sagittal-crystal monochromator gives both energy selection and horizontal focusing.

The monochromator has a flat, water-cooled, first crystal cut along the (111) direction allowing selection of any energy in the range 5-18 keV (2.5-0.69 Å). The second Si crystal, also cut along the same direction, is sagittally bent and collects the entire available horizontal aperture. The degree of bend on the second crystal allows the full incident fan to be focussed horizontally to ≈1.3 mm full-with at half-maximum (FWHM) at any point in the experimental hutch over a range of 5 m. A second plane Si mirror is used to provide vertical focussing of the beam to ≈ 300 μm (FWHM). A system of slit is placed following

the beam to reduce the beam size and also parasitic scatter.

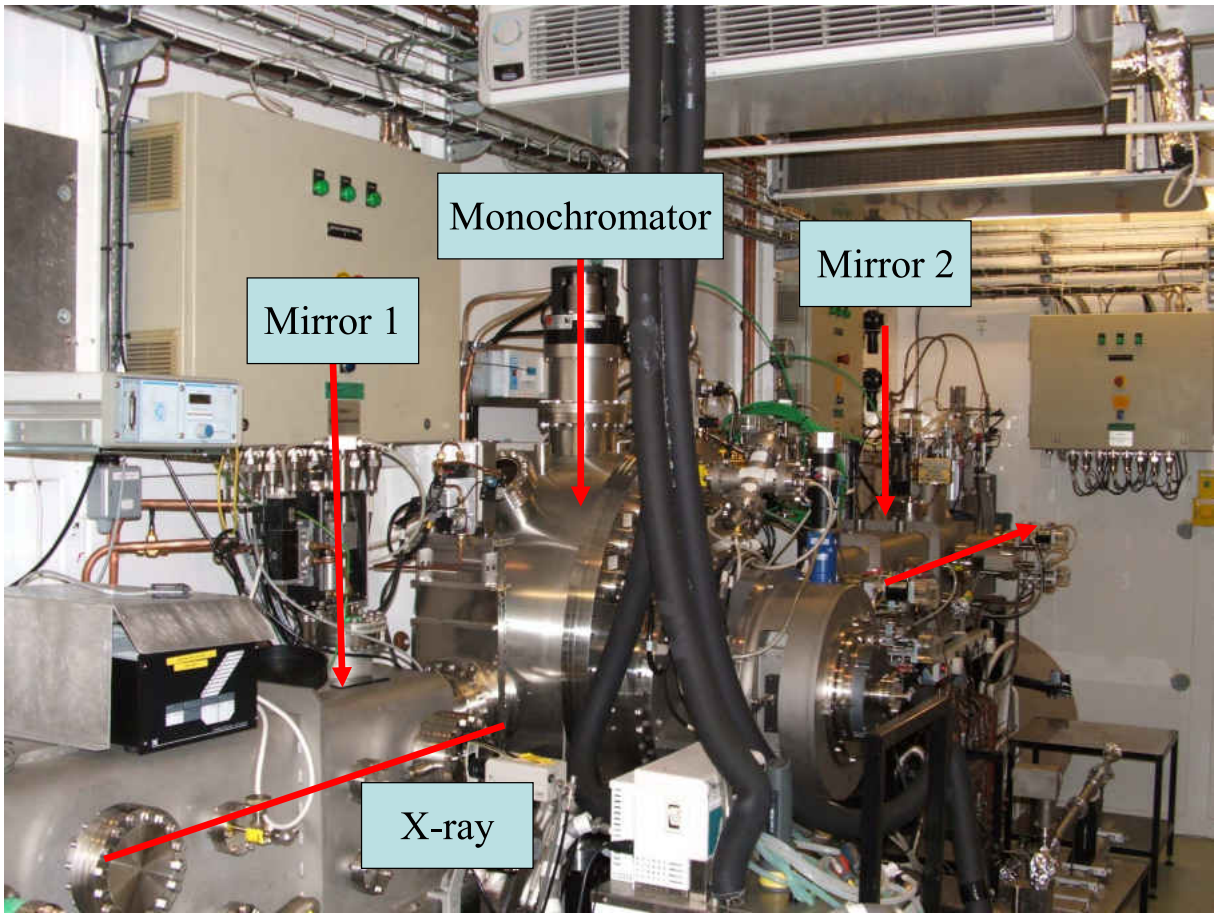

Figure 3.10: Photo of the optical system in the MPW6.2 station at the SRS

The beam, measuring 400 μm x 400 μm, is intense and stable with a high degree of monochromaticity (low bandpass, $\Delta E/E \approx 10^{-4}$). The wavelength tenability is precise with an accuracy of $\Delta\lambda \approx 10^{-4}$.

3.3.3 Experimental hutch

Figure 3.11 shows the layout of the experimental hutch at the station MPW6.2 of the SRS. For safety reasons, the furnace is enclosed in a Plexiglas box which is required to shield scatter of 10.6 μm radiation from class IV CO_2 laser. The laser power supply is interlocked with the door of the hutch so that it cannot be operated until the hutch is fully searched and interlocked.

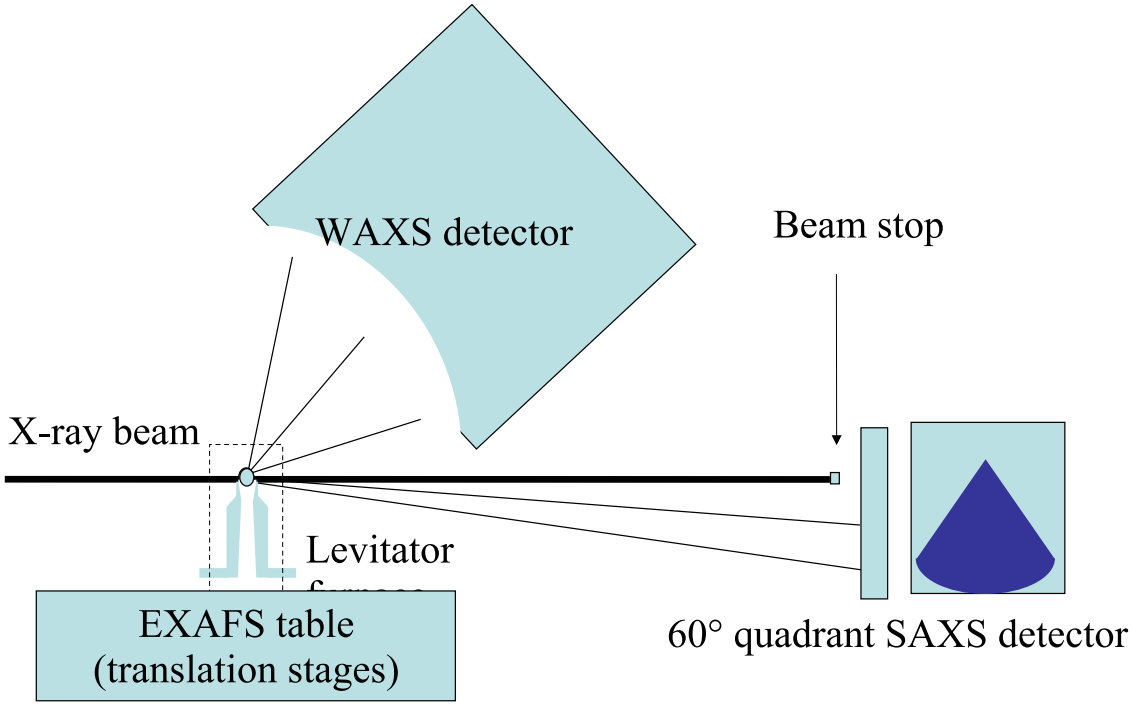

Figure 3.11: Experimental hutch at SRS MPW6.2

A whole aerodynamic levitator furnace and laser heating system were situated on the translation stages (EXAFS table) which are designed originally for extended X-ray absorption fine structure experiments. This table can be controlled by computer through Generic Data Acquisition (GDA) software. The levitated sample is placed on the axis of the X-ray beam. The sample volume gets larger with by increasing sample temperature. The height of EXAFS table should be reduced in order to keep the same amount of scattered sample in contact with X-ray beam. The vertical displacement of EXAFS table can be achieved with step of $25\,\mu m$ (sixteenth of the beam size).

WAXS detector is placed above at a distance of $366\,mm$ from the sample. A high vacuum tube is necessary to reduce the air scatter of X-ray beam before it hit the SAXS

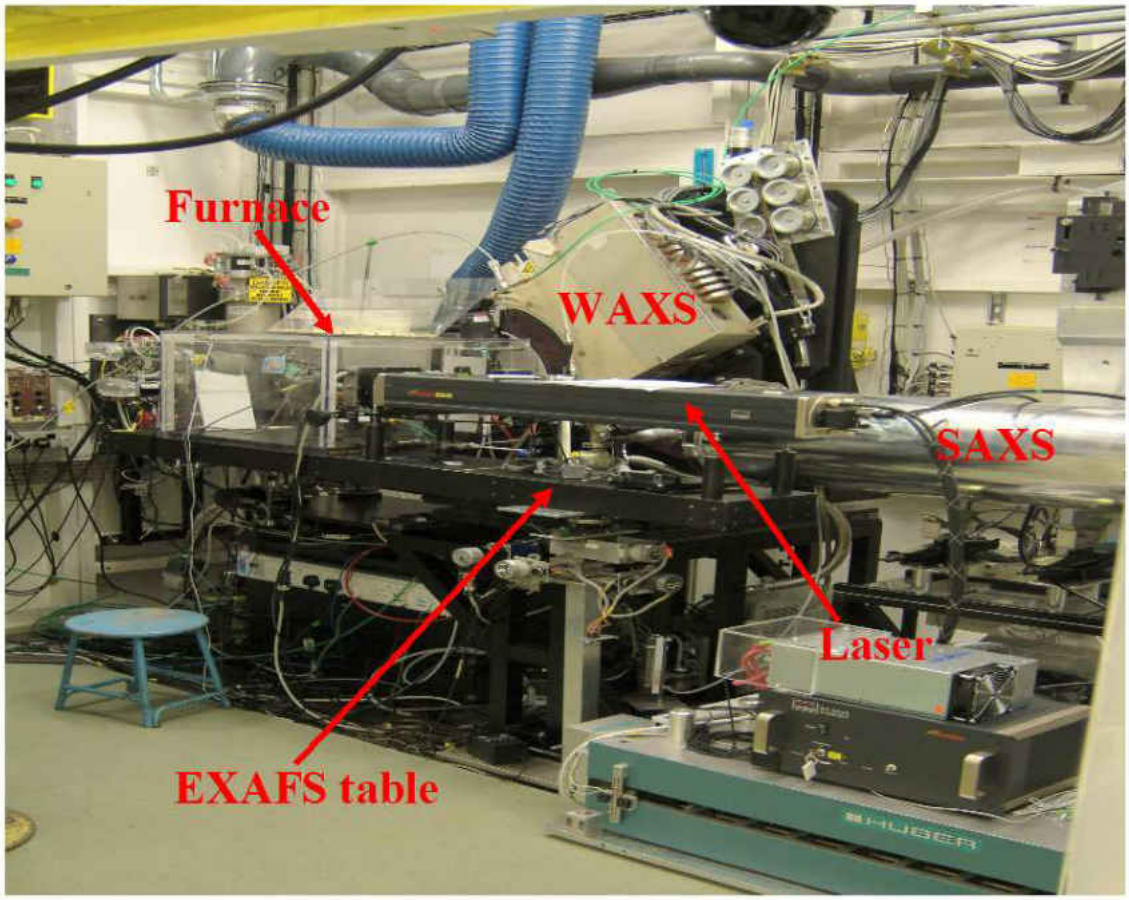

Figure 3.12: Photo of experimental hutch at SRS MPW6.2

detector which is situated between 1200 mm and 4000 mm away from the sample. A beam stop has been placed in front of the SAXS detector to block the direct beam avoiding any damage due to the very high intense flux.

3.3.4 RAPID2 detectors at MPW6.2 SRS

A second generation of the RAPID (RAPID2) readout electronics has been designed and built at Daresbury laboratory. One of the first applications was for powder diffraction and simultaneous SAXS/WAXS on dynamic systems on the MPW6.2 station at the SRS. The RAPID2 detector system for wide angle X-ray scattering is a curved and gas-filled detector.

RAPID2 detectors consist of a gas-filled tube, a positive electrode (cathode) and a

negative electrode (anode). He gas has been used to fill the tube. When X-ray encounters the gas, He atoms are ionized producing positive ions and electrons. These two charged particles are collectively called an ion pair. The positive ions were attracted to the cathode and electrons to the anode. These charges then form a very small current in the wires between cathode and anode. By using sensitive current measuring devices, the currents are measured and displayed as a signal. The position where X-ray encounters the gas can be digitalized in pixel number. Both wide and small angle detector have the same pixel size of 0.094 mm, spatial resolution of 0.375 mm (4 pixels) and operating energy range of 4-12 keV. The count rate can reach up to 106 $photonmm^{-2}s^{-1}$ which is sufficient to handle completely unattenuated diffraction patterns from MPW6.2.

The wide-angle X-ray scattering (WAXS) detector uses 128 channels of electronics to provide 4096 pixels. The target spatial resolution has a full width at half maximum (FWHM) of 4 pixels demonstrating an ability to resolve 1024 FWHM over a 384 mm long curved detector (figure 3.11). WAXS detector allows the range of angle 2θ from 7 to 67 ° to be recorded. The angular resolution equals 0.06 °.

The 60 ° quadrant SAXS detector (figure 3.11) also uses 128 channels over 200 mm radius. The angular resolution is 0.03-0.09 degree. Due to the relatively large beam size (400μm x 400μm), the beam stop limits the angle at a minimum value of 0.5 °.

Each experimental setup from different users in station MPW2.6 has a specific demand on X-ray energy E or X-ray wavelength, $\lambda(\text{Å})=\frac{12.4}{E(keV)}$. Hence the detector calibration is necessary. Detector calibration aims to convert the channel number in the detector to the scattering angle θ, (thus momentum transfer $Q = 4\pi\frac{sin\theta}{\lambda}$). Two crystalline calibrants (silver behenate, silicon) which have well charactered diffraction peaks have been used. Silver behenate which has some sharp diffraction peaks at low angles has been used for calibrating the SAXS detector. Silicon sample is used in the case of WAXS detector

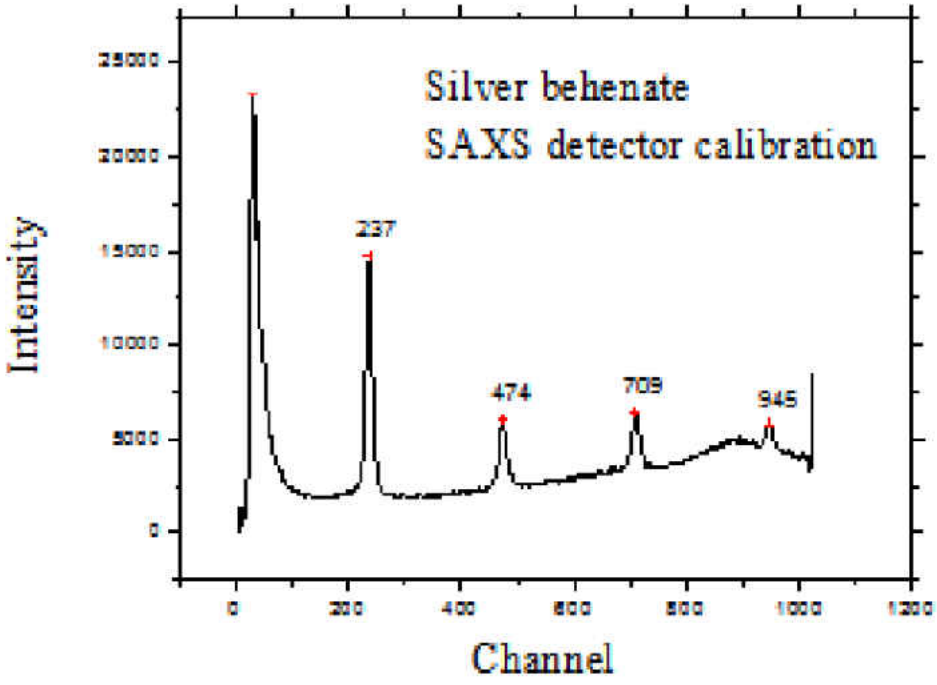

Figure 3.13: Diffraction peak at X-ray wavelength of 0.73 Å(16.9 keV) of silver behenate

calibration. The diffraction patterns of these two samples are shown in figure 3.13 and 3.14. The position of each peak in the detector is numbered by a channel number. For a given X-ray wavelength, λ, the diffraction peaks of silver behenate and silicon occur in the known angles which are calculated from their atomic interplanar distances, d ($\lambda = 2dsin\theta$). These angle values are plotted versus the channel number and shown in figure 3.15 and 3.16. The geometric centre of both detectors is obtained when this plot passes through the origin.

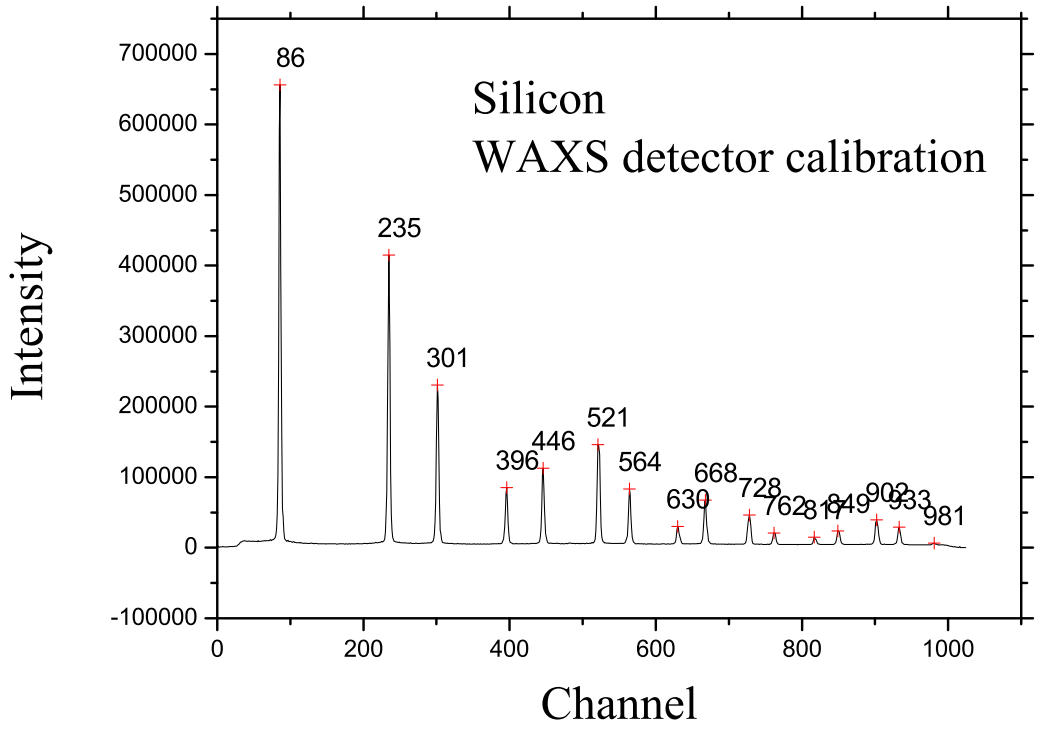

Figure 3.14: Diffraction peak at X-ray wavelength of 0.73 Å(16.9 keV) of silicon

3.4 X-ray diffraction from crystals/powders

3.4.1 Introduction

X-ray diffraction techniques are based on the elastic scattering of X-rays from the structure that have long range order. The diffraction pattern occurs when the wavelength of X-rays is similar to the repeated distance of the periodic array. Powder diffraction techniques can be used to characterize such as the crystallographic structure (phase identification, lattice parameter), preferred orientation in polycrystalline or powered solid samples. The structural information of the sample can be provided more accurately when the powder diffraction technique coupled with the lattice refinement one such as Rietvield refinement. Using synchrotron radiation can greatly increase the resolution in data; the time of data

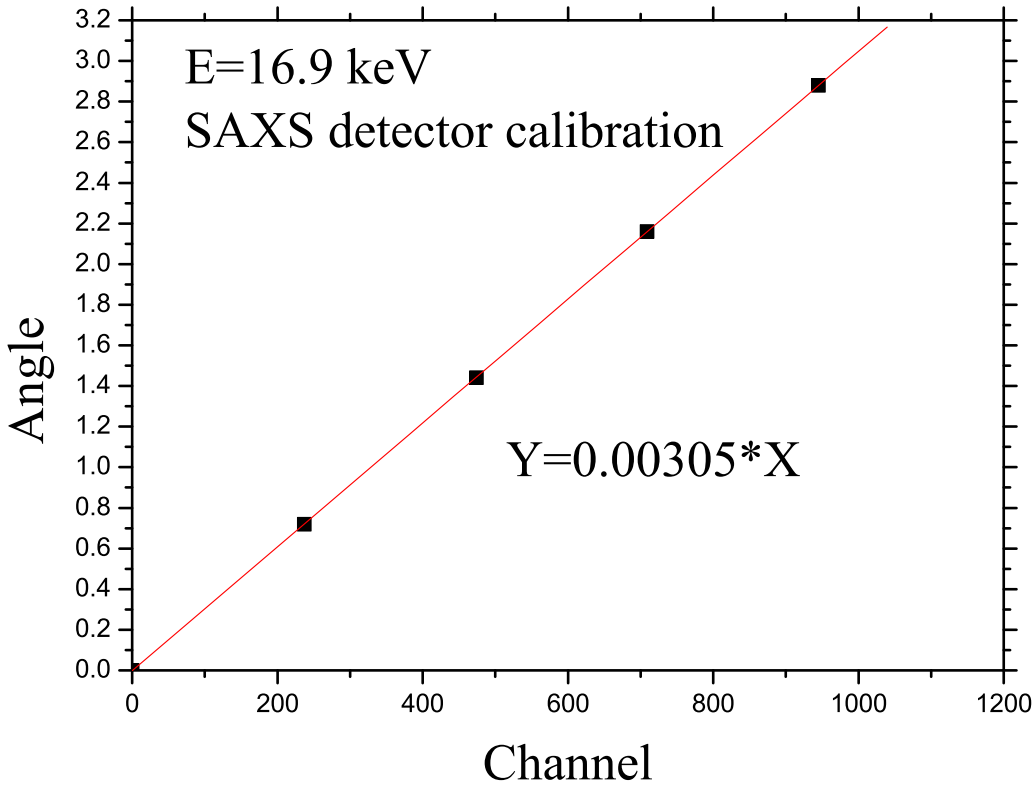

Figure 3.15: The plot of diffraction angle versus detector pixel for SAXS

collection is also reduced. This allows the complex structure and dynamics to be studied in critical conditions (high temperature, high pressure).

3.4.2 Theory

When the X-rays interact with electrons in a periodic array of atoms, the electrons are manifested as secondary point sources providing coherent radiation waves. These waves then interfere constructively and destructively in all directions. The destructive pattern occurs in most directions. But in some specific angles, the constructive interference gives rise to the diffraction intensity which results in a diffraction peak. The intensity of the diffraction peak depends on the amplitude and phase of scattering waves in a given

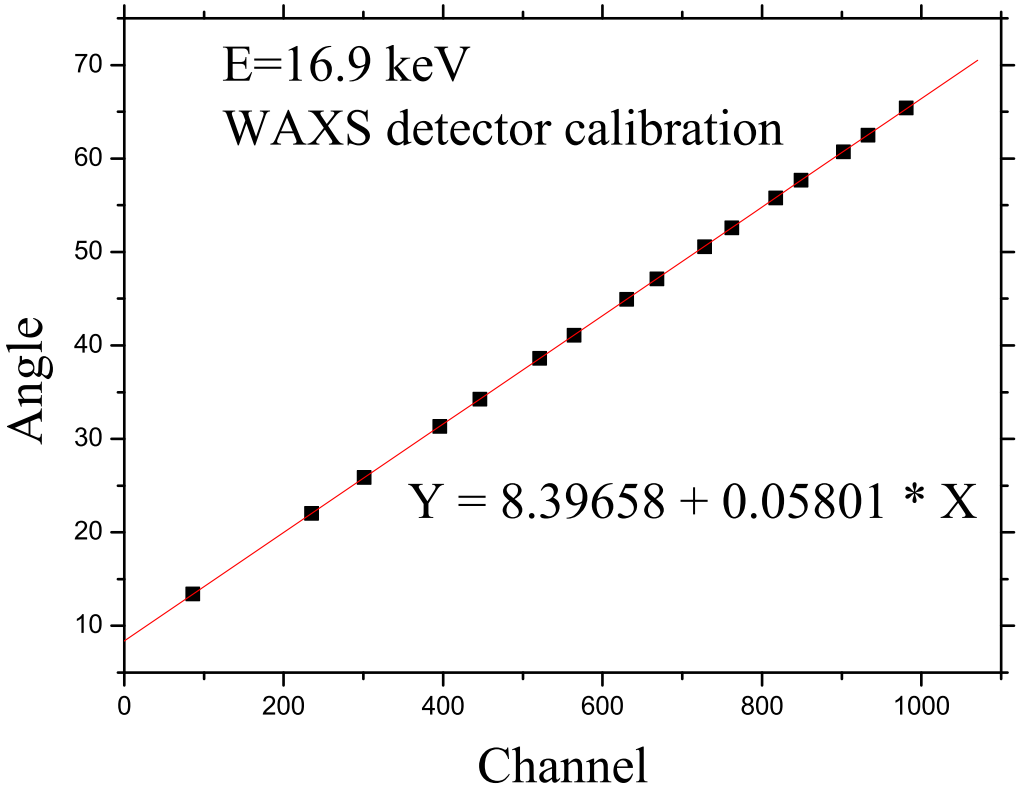

Figure 3.16: The plot of diffraction angle versus detector pixel for WAXS

direction. For coherent scattering waves, their amplitude is the same but their phase depends on the position of the electrons in the crystal structure.

Bragg law

We consider diffraction pattern from a set of lattice planes of interplanar distance d. The monochromatic X-ray radiation as incident beam is focused on the adjacent lattice planes under angle θ (figure 3.17).

The path difference of two scattering rays that strike two successive lattice planes at points O and B:

$$ABC = AB + BC$$

$$ABC = OBsin\theta + OBsin\theta$$

$$ABC = 2dsin\theta$$

For reinforcement of the diffracted beam, this path difference must be a whole number of wavelength: $n\lambda = 2dsin\theta$, where n is the order of reflection. This is known as the Bragg's equation or Bragg's law. In addition, we must show that there is no phase difference between two points (P and O, figure 3.17) in the same crystal plane. The distance travelled of the reflected ray at point P between two perpendicular wave fronts PQ and RO is QO. This is equal to $POcos\theta$. Equivalently, the distance travelled of the reflected ray at point O between these two wave fronts is PR, and PR is also equal $POcos\theta$. These two rays are therefore in phase with each other throughout. This also means that if the phase difference between B and O is $n\lambda$, after reflection, then the phase difference between B and P is also $n\lambda$. Thus, the phase difference between two rays reflected from two parallel crystal planes depends on the distance of the point of reflection measured perpendicular to the planes and not on the separation of this point parallel to the planes. This principle can be used both in considering how the amplitude of scattering from one atom depends on the diffraction angle and also in calculating how the phase of the scattered beam from each atom depends on its position in the unit cell.

3.4.3 Example for crystalline alumina

The diffraction pattern of alumina which have been recorded by SAXS and WAXS detectors in the station MPW6.2 of the SRS using the aerodynamic levitator furnace are shown as following. Figure 3.18 shows the diffraction peaks from crystalline alumina at 1273 K with the X-ray wavelength of 0.73 Å(16.9 keV).

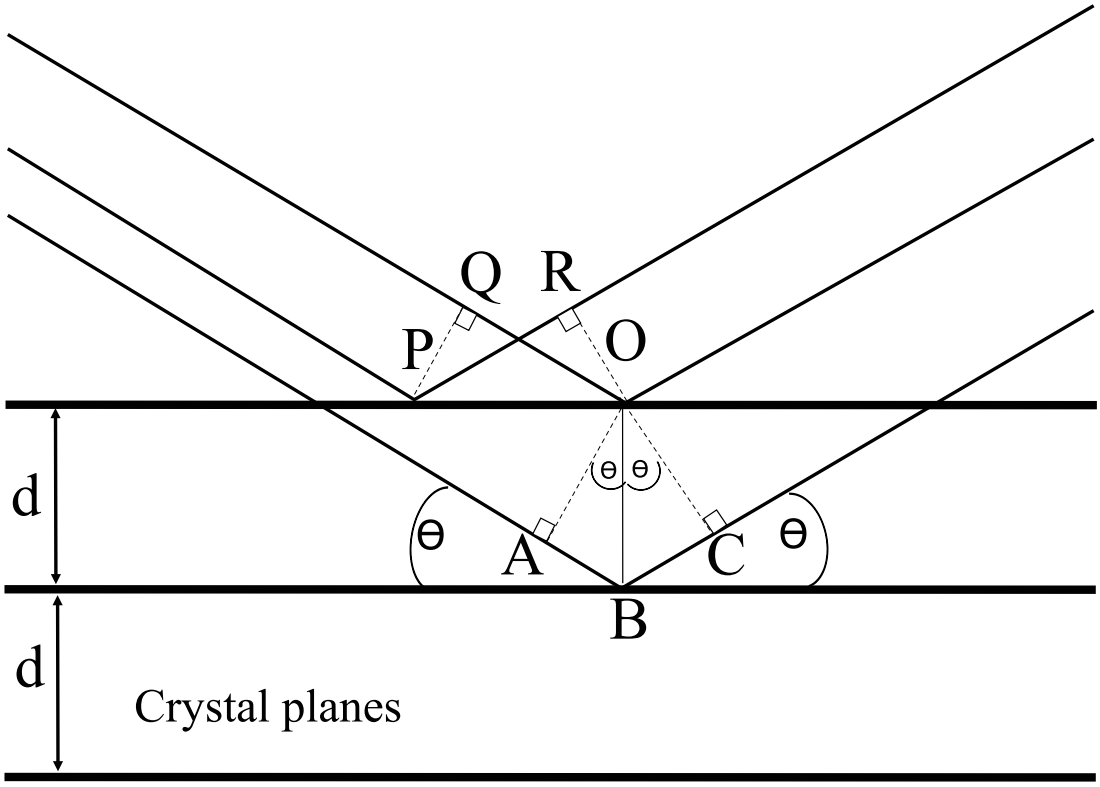

Figure 3.17: Bragg reflections by equally-spaced, parallel crystal planes

3.5 Wide angle X-ray scattering from liquids and glasses

3.5.1 Introduction

The theoretical and experimental tools employed in X-ray (neutron) studies in liquids and glasses differ, in general, from those used for diffraction of single or powder crystal, as mentioned above. The physical properties of liquids and glasses are largely due to these systems being disordered, isotropic and generally homogeneous. Due to the missing of long range order, the diffracted intensity from liquids and glasses gives rise to weaker and more diffuse as compared with Bragg peak intensities. A relation between the scattering measurement to the structural information of liquids and glasses is briefly reviewed.

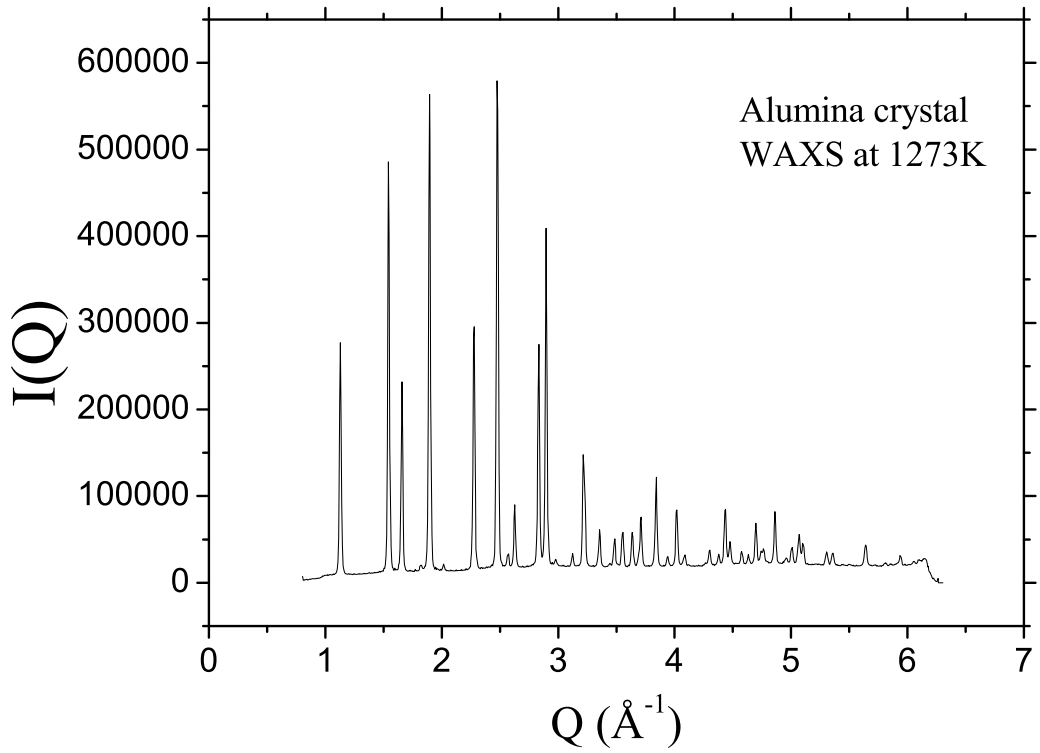

Figure 3.18: Intensity of crystalline alumina from wide angle X-ray scattering at 1273 Kwith the X-ray wavelength of $0.73\,\text{Å}(16.9\,keV)$

3.5.2 Theory

The lack of crystalline lattice necessitates a description in terms of radial distribution function *G(r)*. This function shows the fluctuation in density around a given atom chosen as origin (Figure 3.19). Close to the central atom, there is a region where the *G(r)* is zero, which denotes the hardcore repulsion of two neighbouring atoms. The first pronounced peak is at the position of atomic diameter from the origin. A series of smaller peaks at higher-r represents next neighbour shell until the saturation at *G(r)* =1, where the mean density of the system is reached. Peak position gives the interatomic distances; while the peak area can provide the coordination number of the corresponding shell.

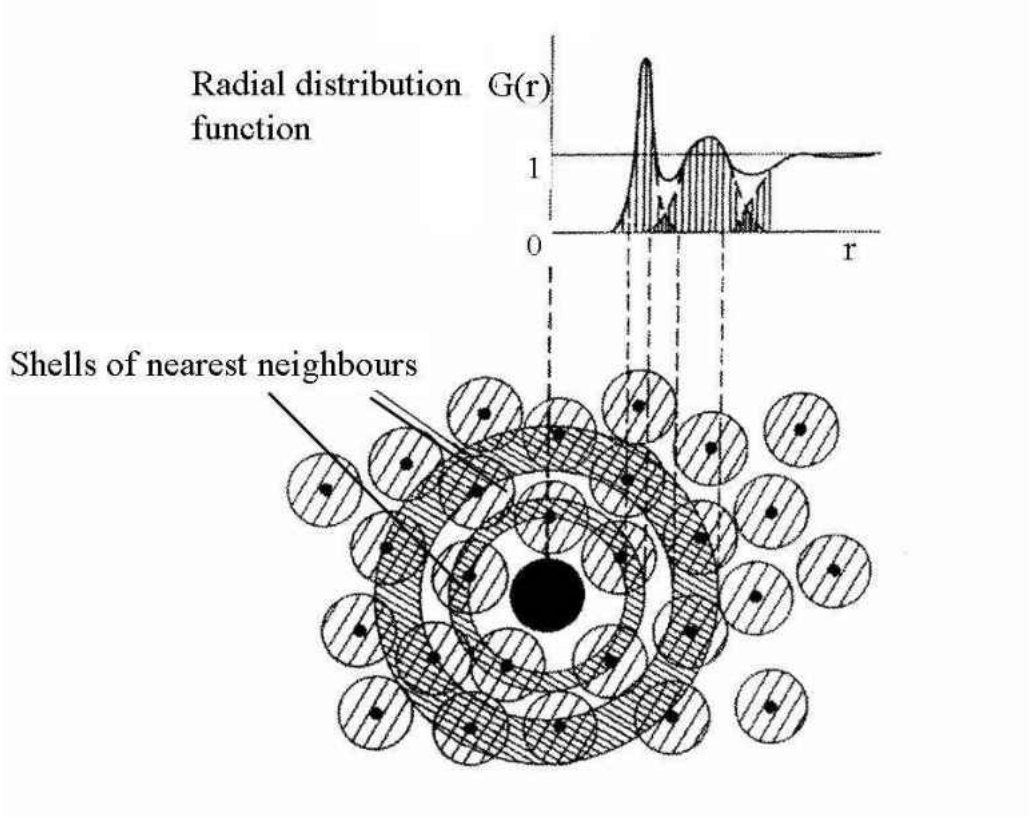

Figure 3.19: Illustration of the radial distribution function for monatomic liquids/glasses

A scattering measurement gives the total intensity, *I(Q)*, as a function of momentum transfer Q:

$$\frac{I(Q)}{I_0(Q)} = A_{coh}(Q)I_{coh}(Q) + A_{incoh}(Q)I_{incoh}(Q) \tag{3.1}$$

where $I_0(Q)$ is the intensity of the incident beam measured by an ionization chamber, and A_{coh}, A_{incoh} are attenuation coefficients for the respectively coherent and incoherent intensity I_{coh}, I_{incoh}.

The structure factor *S(Q)* is related with the coherent X-ray scattering intensity through the formula:

$$S(Q) = \frac{I_{coh} - \left\langle |f(Q)|^2 \right\rangle}{|\langle f(Q) \rangle|^2} \tag{3.2}$$

where $\left\langle |f(Q)|^2 \right\rangle$ and $|\langle f(Q) \rangle|^2$ are respectively the square of the mean and the mean-square of the scattering amplitude.

From the *S(Q)*, the radial distribution function is given by:

$$G(r) - 1 = \frac{1}{2\pi^2 \rho_a} \int_0^{Q_{max}} Q(S(Q) - 1) \frac{sin(Qr)}{r} dQ \tag{3.3}$$

where ρ_a is the number of atom per unit volume.

3.5.3 Example for liquid alumina

The measured scattering intensity at wide angle for liquid alumia at 2323 K is shown in figure 3.20. The structure factor *S(Q)* of alumina liquid at 2323 K is shown in figure 3.21. This is obtained from the measured intensity *I(Q)* and the tabulated X-ray scattering factors *f(Q)* [71] using equation 3.2. Figure 3.22 shows a result of the radial distribution function *G(r)* of alumina liquid at 2323 K. The first peak position in *G(r)* shows the Al-O distance which is around 1.8 Å, and the peak area represents the coordination number of Al-O (around 4.2) in the nearest neighbour shell. The second peak position in *G(r)* is around 3.2 Åand contains contributions from Al-Al, and O-O correlations. A third peak position in *G(r)* around 4.2 Åis due to the correclations between Al and seconde O positions.

Firgure 3.23 shows the results for partial pair correlation functions obtained by Landron *et al* [67] from neutron scattering and empirical potential structure refinement [69]. The good agreement between neutron scattering analysis and the X-ray results described in this thesis confirm the reliability of the data collection of *I(Q)* and the data reduction of *S(Q)* (figure 3.21) and *G(r)* (figure 3.22).

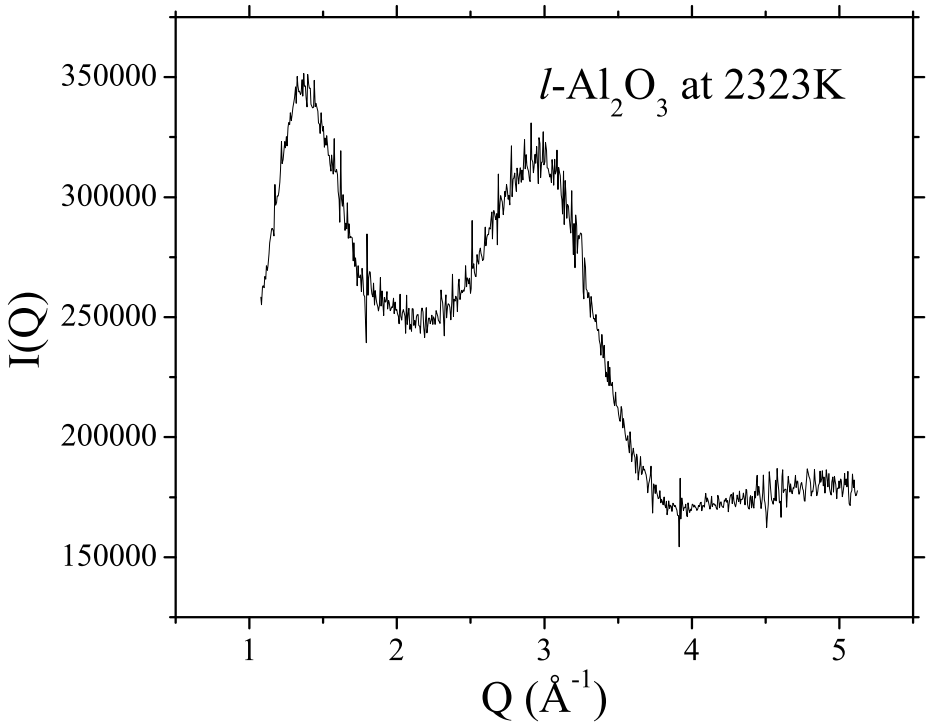

Figure 3.20: The measured scatteing intensity *S(Q)* of liquid alumina at 2323 K

3.6 Small angle X-ray scattering from liquids and glasses

3.6.1 Introduction

Small angle scattering (SAS) is the collective name representing the techniques of small angle x-ray (SAXS), neutron (SANS) and light (SALS or jus LS) scattering. In each of these techniques the radiation is *elastically* scattered by the sample. The resulting scattering pattern is analysed, providing the information about the particle size, shape, interparticle distances and particle size distribution. This section will be focused on SAXS with a brief account of theory as well as the experiment setup in SRS6.2. Since X-rays interact with the electron, so the SAXS signal is always observed and only observed

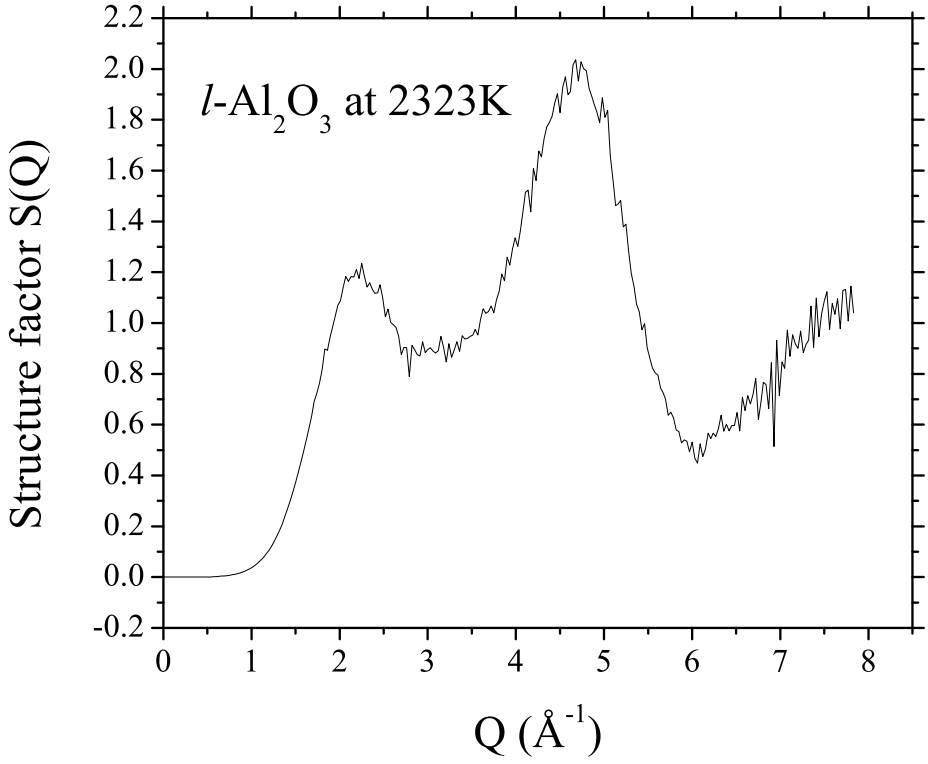

Figure 3.21: The structure factor *S(Q)* of liquid alumina at 2323 K

when the electron density inhomogeneities exist in the sample (in SANS, those are the inhomogeneities of neutron scattering length). These inhomogeneities (particles) have dimensions from several tens to several hundred times of the X-ray wavelength. The physical principles of this process can be visualized as in the figure 3.24. X-rays are scattered at the interface between two regions of difference in density. In the figure 3.24, the particles have aa density ρ_1 which is different from the medium surounding ρ_2. Incoming X-rays are scattered in the same manner of refraction in light scattering. The small particle has a larger curvature so that scattered radiation refracts at larger angles than in the scattering of the large particle. The definition of a *particle* does not necessarily reflect a real domain, but reflects the size of a scattering element that could

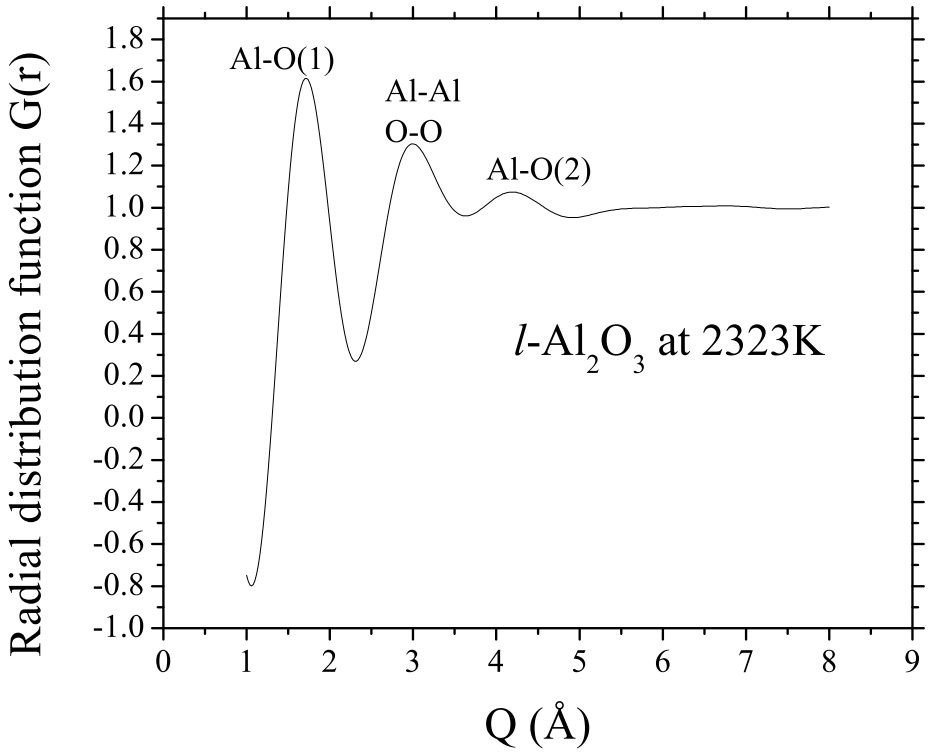

Figure 3.22: Radial distribution function *G(r)* of alumina liquid at 2323 K obtained by Fourier transforming *S(Q)* (figure 3.21) using equation 3.3.

be a component of a physical domain.

3.6.2 Theory

The measured intensity of SAXS *I(Q)* relates to the distance distribution function *p(r)* (from geometrical consideration) by Fourier inversion:

$$I(Q) = 4\pi \int_0^\infty p(r) \frac{sinQr}{Qr} dr \tag{3.4}$$

We have implicitly assumed that the particles are surrounded by a vacuum, in which case the scattering amplitude is proportional to the electron density ρ (the number of moles of electron per unit volumes). For solvent particles, only the electron density difference between solute density ρ_1 and solvent density ρ_2 is effective. The scattering

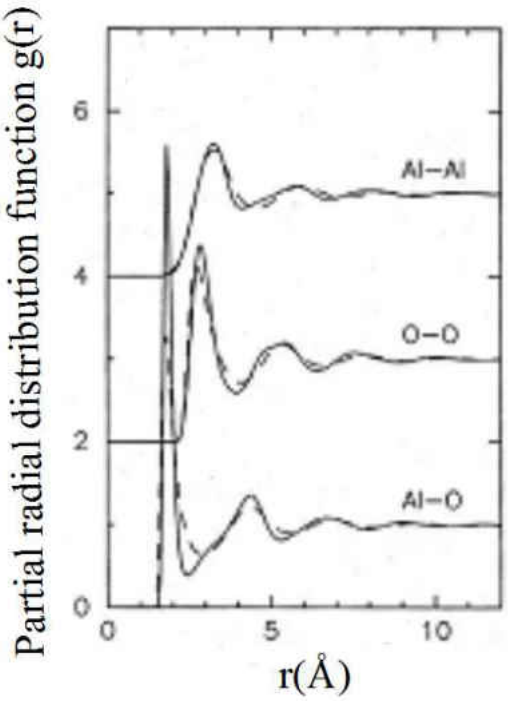

Figure 3.23: Partial radial distribution fuction as derived by Landron *et al* from analysing neutron scattering from liquid alumina using empirical potential structure refinement [69]. The peaks for Al-O (1), O-O and Al-Al and Al-O (2) align with the first three peaks in the experimental *G(r)* shown in figure 3.22.

amplitude is thus proportional to $(\rho_1 - \rho_2)^2$. It is expected to be applicable even in the case of a mixture of two liquids having different densities (like liquid-liquid transition). We will consider some assumptions and approximations in order to set the relationship between particle size and scattering angle.

Guinier region: In the low Q region (Guinier region)[40], the scattering intensity can be approximately written as:

$$I(Q) = C \exp \frac{-Q^2 R_g^2}{3} \tag{3.5}$$

where C is the scaling factor, R_g is the radius of gyration (Guinier radius). The R_g is the intuitive measure of spatial extension of the particle. The magnitude of the slope of the curve of $\ln I(Q)$ versus Q^2 is always equal to one-third of the square of R_g. The concept

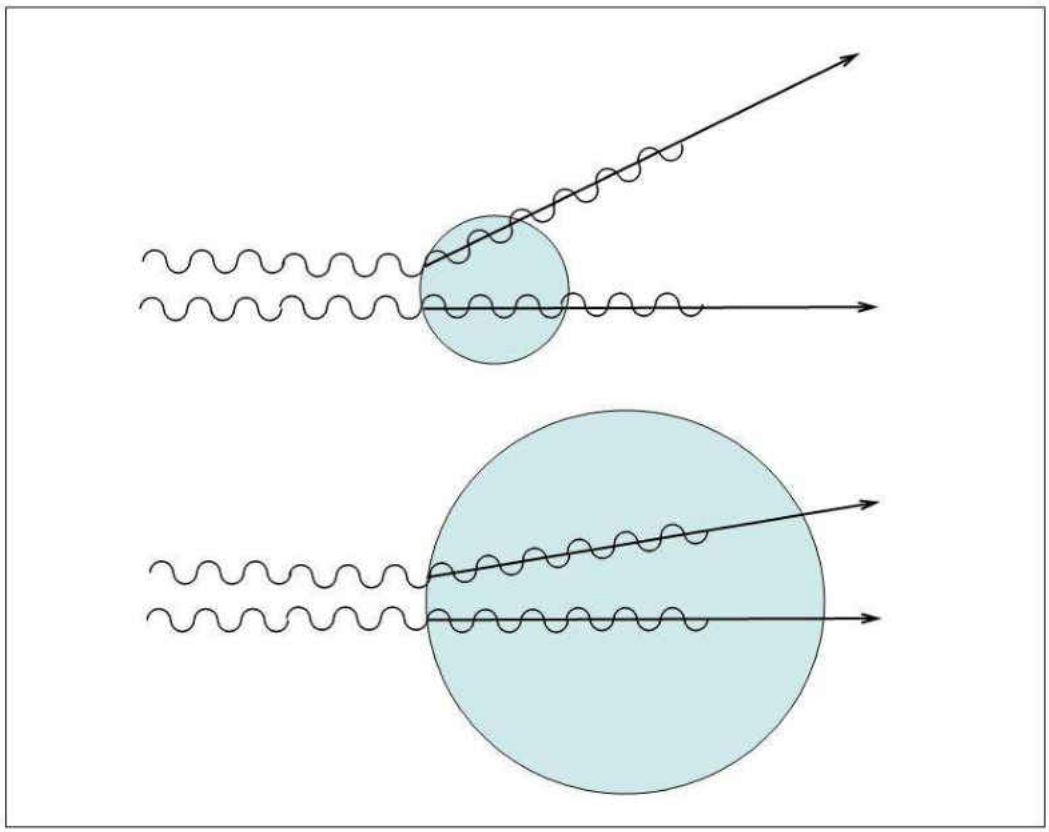

Figure 3.24: The coherent scattering from two points within a small and large homogeneous particle of density ρ. The small partical scatters through large angles and the large particle through small angle.

of R_g is sound, whatever the particle form. Although, the relation between R_g and the particle radius R depends on the particle form (sphere, rod, disc, etc).

For spherical of radius R_s, the gyration radius R_g is given by:

$$R_g^2 = \frac{3}{5} R_s^2 \tag{3.6}$$

In the case of the cylindrical (disc) particle of radius R_c and length (thickness) L_c, the formula of R_g will be:

$$R_g^2 = \frac{R_c^2}{2} + \frac{L_c^2}{12} \tag{3.7}$$

The Guinier approximation is valid within some limitations: the sample should contain particles which separate with a distance large enough for no interparticle scattering to be

seen.

Porod region: Porod's law can be used to measure the surface area of domains at the nano-scale. The scattering at larger angle (i.e. $QR_g > 1$ but still in the small angle regime) is normally generated by the surfaces of the scattering particles. The larger the particle the lower Q-value at which the Porod region starts. The rigorously derived form of Porod's law is:

$$I(Q) = I_e 2\pi\rho^2 S/Q^4 + b \tag{3.8}$$

where p is the electron density difference, I_e is a constant, S is the surface area of the particle and b is the thermal background. The surface area of particle can be extracted from the slope of *I(Q)* versus Q^{-4}. Positive deviation can be due to the thermal motion of aggregates or due to the inhomogeneities in one of the phases. Negative deviations ($Q^{-x}, x > 4$) are related to the non-smooth boundary of the scattering particle to the matrix.

3.6.3 Example for liquid alumina

Intensity of X-ray scattering measured at small angle for liquid alumina is plotted in figure 3.25. At each temperature, the sample is measured over 120 s. The background is measured at room temperature over 180 s. Two ionization chambers are positioned before and after the sample to measure the intensity of the incoming I_0 and outcoming I_t beams. We have monitored the beam position on the sample in order to keep the attenuation coefficient (I_t/I_0) of approximately 30%. The scattered intensity from the sample is the subtraction of the background from the raw data using the formula: $I_{Sample} = I_{Rawdata} - I_{Background} * (2/3) * (I_t/I_0)$

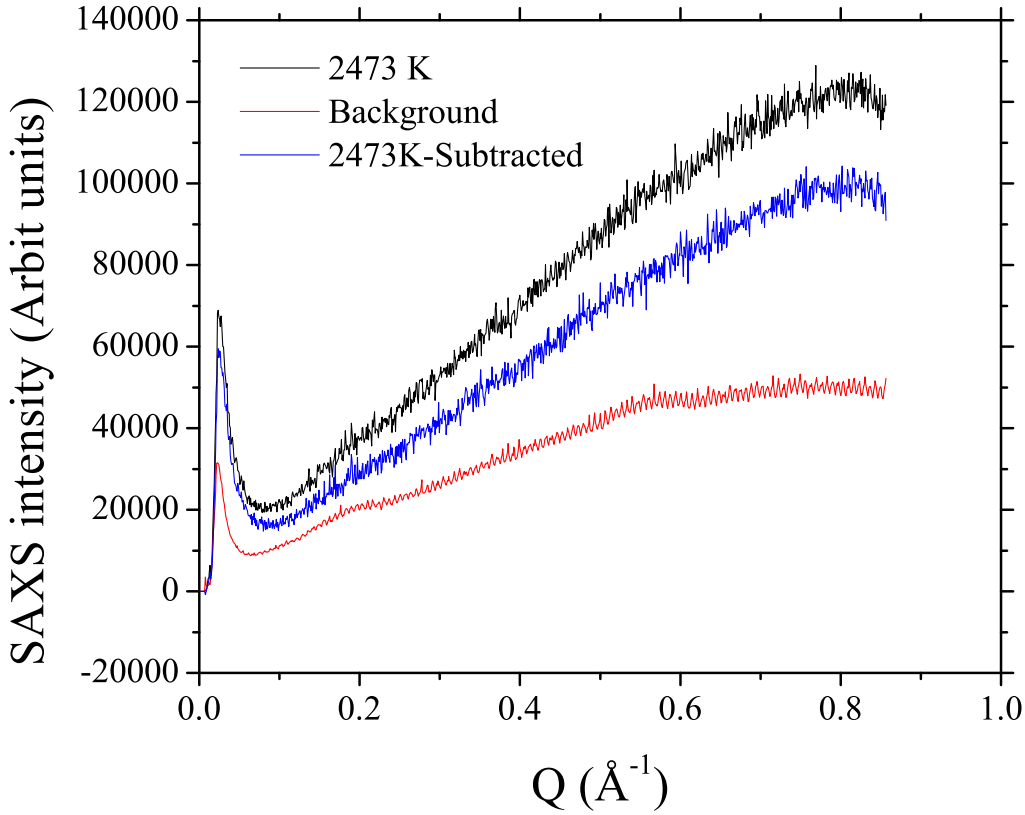

Figure 3.25: Raw data of liquid alumina at 2473 K. The data is taken by removing the background using formula: $I_{Sample} = I_{Rawdata} - I_{Background} * (2/3) * (I_t/I_0)$ where $(2/3)$ is factor of experimental duration and (I_t/I_0) is the attenuation coefficient.

Chapter 4

Rheology of Liquids at Ultrahigh Temperatures

4.1 Introduction

Rheology is known as the study of *flow* and *deformation* of liquids and solids under the action of mechanical forces. Glass has complex rheology behaviour as it is like an *elastic solid* at low temperature while at sufficiently high temperature characterized by glass transition, T_g, it flows like viscous liquid. The melting process has, however, no true melting point but instead there is progressive softening as the temperature rises. Likewise, as the temperature is lowered, liquids become more viscous and stop flowing. Viscosity is a measure of the viscous degree of liquids. By convention, liquid becomes glass on cooling when its viscosity reaches 10^{12} *Pas*. Studying thermodynamic properties of liquids such as density, surface tension and viscosity is important in controlling and predicting the behaviour of the resulting glass. Measurements of those properties in alumina has been achieved in our laboratory using high-speed camera imaging. The results show both an agreement with literature values and the ability of using the imaging method integrated with an aerodynamic levitating furnace.

There are two basic kinds of flow with relative movement of adjacent particles. In *shear* flow, the liquid elements move *over* or *pass* each other while in *extensional* flow, adjacent particles move *toward* or *away from* each other. Viscosity (from Latin *viscum*,

the mistletoe) is a measure of the resistance to flow of a liquid being deformed under shear stress or extensional stress. Newtonian liquid is the one for which viscosity changes with temperature and pressure but not with deformation rate or time. This chapter focuses on viscosity under shear stress.

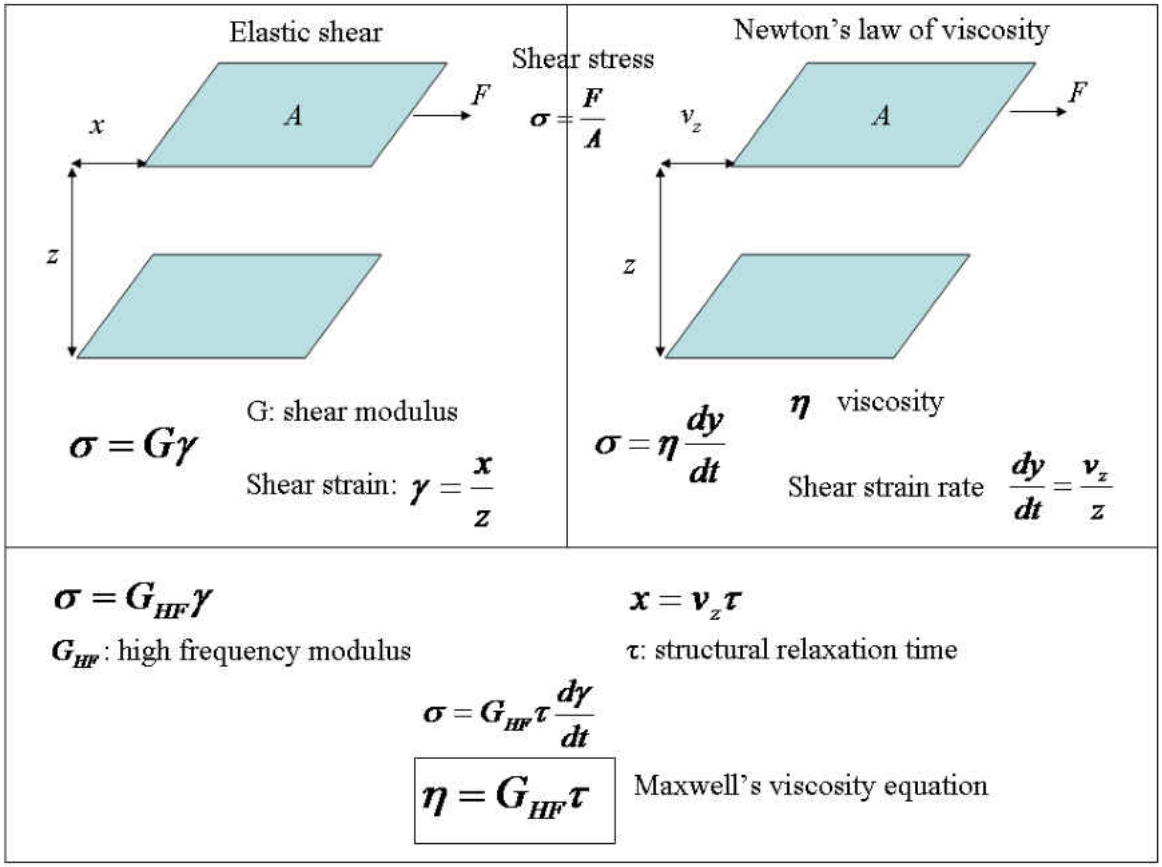

Figure 4.1: Shear stress in solids and liquids, adapted from [10]

When shear force F applies on a surface A of liquid or solid, the formula of the shear stress: $\sigma = \frac{F}{A}$. The unit of shear stress is $N.m^{-2}$. There is a difference in response to shear between solids and liquids. Under the application of shear force, the solid will distort elastically until the deformation generates a force that opposes shear force. The system is in equilibrium. However, when shear force is applied to liquid, it flows like the wind tossing the sea waves. In general, when the shear is removed, the liquid ceases to flow. In

reality, the flow decays due to the internal dissipation of energy. Layers move at different velocities. Newton's law states that for straight, parallel and uniform flow, shear stress between layers is proportional to the velocity gradient in the direction perpendicular to the layers. The elastic shear for solid and Newton's law of viscosity for liquid are linear.

Figure 4.1 shows the comparison of shear stress in solid and liquid. In solid, shear stress is proportional to shear strain :

$$\sigma = G\gamma \tag{4.1}$$

where shear modulus G is a constant. Shear strain, in linear representation, is just the ratio of displacement in x-direction parallel with shear force F to the perpendicular z-direction: $\gamma = \frac{x}{z}$. In liquid, on the other hand, the same shear stress will be proportional to the shear strain rate, $\frac{d\gamma}{dt} = \frac{v_z}{z}$ and viscosity, η:

$$\sigma = \eta \frac{d\gamma}{dt} \tag{4.2}$$

Maxwell introduced the high frequency shear modulus G_{HF} which is similar to shear modulus G and the structural relaxation time, τ, that defines a value for the displacement $x(= v_x\tau)$. Within that period of time, τ, liquid resistance feels like solid resistance. The shear stress for liquid will be written as: $\sigma = G_{HF}\gamma$ or:

$$\sigma = G_{HF}\tau \frac{d\gamma}{dt} \tag{4.3}$$

Maxwell viscosity's equation for liquid can then be simplified in a formula that helps to square elastic and viscous behaviour:

$$\eta = G_{HF}\tau \tag{4.4}$$

4.2 Strong and fragile liquids

Angell has proposed a plot of viscosities of glass-forming liquids in logarithm scale versus normalized temperature scale [2]. All viscosity curves have two common points at the two

ends . At the glass transition, T_g, the viscosity is defined to be $10^{12}\,Pas$. At the highest temperature, the viscosity is related to the vibrational dynamics. Strong liquids, whose viscosities in logarithm versus. T_g/T increases constantly have an Arrhenius viscosity-temperature relation (i.e. a straight line). Fragile liquids show a high rate of change in viscosity with respect to the temperature as the glass transition is approached (figure 2.7). The non-Arrhenius behaviour is expressed empirically in the Tamman, Vogel, Fulcher (TVF) equation [14]:

$$\eta, \tau = A \exp \frac{B}{T - T_o} \tag{4.5}$$

where A, B and T_o are constant; T_o is often equated with the Kauzmann temperature [18], the lowest limit of the glass transition temperature. The change rate of viscosity near glass transition temperature can be quantified by an index called fragility, m. This is the temperature sensitivity of viscosity in the liquid state at T_g and is defined by:

$$m = \left(\frac{d(log\eta)}{d(T_g/T)} \right)_{T_g=T} \tag{4.6}$$

This value is, in fact, calculated from the slope of viscosity curve in Angell plot at $T_g/T = 1$. Liquids of fragility $m \approx 20$ like silica are called "strong" while the "fragile" liquids like the heavy metal halides, ZBLA, for instant, have $m \approx 200$ [14].

4.3 Methods of measuring shear viscosity

4.3.1 Traditional methods for Newtonian liquids

Falling ball viscometer

This method can measure viscosities in the range of $1-10^6 Pas$. In this method, a solid ball of radius r and density ρ_b, drops under the effect of gravity in a vertical cylinder containing Newtonian liquid, with density ρ and viscosity η which is then measured. With a correct setup, the ball will reach the terminal (and constant) velocity, V, measured by the time it takes to pass two marks on the cylinder (figure 4.2 a). The fundamental principles of

dynamics are applied to the ball with three following external forces: 1. gravity force, given by $(4/3)\pi r^3 \rho_b g$, where g is the acceleration of free fall; 2. buoyancy force, given by $(4/3)\pi r^3 \rho g$; 3. drag force, given by $6\pi r \eta V$. The ball reaches the final velocity, at zero acceleration, when all external forces are balanced:

$$(4/3)\pi r^3 \rho_b g - (4/3)\pi r^3 \rho g = 6\pi r \eta V \tag{4.7}$$

This equation is called Stoke's law. The viscosity of the liquid at the temperature of the experiment can be calculated from the equation:

$$\eta = \frac{2}{9}\frac{\rho_b - \rho}{V} r^2 g \tag{4.8}$$

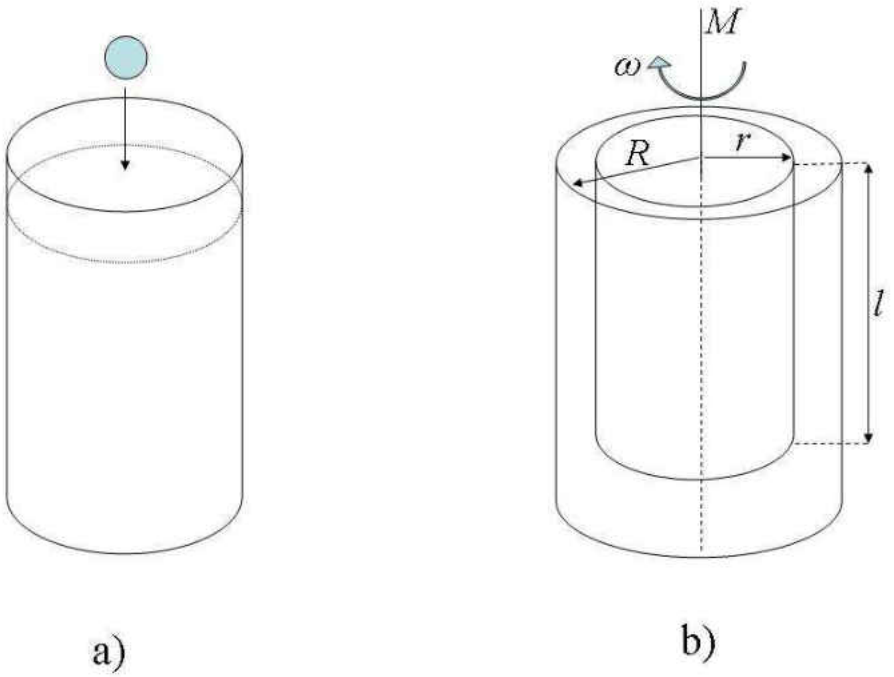

Figure 4.2: Viscosity measurement in traditional methods: *a*) falling ball viscometer and *b*)rotation viscometer

Rotation viscometer

The apparatus contains two coaxial cylinders of radius r and R, filled in between with the liquid that is to be measured. Torsion acts upon either the inner cylinder (length l) or the outside crucible. The viscosity is calculated from the relation:

$$\eta = \frac{M}{4\pi\omega l}\left(\frac{1}{r^2} - \frac{1}{R^2}\right) \tag{4.9}$$

where M is the measured torsion couple and ω the angular velocity. This method requires a large amount of sample.

The traditional methods are well understood and reliable. However, they are generally not suitable for ultrahigh temperature liquid and/or with small amount of sample. This can not allow the supercooled liquid to be accessed due to the nucleation by contact between sample and furnace.

4.3.2 Novel method using levitating furnaces for ultrahigh temperat liquids

In contactless conditions, the sample can be maintained at molten and supercooled liquid states without crystallisation. The sample is levitated by means of an electric, magnetic or mechanical force that opposes gravity (section 3.2). Viscosity and surface tension are measured by using the behaviour of sample vibration around its shape in equilibrium. In these methods, the molten sample is brought to the selected temperature then excited to vibrate. Different excitation ways can be used for the sample vibration, such as electric for electromagnetic levitator, acoustic for aerodynamic levitator etc. In scanning the excited frequencies, the response of the droplet exhibits a resonance peak. The position of the peak is related to the surface tension (restoring force) and density (inertial effect), whereas the peak width is governed by the dissipative energy (the viscosity of the liquid).

The resonance frequencies Ω and the full width at half maximum (FWHM) of reso-

nance peak $\Delta\Omega$ for a free oscillating droplet of volume V, radius R, surface tension σ, density ρ, and viscosity η in the vibrational mode l are written in formula [41]:

$$\Omega = \sqrt{\frac{l(l-1)(l+2)\sigma}{3\rho\pi V}} \tag{4.10}$$

$$\Delta\Omega = \frac{(l-1)(2l+1)\eta}{2\pi\rho R^2} \tag{4.11}$$

In magnetic levitation technique, the effects of the magnetic and gravitational fields on the oscillation frequencies of the drop can be calculated allowing an accurate surface tension measurement to be made [42]. The effect of gravity and gas flux on the shape in equilibrium is also evaluated [43] to investigate the real shape of the drop instead of the ellipsoidal approximation. The mode $l = 1$ represents the translational movement of

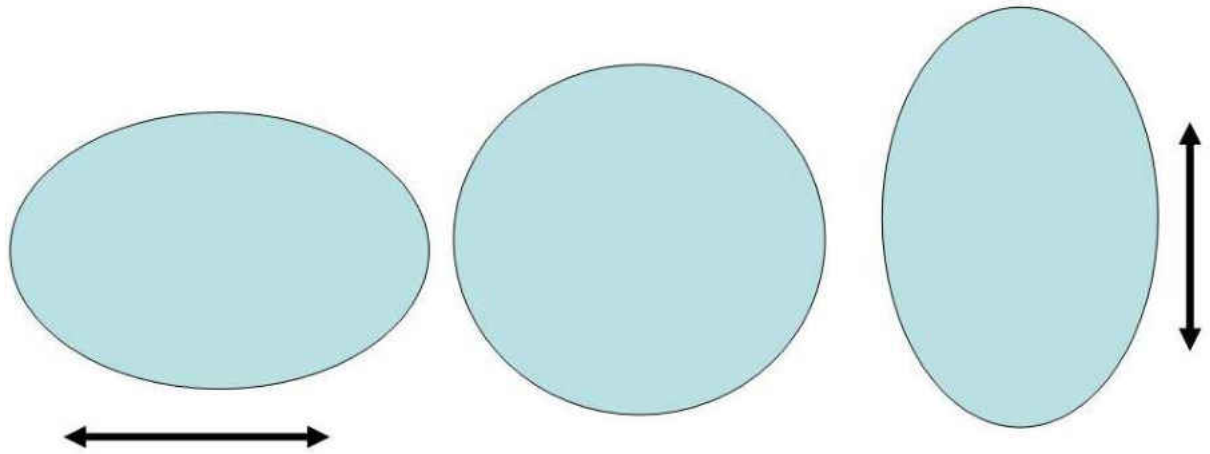

Figure 4.3: Geometry of $l = 2$ oscillation mode. Liquid drop oscillates in vertical and horizontal movement. This mode contains most kinetic energy from the oscillation and therefore exhibits strong vibrational amplitudes.

sample and needs to be normalized in the measurements (section 3.4). Figure 4.3 shows the geometry of $l = 2$ oscillation mode (oscillation between probate and oblate shapes). This mode contains the most kinetic energy. Other oscillation modes with $l > 2$ are not observed because of their strong damping. The $l = 2$ mode has been investigated in

our aerodynamic levitator (figure 4.4). Lord Rayleigh [44] was the first to introduce the relation of the resonant frequencies, Ω to the surface tension σ for $l = 2$ mode:

$$\sigma = 3\pi m\Omega^2/8 \tag{4.12}$$

where m is the drop weight. This equation has been used by Glorieux [45]

The equivalent formula for viscosity is:

$$\eta = \frac{2\pi}{3}R^2\rho\Delta\Omega \tag{4.13}$$

and has been used by Perez *et al* [43].

Density is an important factor in the accuracy of surface tension and viscosity measurements. By convention, density is the ratio of the weight m of sample over its volume V. In video imaging of a drop with a spherical approximation, the density can be measured by knowing the weight and cross-section area ($S = \pi R^2$) of the sample. The relation between the cross-section area S and the sphere volume V can be easily expressed:

$$S = \sqrt[3]{\frac{9\pi V^2}{16}}; \quad V = \sqrt{\frac{16S^2}{9\pi}} \tag{4.14}$$

The cross-section areas needs to be calibrated with a sample of well-known size and density. The alumina spheres at room temperature are now commercially available with different diameters such as 1.000, 1.500, 2.000 mm of high precision ($\pm 2.5\mu m$). The density of the alumina sphere at room temperature was calculated from its weight ($16.6 \pm 0.1mg$) and diameter ($2.000 \pm 0.002mm$):

$$\rho_{RT} = \frac{m}{V} = \frac{m}{4/3\pi R^3} \tag{4.15}$$

and we use this value to calibrate the density of alumina at different temperatures. The cross-section areas of sample images at room temperature and at higher temperature, T, respectively S_{RT}, S_T are measured in pixels. Figure 4.8 shows the screenshot of our written LABVIEW program which calculates the number of pixels that the sample image

covers. The relationship of the sample densities at temperature T and room temperature can be seen in the formula:

$$\rho_T = \rho_{RT} \left(\frac{S_{RT}}{S_T} \right)^{3/2} \tag{4.16}$$

4.3.3 Adaptation of Aberystwyth aerodynamic levitator for viscosity surface tension, and density measurements

The detail description of Aberystwyth aerodynamic levitator has been written in the previous section (section 3.2). Figure 4.4, adapted from figure 3.4, shows the setup of the aerodynamic levitator combining a high-speed camera and a double-piezo.

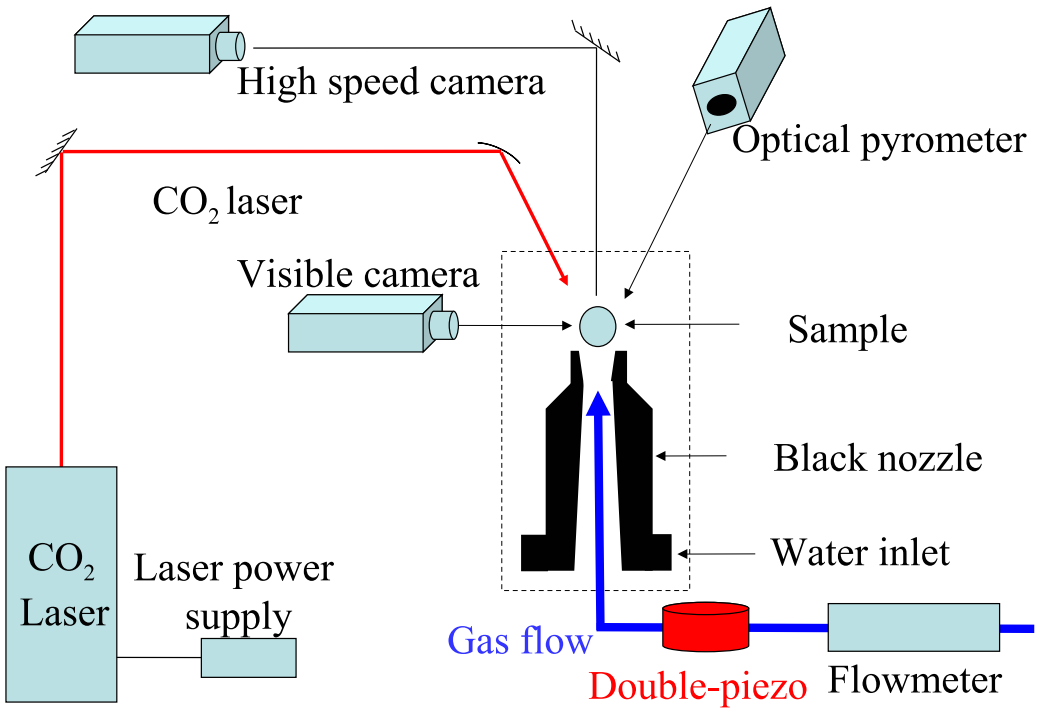

Figure 4.4: Levitator setup for density, surface tension and viscosity measurements of molten and supercooled liquid alumina adapted from figure 3.4 using high-speed camera. Double-piezo (figure 4.6) is integrated into the gas flow. It creates sound waves of variable frequencies controlled via a frequency generator.

The high-speed camera is used to record sample images. The speed of recording can vary between $10\,f.s^{-1}$ (during several hours) up to $37000\,f.s^{-1}$ (during $1.5\,s$). We use a $105\,mm$ lens with magnification 3X to record sample images within 256x256 pixel area in the CCD detector of the high-speed camera. A flat mirror is placed on the top of the sample with 45 degrees of inclination, allowing the high-speed camera to view the sample images from the top (figure 4.4). This design is useful as it keeps the high-speed camera in a stable horizontal position. The aluminium nozzle was painted black in order to increase the contrast between the bright sample and the background (black nozzle). The view from the side is limited by the nozzle (the bottom part of the sphere is inside the cone). The setup of the high-speed camera is seen in figure 4.5.

The double-piezo is used to generate accoustic waves. In viscosity and surface tension measurements, an eternal excitation that enables the sample to oscillate is necessary. This perturbation needs to vary in frequency over a wide range in order to excite the main resonant frequencies of the liquid drops. Our samples are in general refractory oxides, therefore not suitable for electrical and/or magnetic perturbation as these methods require free charge within the sample. To enable refractory samples to be vibrated, acoustic perturbations are introduced in the gas flow via a double-piezo connected to a frequency generator. The driving frequency, ν, sweeps in order to find the resonant frequencies at different temperatures. The gas from the mass flow passes through a double-piezo that can be excited from a generator that generates frequencies in a wide range covering the region of interest, 0-1000 Hz. An acoustic wave interacts with the sample in the vertical direction from bottom to top, in the same direction as the gas flow in order to excite the mode $l = 2$ more strongly.

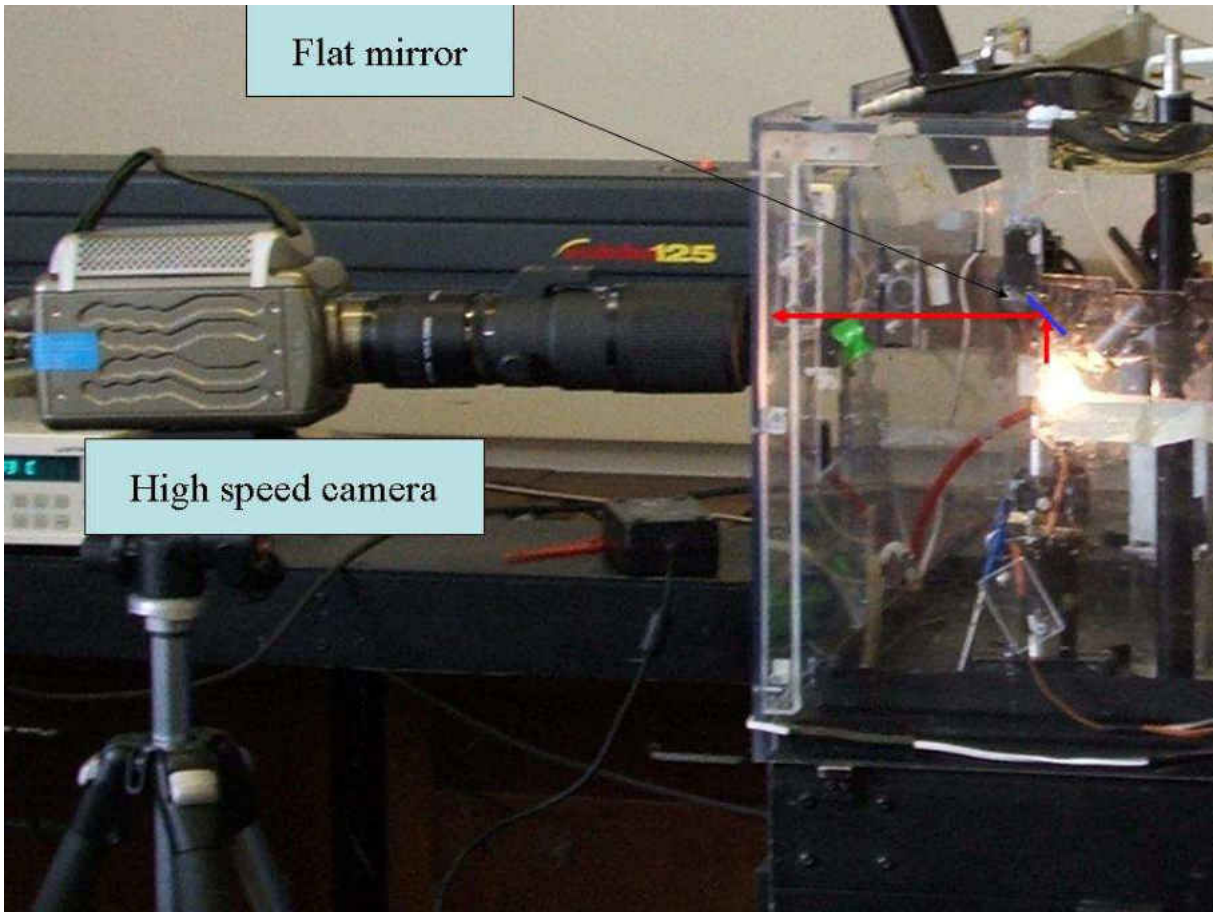

Figure 4.5: The high-speed camera records images of alumina drop in a horizontal position through a mirror of 45 degree inclination. The images recorded are in fact the view from a vertical direction. This design allows the high-speed camera to record images in wide field in a stable, horizontal position. This is suitable to integrate with a synchrotron radiation experiment as the wide-angle detector is placed above sample.

4.4 Experimental conditions and imaging analysis

4.4.1 Density measurements

The accuracy in density measurement depends on the sphericity of the sample so we have achieved these measurements using stable conditions, i.e. without any external perturbations. At low temperature, the sample is stable but when the temperature increases, the sample shows complex movements including vibration, oscillation and translation. For each temperature, the sample is levitated over a long period, typically 40 s, at recording rate 4000 $f.s^{-1}$. This method can increase the signal/noise ratio in calculating the

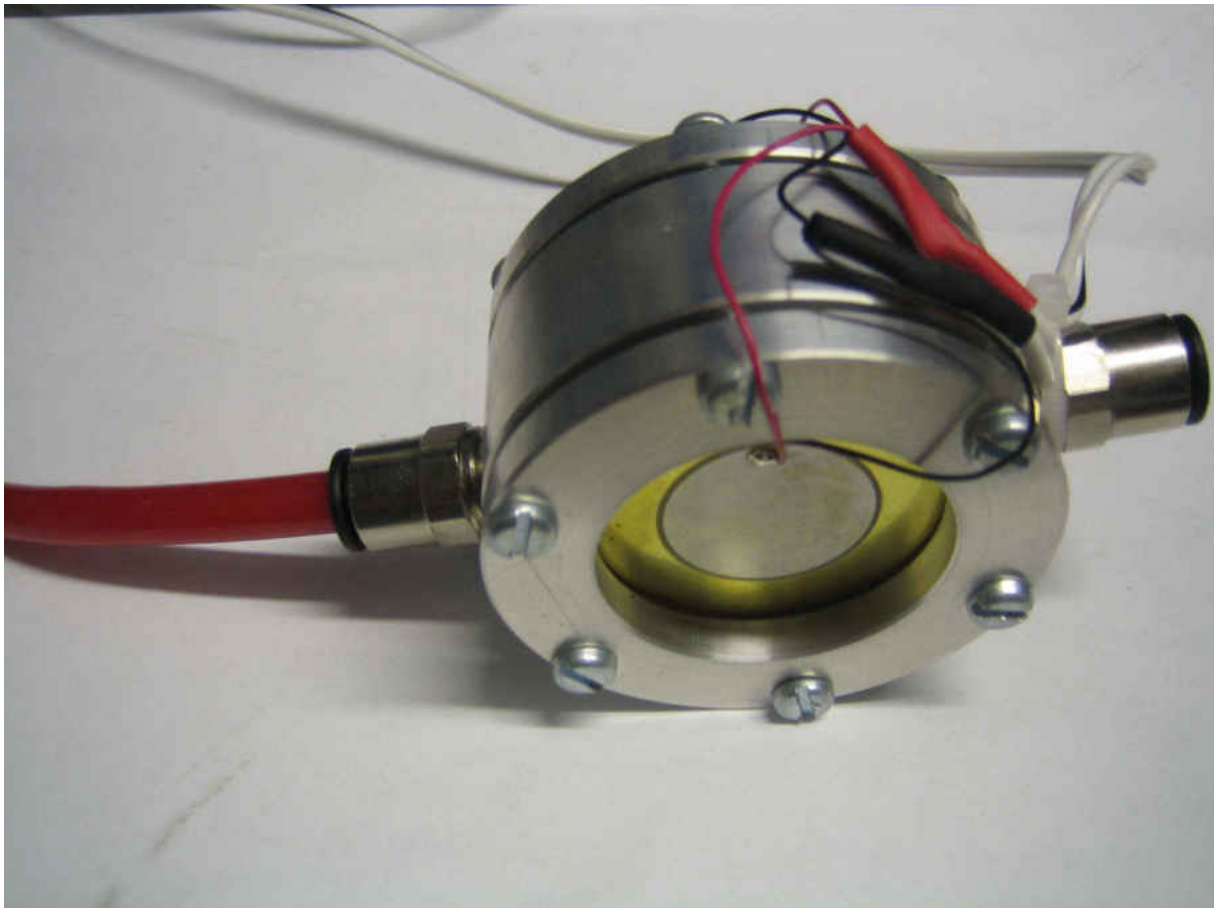

Figure 4.6: Built double-piezo used to generate acoustic waves of variable frequencies controlled via a frequency generator.

cross-section area of sample significantly.

The alumina sphere with a high precision of diameter $2.000 \pm 0.0025mm$ was first levitated for calibration purposes. Then the sample was brought to a fixed temperature (via laser power control). Data were obtained at discrete temperatures rather than continuously as in previous investigation [12, 13]. We have also attempted few measurements with a slow ramping of laser power and recorded the sample images within a wide range of temperatures. However, this method does not define accurately the corresponding temperature for specific recorded images. The sample temperature was measured from the top as shown in figure 4.4. Due to the directional nature of laser heating, it is hard to get a uniform temperature in the whole sample. The cross-section area of the sample

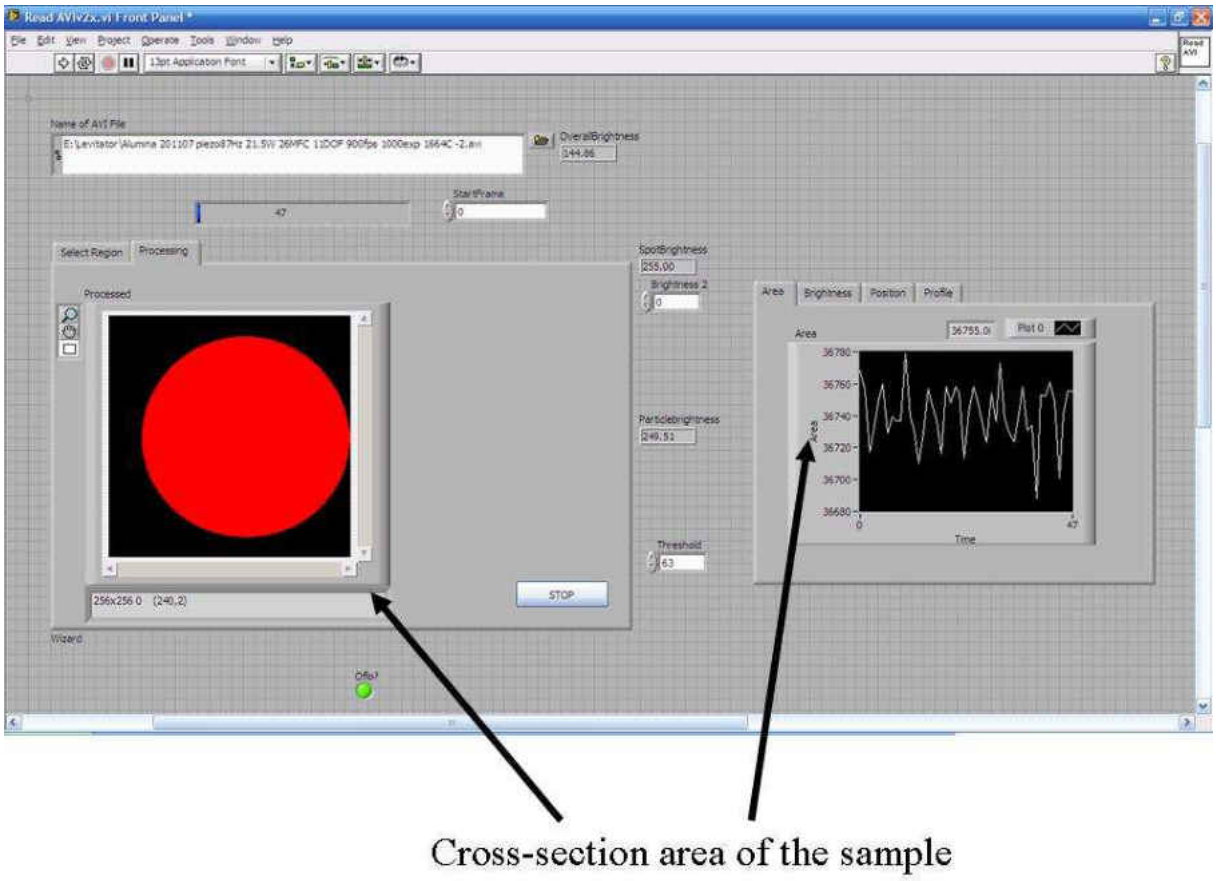

Figure 4.7: Screenshot of LabVIEW program which is used to measure the cross-section area of the sample. On the left, the whole sample image is shown in red. The program calculates the number of pixels that each picture covers on the screen. As the drop vibrates slightly, even without external excitation, the sum of pixels shown on the right, oscillates around an average value. Recording during 40 s with 65000 pictures gives a high static and signal/noise ratio in calculating the cross-section area of sample. The noise comes mainly from the translational movement (oscillation mode $m = 1$)

was calculated from the average value of all recorded images for one temperature. This method allows high precision in determination of the cross-section area of the drop at each temperature.

4.4.2 Viscosity and surface tension measurements

The setup of the high-speed camera for viscosity and surface tension measurements is different from the one for density because in this case an external perturbation was necessary. In these measurements, we have chosen empirically the speed of recording at 900

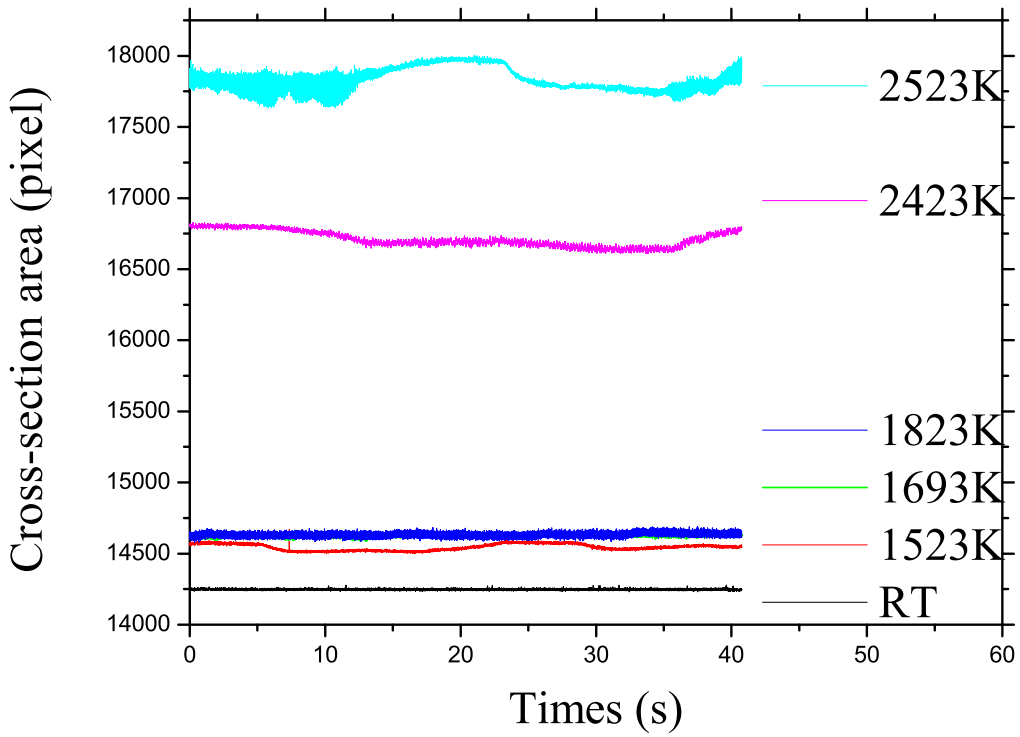

Figure 4.8: Cross-section areas in pixels are measured for each temperature. Raw data is shown for various temperatures which enables the density to be measured (equation 4.14 and 4.15). At room temperature, the value remains constant as the sample is spherical and stable. The effect of vibrational and translational movements of sample raise with temperature. Therefore, measuring the cross-section area at one temperature over a long period can increase the signal/noise ratio in the density measurement.

$f.s^{-1}$ during $72\,s$. This speed of recording allows the vibration of the liquid drops to be captured where the main resonant frequencies of alumina are within 0-1000 Hz range. This setup allows enough experimental time for adequate statistics and a correct exposure for different temperatures and luminosity. Measuring the cross-section area necessitates capturing the edge of the liquid drop. At ultrahigh temperatures, the sample is very bright so the aperture of the lens can be reduced in order to increase the depth of field. A clear picture of the sample can be obtained even in the case of translation.

Our recorded videos are in 2D so the idea of observing the vibration of liquid drop requires detecting the change in diameter of drop images. The video that records the process during scanning the driving frequencies, ν, is then digitalized in 65000 pictures for image processing. We have written the program based on IDL software to calculate the diameter of the sample in the horizontal and vertical directions. It is based on counting the average brightness in a defined line. However, during the experimental process, the sample was moving slightly out of its equilibrium position. In order to take the real change in diameter of the sample, the average diameter of the sample was subtracted from the measured diameter. Figure 4.9 shows a series of digitalized pictures of alumina drop at 2408K during vibrations. The change in diameter of the sample is relatively small and appears unclear to the naked eye.

The amplitude of the diameter change is then plotted versus the driving frequencies (figure 4.10). Vibrational amplitude of the alumina sample in five different temperatures is shown. A Lorientzian function has been used to fit the resonant peaks. As the vibrational amplitude is small, the resonant peaks maintain symmetry. When the temperature is lowered, they become broader in width and lower in height.

Assuming linear oscillation, the full width, $\Delta\Omega$, of the resonance peak was measured at half maximum through the Lorientzian equation:

$$I(\nu) = \frac{\frac{\Delta\Omega}{2}}{(\nu - \Omega)^2 - (\frac{\Delta\Omega}{2})^2} \tag{4.17}$$

where $I(\nu)$ is the resonant intensity defined as the square of oscillation amplitudes. The width of the resonant peak, $\Delta\Omega$, and the main resonant frequency, Ω, are used in the equation 4.12 and 4.13 to calculate the viscosity, η, and the surface tension, σ, of liquid alumina.The result is shown in table 4.1.

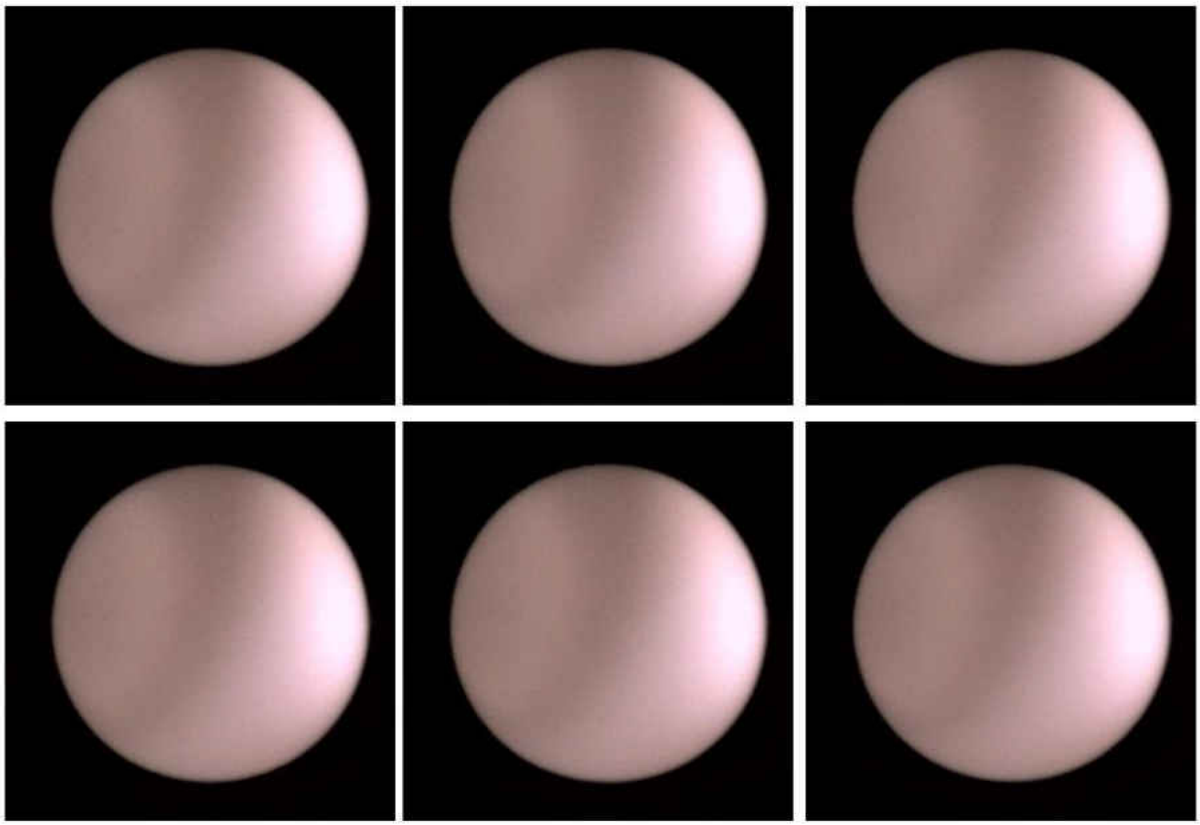

Figure 4.9: Sample images during vibration. These six pictures are collected at different moments within one period of drop oscillation at 2408 K. The changes in diameter of sample during vibration are relatively small and not obvious to the naked eye.

4.5 Results and discussions

4.5.1 Density

Using the high-speed camera, we have measured the density of alumina in both solid and molten states. They are plotted in figure 4.11. The measured densities of alumina are compared to the densities in crystalline state using X-rays diffraction by the National Institute of Standards and Technology (NIST)[11] and in molten and supercooled liquid regions by Glorieux *et al* [12]. The density in crystalline alumina of NIST is calculated from the mass and volume of one unit cell using parameters *a, b, c* of hexagonal unit cell resulting from X-ray diffraction peaks. In molten and supercooled liquid regions,

	2408 K	2220 K	2153 K	2018 K	1910 K
$\Omega(Hz)$	222 ± 1	185 ± 1	181 ± 1	75 ± 1	20 ± 1
$\Delta\Omega(Hz)$	9 ± 1	14 ± 1	20 ± 1	42 ± 1	140 ± 1
$\mu(mPa.s)$	52 ± 4	82 ± 4	117 ± 4	246 ± 4	820 ± 4
$\sigma(mN/m)$	0.96 ± 0.01	0.66 ± 0.01	0.64 ± 0.01	0.10 ± 0.01	0.007 ± 0.005

Table 4.1: Viscosity and surface tension of liquid alumina with their errors at different temperatures.The width of the resonant peak, $\Delta\Omega$, and the main resonant frequency, Ω, are calcutaled from the Lorientzian fit to the measured vibration amplitude of the sample. Using equation 4.12 and 4.13, the viscosity, η, and the surface tension, σ, of liquid alumina are obtained.

Glorieux *et al* [12] have measured the cross-section area of the sample on free cooling. At high temperature, the sphericity of the sample might affect the measured cross-section values hence the densities. The systematic error comes mainly from the translational movement (oscillation mode $m = 1$). However, the alumina densities in our measurement were measured at fixed temperatures to reduce the noise especially at high temperature. With a close-packed structure and high purification of the sample, a good agreement between our results and NIST values in the solid state suggests the reliability of this method. The highest temperature in the crystalline state that our method can reach is 2000 K or about 300 K below melting point, T_m=2323 K because the sample starts to melt partially at that temperature. The data at two temperatures below the melting point are collected in the supercooled region by reducing the temperature of molten alumina slowly via laser power control. The loss in mass of the sample by being heated over the experimental period is less than 0.05% which is smaller than the systematic error from the translational movement especially at high temperature. The change in density of our measurements between solid and liquid states at melting point is smaller than the difference between [11] and Glorieux *et al* [12] values. We believe our values are more reliable than Glorieux *et al* as our measurements were made at fixed temperatures.

4.5.2 Viscosity and surface tension

The temperature range possible with the levitator covers 500 degrees and extends 250 degrees lower in the supercooled region compared to other works [13, 46]. The lowest temperature is defined when crystallization occurs. From the Lorentzian fit, equation 4.17, peak width and peak position of resonant peaks in figure 4.10 have been calculated for each temperature. The result as shown in table 4.1 also included the calculated value for viscosity η (equation 4.13) and surface tension σ (equation 4.12). In the common temperature range, 2200K-2400K, our viscosity values are in good agreement with the literature [13, 46].

On a logarithm scale, good consistency is obtained with our experiments and the TVF expression, equation 4.5. The TVF curve needs at least 3 points to be created because if T_g is known, three unknowns A, B, T_0 remain to be determined. The TVF curve starts from the point at very high temperature, $T \to \infty$ or $T_g/T = 0$ with an assumed value of viscosity $10^{-3}\,Pas$.

From Maxwell's viscosity equation 4.4 with shear modulus for alumina, $G_{HF} = 30.10^9\,Pa$, this value of viscosity corresponds to the relaxation time $\tau = 3.10^{-14}\,s$ that is equivalent to phonon frequency $\nu = 3.10^{13}\,Hz$. That frequency is commonly found in glassy systems in the middle of vibrational density of states [14]. The second point at $T = T_g$, relates to viscosity η reaching a value of $10^{12}\,Pa$ at which, by convention, a liquid becomes glass. The third point is taken at T= 2350 K, $\eta = 30m\,Pa$. With an empirical assumption of $T_g \backsimeq 2/3T_m = 1521$ K, those points give values of A, B, T_0 of $10^{-3}\,Pa$, 3400 K and 1431 K respectively. The fragility is calculated from the slope of TVF curve, equation 4.6 , when $T \to T_g$ for alumina, $m \approx 180$, indicates that liquid alumina is very fragile and comparable to metal halides (figure 2.7). Compared to alumina, YAG behaves as a less fragile liquid. The result for YAG is taken from [47].

Surface tension of molten and supercooled liquid alumina in this work is compared with the work of Paradis *et al* [13]. From figure 4.10, the main resonant frequencies shift to lower values as the temperature decreases, suggesting that the surface tension tends to lower values as the drop becomes more viscous. In the temperature range 2100-2400 K, figure 4.13, the agreement is reasonable. The sharp fall of the surface tension at supercooled temperatures is unexpected and may be due to the synchronization of the high-speed camera and the frequency generator at the start of the recording.

4.6 Conclusions

The density of alumina measured using the aerodynamic levitator shows a good agreement with standard values in the crystalline state. In the molten and supercooled states, we believe our measurements are more reliable than earlier experiments using free cooling [12]. The difference at the melting point is 23.3 % and relates to the change in atomic structure between α-Al_2O_3 and l-Al_2O_3 [14]. Viscosity values fit well with TVF curve to a value of fragility $m = 180$ for l-Al_2O_3. Surface tension values are comparable with the literature value [13] within the common temperature range, 2200-2400 K.

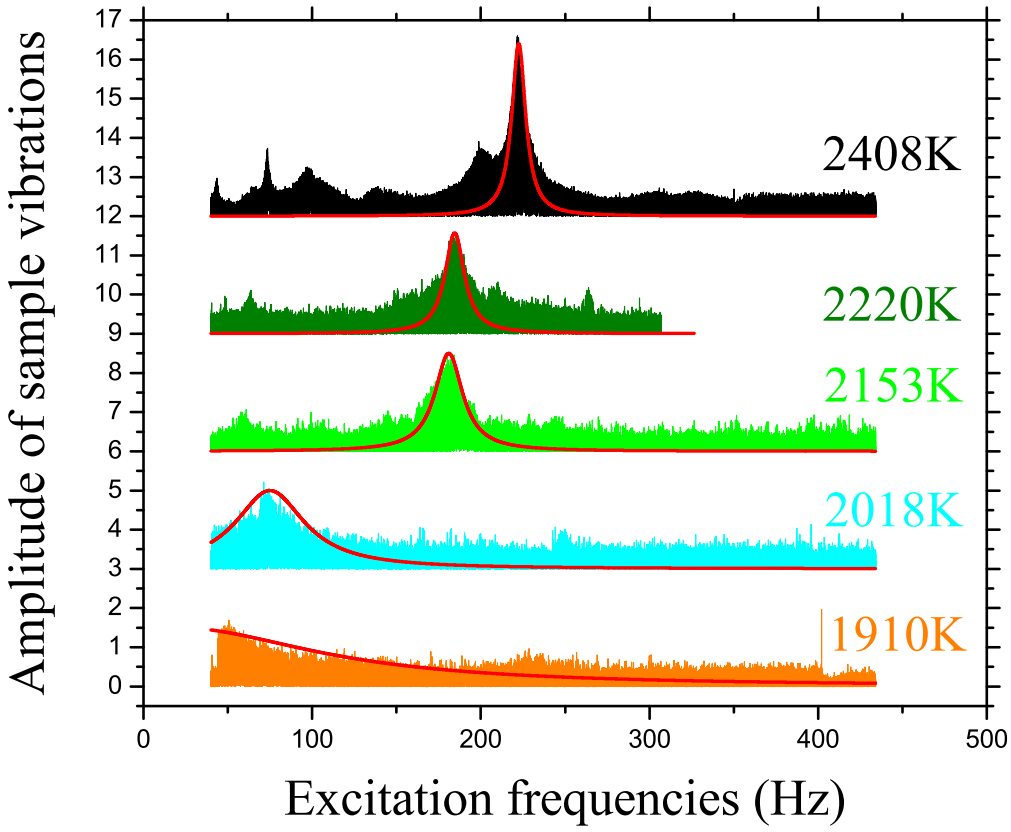

Figure 4.10: Raw data of vibrational amplitudes of alumina sample at five different temperatures. Obviously, the main frequencies shift left as temperature decreases suggesting the surface tension tends to lower value as the drop become more viscous. Lorientzian function, equation 4.17, has been used to fit resonant peaks. Adapted data are shown by the solid curves. As the vibrational amplitude is small, resonant peaks maintain symmetry. When the temperature is lowered, resonant peaks are broader in width and lower in height.

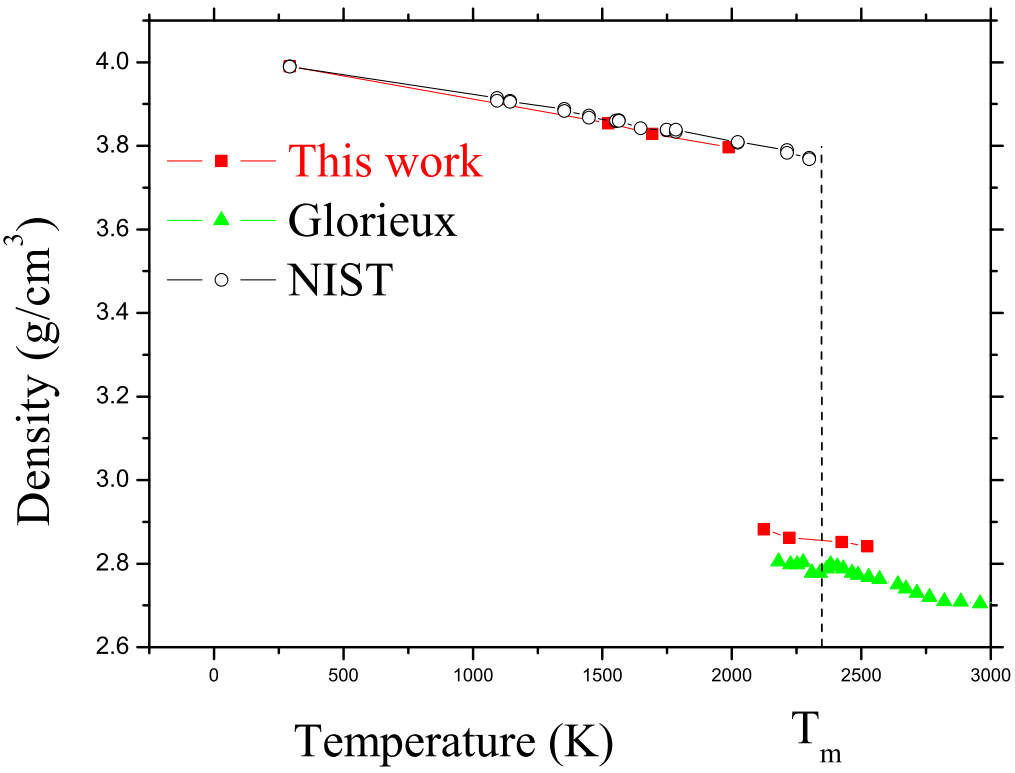

Figure 4.11: Density of alumina in crystalline, molten and supercooled states. Alumina density in crystalline state of National Institute of Standards and Technology (NIST)[11] has been calculated using X-rays diffraction Density is calculated from the mass and volume of one unit cell using parameters *a, b, c* of hexagonal unit cell resulting from X-ray diffraction peaks. In molten and supercooled liquid regions, Glorieux *et al* [12] have measured the cross-section area of the sample in free cooling.

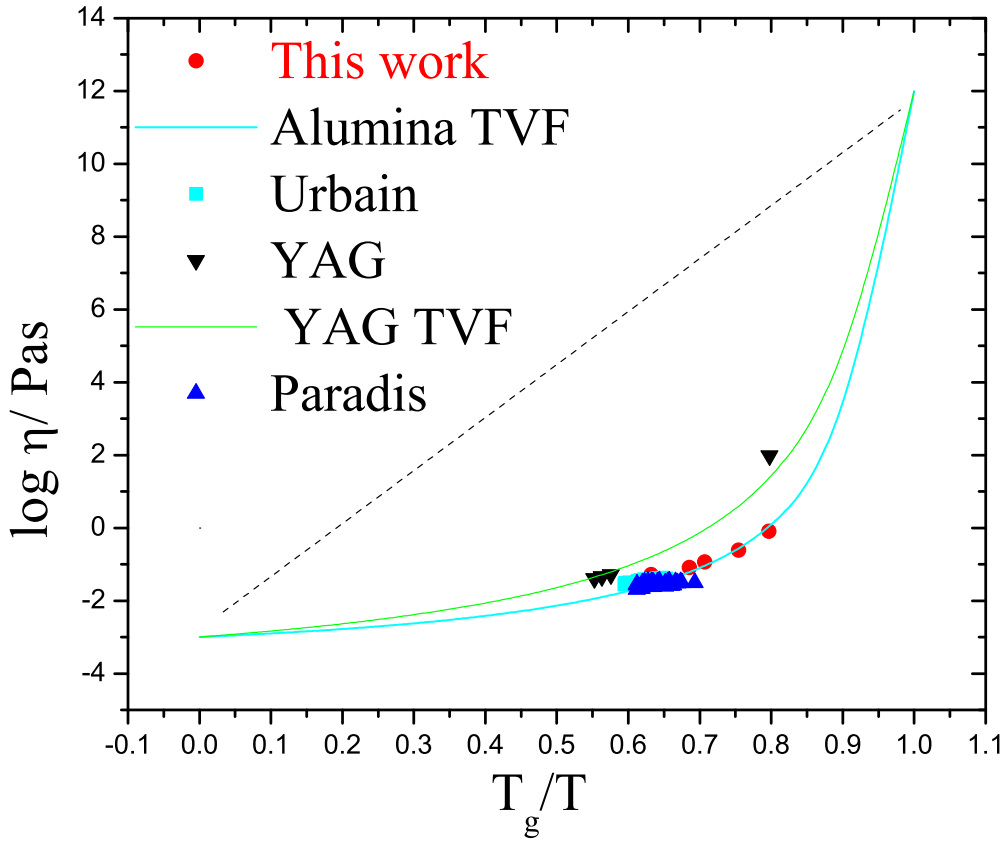

Figure 4.12: Viscosity of alumina in molten and supercooled states from our work and from the literature [13, 46]. In comparison to YAG, alumina liquid behaves as a more fragile liquid. The fragility is calculated from the slope of TVF curve equation 4.6 , when $T \rightarrow T_g$. Other compositions such as AY20 will fall in between exhibiting intermediate fragilities.

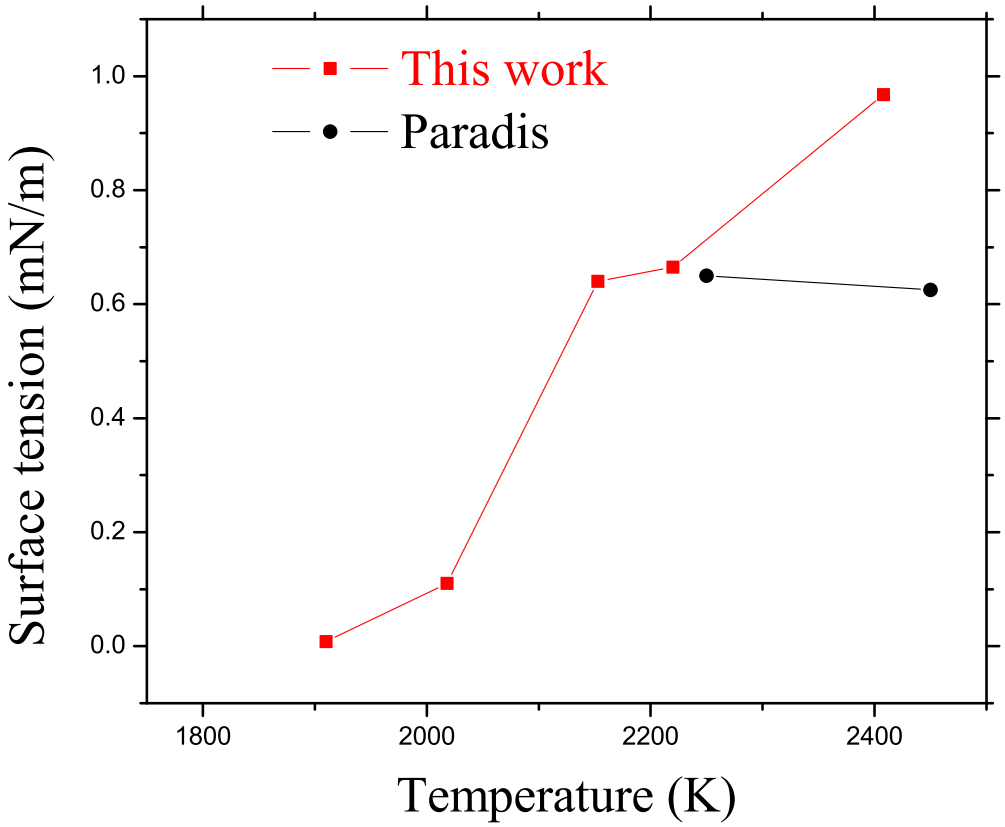

Figure 4.13: Surface tension of molten and supercooled liquid alumina in this work is compared with the work of Paradis *et al* [13]. Surface tension is calculated by introducing into the equation 4.12 the main frequencies found from Lorentzian fit, equation 4.17 and figure 4.10.

Chapter 5

Density Fluctuations in Molten and Supercooled Liquid Alumina

5.1 Introduction

The study of density-fluctuations in the supercooled liquids and in glassy states is important in investigating dynamic anomalies in the supercooled liquid state and at the glass transition, T_g. Mode coupling theory (MCT) has provided an advanced description of the transition from an ergodic liquid to the non-ergodic glassy state of matter. Experimentally this occurs above T_g, typically $1.2\,T_g$. There is a contrast in fluctuations in density and hence electron density. The small-angle X-ray scattering (SAXS) technique (section 3.6) can be used in this study to detect these inhomogeneities in liquids and glasses. SAXS has been employed to measure these phenomena in molten and supercooled alumina.

5.2 Long range order and density fluctuations

A long range order in glasses is governed by the density fluctuations quenched from the liquid state. Maintaining a liquid or fluid in thermodynamic equilibrium at ambient pressure necessarily involves fluctuations $\langle \Delta\rho^2 \rangle$ in the average density ρ_o, distributed in space and time. The magnitude of these fluctuations increases linearly with increasing temperature. The volume of fluctuating elements, V, is dictated by the bulk compressibility of

the liquid, K_T [21].

$$V \left\langle \Delta\rho^2 \right\rangle / \rho_o^2 = k_B T K_T \tag{5.1}$$

where the formula and unit of the compressibility of the liquid are:

$$K_T = -\frac{1}{V}\frac{dV}{dP} \quad (Pa^{-1}) \tag{5.2}$$

When the temperature decreases, the diffusional processes decrease but the compressibility stays approximately constant. As a result, the size of density fluctuations $V \langle \Delta\rho^2 \rangle / \rho_o^2$ decreases linearly with temperature.

5.3 Mode coupling theory and non-ergodicity

The basic concept of MCT [48] is the *cage effect* for which, on approaching the glass transition, the molecular motion of a particle will be constrained by surrounding ones. The particle can vibrate rapidly within this cage-like area till a momentary structural change enables it to escape away from this region. As the temperature decreases, the diffusion process becomes slower than the vibration one while they are comparable at high temperature where the liquid is in thermodynamic equilibrium and is therefore ergodic. MCT identifies the fast dynamic processes β corresponding to the motion of atomics or molecules inside cage-like regions, and slower α processes that control the creation or annihilation of those regions. MCT predicts a critical temperature T_c (typically T_c=1.2 T_g) at which an ergodic non-ergodic transition occurs as the temperature is lowered [49].

The degree to which the liquid is non-ergodic at temperature T can be expressed through the non-ergodicity factor $f(Q,t)$ at time t, where Q is the momentum transfer of the incoming waves (neutrons, X-rays, light) in scattering experiments:

$$f(Q,t) = \frac{F(Q,t)}{S(Q)} \tag{5.3}$$

where $F(Q,t)$ is the density-density correlation function and $S(Q)$ is the static structure

factor. When the time-scale tends to infinity, the non-ergodicity equates to the Debye-Waller factor, i.e:

$$f(Q, t \to \infty) = e^{-<\mu^2>Q^2/3} \tag{5.4}$$

where $< \mu^2 >$ is the mean square displacement of the average atom about its average position. Approaching the low Q and long time limit ($Q \to 0, t \to \infty$), the non-ergodicity factor relates more directly with the Landau-Plazcek ratio, which is measured with light and X-ray scattering, viz:

$$f_0(T) = \frac{R_{LP}}{R_{LP} + 1} \tag{5.5}$$

It is possible to determine a dimensionless parameter, α, that shows how fast the non-ergodicity factor increases when the temperature is lowered [50]:

$$\alpha = \frac{T_g}{T R_{LP}} \tag{5.6}$$

α is measured from the slope of $f_0(T)^{-1}$ *vs* T/T_g in the formula:

$$f_0(T) = 1/(1 + \alpha T/T_g) \tag{5.7}$$

This illustrates the strong and fragile supercooled liquid in figure 5.1 where $f_0(T)$ is plotted up to the glass transition. Two examples of MCT temperature T_c are shown for B_2O_3 and CKN.

5.4 Characterising density fluctuations

5.4.1 Glass

The density fluctuations in glass gives an additional contribution in scattered intensity of X-rays or neutrons, $I(Q)$.

$$V \left\langle \Delta\rho^2 \right\rangle / \rho_o^2 = S(0)/\rho_o = I(0) / \left(\rho_o \sum_{\alpha}^{N} W_{\alpha\beta\ldots}^2 \right) \tag{5.8}$$

where $\sum_{\alpha}^{N} W_{\alpha\beta\ldots}^2$ is the average cross-section for the different atoms present, weighted according to the composition [14]. The amplitude of density fluctuations can be measured

through the extrapolation at $Q \rightarrow 0$ from the measured intensity. An empirical law of form:

$$I(Q) = I(Q \rightarrow 0) \exp(bQ^2) \tag{5.9}$$

fits with the data in a number of materials and in the large Q-range [51]. Such fits allow calculation of the scattered intensity at $Q \rightarrow 0$ from the linear regime resulting in equation 5.9, thus neglecting the low Q scattering increase. Figure 5.2 shows the SAXS signal in logarithm scale for molten silica at 1812K and vitreous silica at 379 K (dotted lines show the region where $I(Q) \propto \exp(bQ^2)$ applies)[15]. The equation 5.9 enables $I(Q \rightarrow 0)$ to be obtained for the limited range $0.4 < Q < 0.6\,\text{Å}^{-1}$ (between two vertical dash lines).

Density fluctuations can also be measured using Brillouin scattering from the Landau-Plazcek ratio R_{LP} which is the ratio of the integrated intensities of the central elastic line and the inelastic Brillouin doublet and

$$V \left\langle \Delta\rho^2 \right\rangle / \rho_o = \frac{(1 + R_{LP}) k_B T}{\nu^2} \tag{5.10}$$

where ν is the longitudinal sound velocity. Zarzycki [52] has shown how the fluctuating volume V and density contrast $V \left\langle \Delta\rho^2 \right\rangle / \rho_o$ can be separated using the two equations 5.8 and 5.10 from SAXS and Brillouin data. In the case of silica, V has a value of around 910^3 Å^3 suggesting the radius of scattering particles, $(3V/4\pi)^{1/3}$, is about $13\,\mathring{A}$ and $\sqrt{\langle \Delta\rho^2 \rangle}/\rho_o \approx 1\%$. Thus, the compressibility of silica at glass transition where these fluctuations are quenched can be estimated from equation 5.1. K_T works out to be $7.8\,10^{-11} Pa^{-1}$ [53].

5.4.2 Molten and supercooled liquids

The study of density fluctuations in molten and supercooled liquid of refractory materials has been achieved by several groups. For example, $(Y_2O_3)_x$-$(Al_2O_3)_{1-x}$ melts has been investigated by McMillan *et al* [54], and more recently by Greaves *et al* [53]. Our work on

molten and supercooled liquid alumina has used the laser-heated aerodynamic levitation technique [39] integrated with synchrotron radiation [55], where small and wide-angle X-ray scattering can be recorded simultaneously [56]. This furnace technique enables structure at nano (SAXS) as well as atomic (WAXS) scale to be studied *in situ*. As an example, molten and supercooled liquid $Y_2Al_6O_{12}$ whose melting temperature T_m=2173 K, SAXS has been measured at 2203 K and 1663 K. This is shown in figure 5.3a, where I(0) can be estimated from the linear range using equation 5.9. The linear behaviour similar to silica (figure 5.2) occurs in the range $0.17 < Q < 0.6\,\text{Å}^{-1}$. Note the increasing in SAXS intensity with temperature. The same data can now be plotted as $\log I(Q)$ *vs* $\log Q$ in figure 5.3b. This does not give a direct estimation of *I(0)*, however, it shows an obvious rise in *I(Q)* as $Q \rightarrow 0$. Figure 5.4 shows the integration of SAXS in the low Q regime $\int_{0.03}^{Q_{min}} I_{SAXS} Q^2 dQ$ between 1500 K and 2400 K. The linear increase with temperature indicates the behaviour of thermal fluctuations expected from equation 5.1.

5.5 Results

Figure 5.5 shows our SAXS data on molten and supercooled liquid alumina. The data was measured in SRS6.2 using the aerodynamic levitator. The process of removing the background has been described in section 3.6. The ideal background should be taken at the same temperature and the same synchrotron current for each measurement. In our measurements, the background is measured at room temperature. It could be one source for the systematic errors in the integration of SAXS intensities. The scattered intensities are also plotted as $\log I(Q)$ *vs* Q^2 in a wide range of temperature from 2423 K to 1848 K. The increase in SAXS intensity is linear with temperature and somewhat Q-independent. Minimum at $0.078\,\text{Å}^{-1}$ is comparable with $0.3\,\text{Å}^{-1}$ in silica[15]. Whilst density fluctuations in silica were reported as being about $20\,\text{Å}^{-1}$ in size, that suggests their size for alumina is

about 60-80 Å^{-1}. As the minimum position does change significantly over the temperature range of the experiments, the average size for alumina remains approximately constant. The larger size for liquid alumina compared to molten silica suggests alumina is more compressible (lower K_T), which would be consistent with a higher fragility. Observing in the same range of Q between two dash lines 0.17< Q <0.6 Å^{-1} (in Q^2 scale: 0.0289< Q^2 <0.36 Å^{-2}, figure 5.5a), we see that the linear region in SAXS intensity of l-Al_2O_3 is less obvious than $Y_2Al_6O_{12}$ or SiO_2. Figure 5.6 also shows an increase of SAXS intensity integration, $\int_{0.025}^{Q_{min}=0.078\,\mathring{A}} I_{SAXS}Q^2dQ$, of l-Al_2O_3. The low Q limit in SAXS integration, Q=0.025 Å is defined by the beam stop that prevents the direct X-ray beam from reaching the detector.

Figure 5.7 shows a comparison of $\int I_{SAXS}Q^2dQ$ versus T for liquid alumina and liquid yttrium aluminates. The slope of $\int I_{SAXS}Q^2dQ$ versus T in liquid alumina is greater than in yttrium aluminates liquid. From equation 5.1, $V\left\langle \Delta\rho^2 \right\rangle / \rho_o \propto T$ and therefore, if the temperature dependence of integrated SAXS is greater for liquid alumina than for yttrium aluminates liquid, the compressibility, K_T, might also be greater. It is interesting to note from figure 4.12, the fragility of alumina is also greater than YAG, suggesting that the fragile liquid might have greater compressibility than strong liquids.

5.6 Conclusions

Although the linearity of SAXS intensity of l-Al_2O_3 in plotting *logI(Q)* vs Q^2 (figure 5.5 is less obvious than $Y_2Al_6O_{12}$ (figure 5.3) or SiO_2 (figure 5.2), the integrating result from $\int_{0.025}^{Q_{min}=0.078\,\mathring{A}} I_{SAXS}Q^2dQ$ still shows an increase with temperature (figure 5.7). This comparison shows that the amplitude of density fluctuations, $\Delta\rho/\rho$, will increase with temperature more strongly for liquid alumina than for AY20 which is the stronger liquid (figure 4.12).

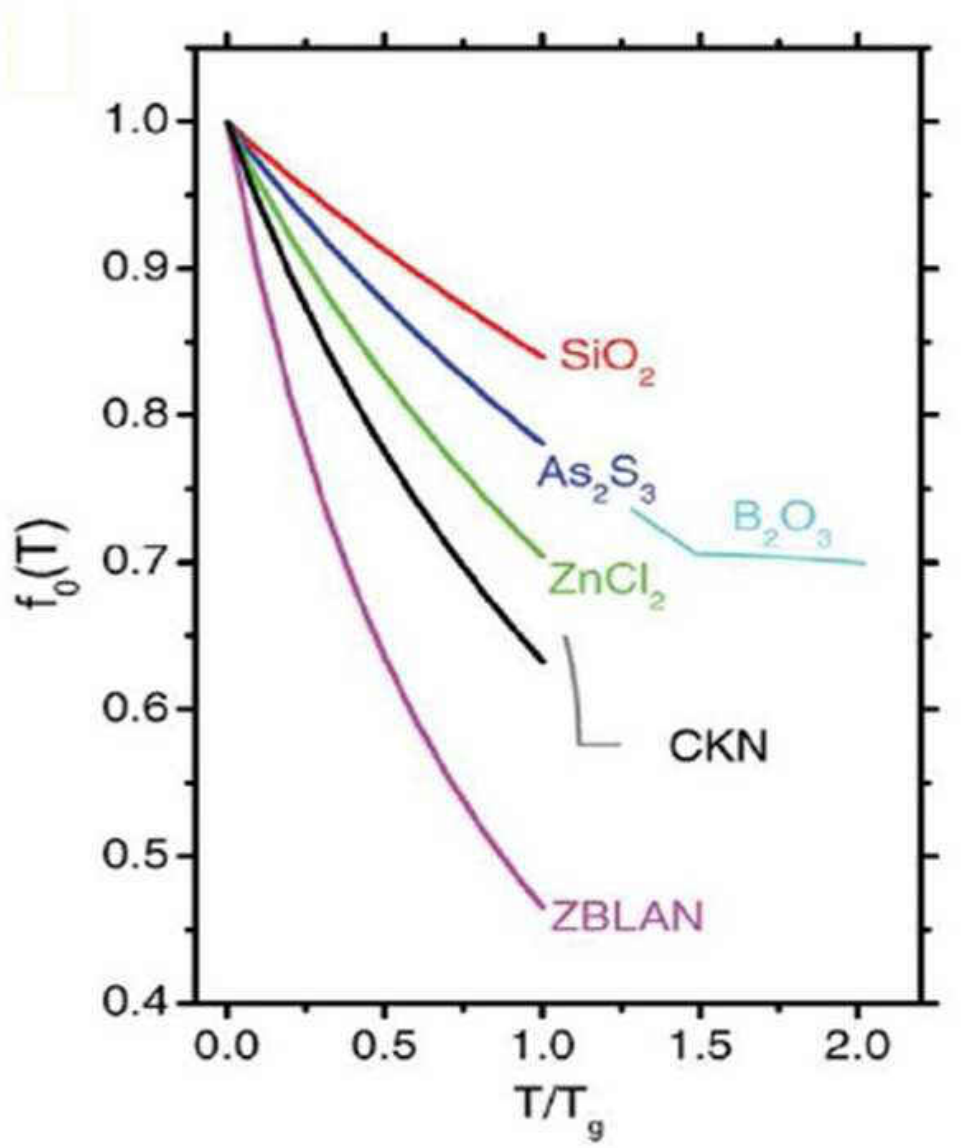

Figure 5.1: Non-ergodicity factor, f_0, for various inorganic glasses [14] versus normalized temperature T/T_g. As the temperature rises, non-ergodicity decreases to the plateau at T_c above T_g where ergodic- non-ergodic transition is predicted by MCT. These plateaus are seen in B_2O_3 and $2Ca(NO_3)_2$-$3KNO_3$(CKN)

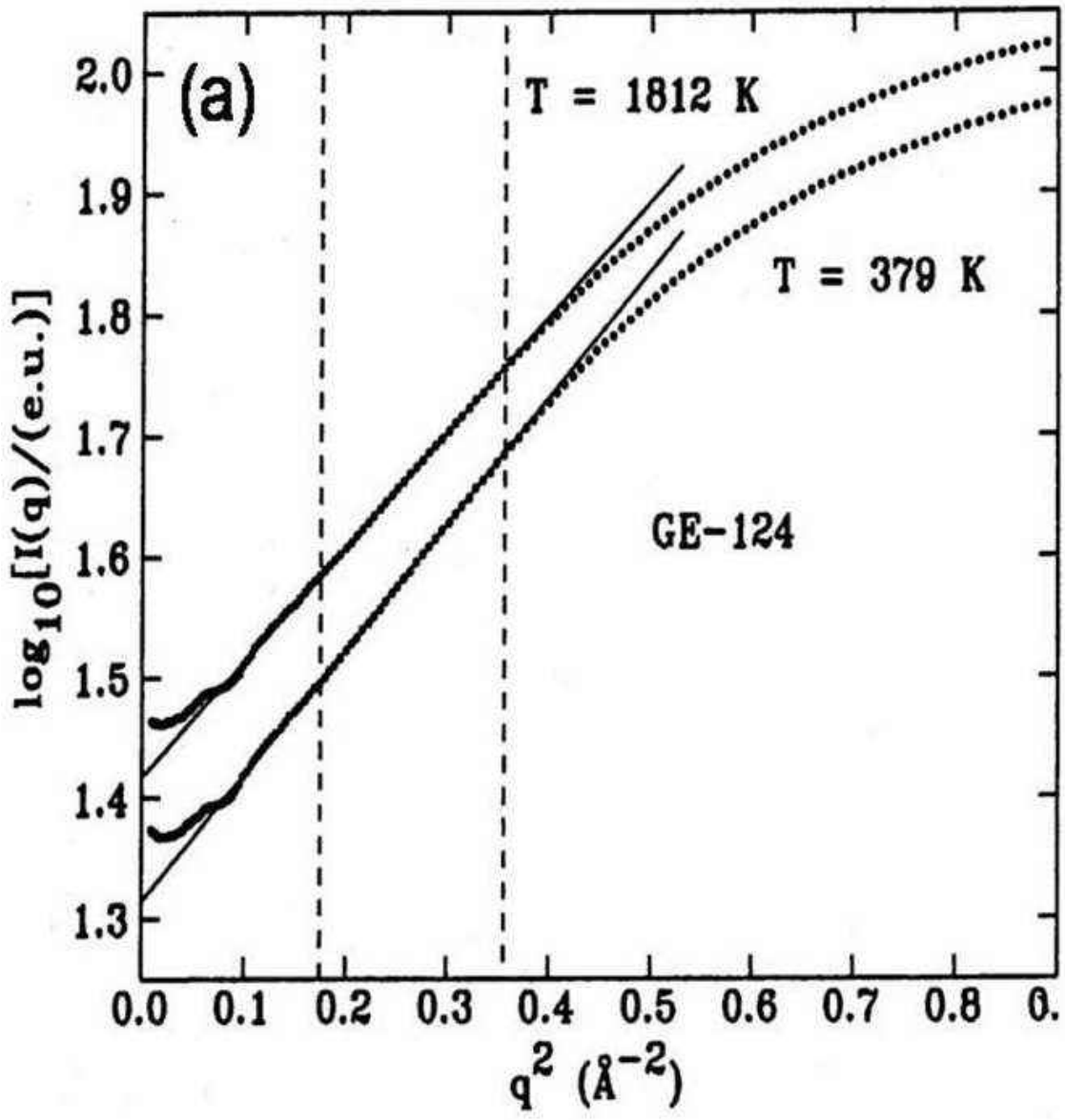

Figure 5.2: Density fluctuations and their temperature dependence measured in silica using small angle X-ray scattering at the ESRF. Log$I(Q)$ versus Q^2 at the base of structure factor for glass and liquid [15]. $I(Q)$ is estimated, the rise with T following equation 5.9

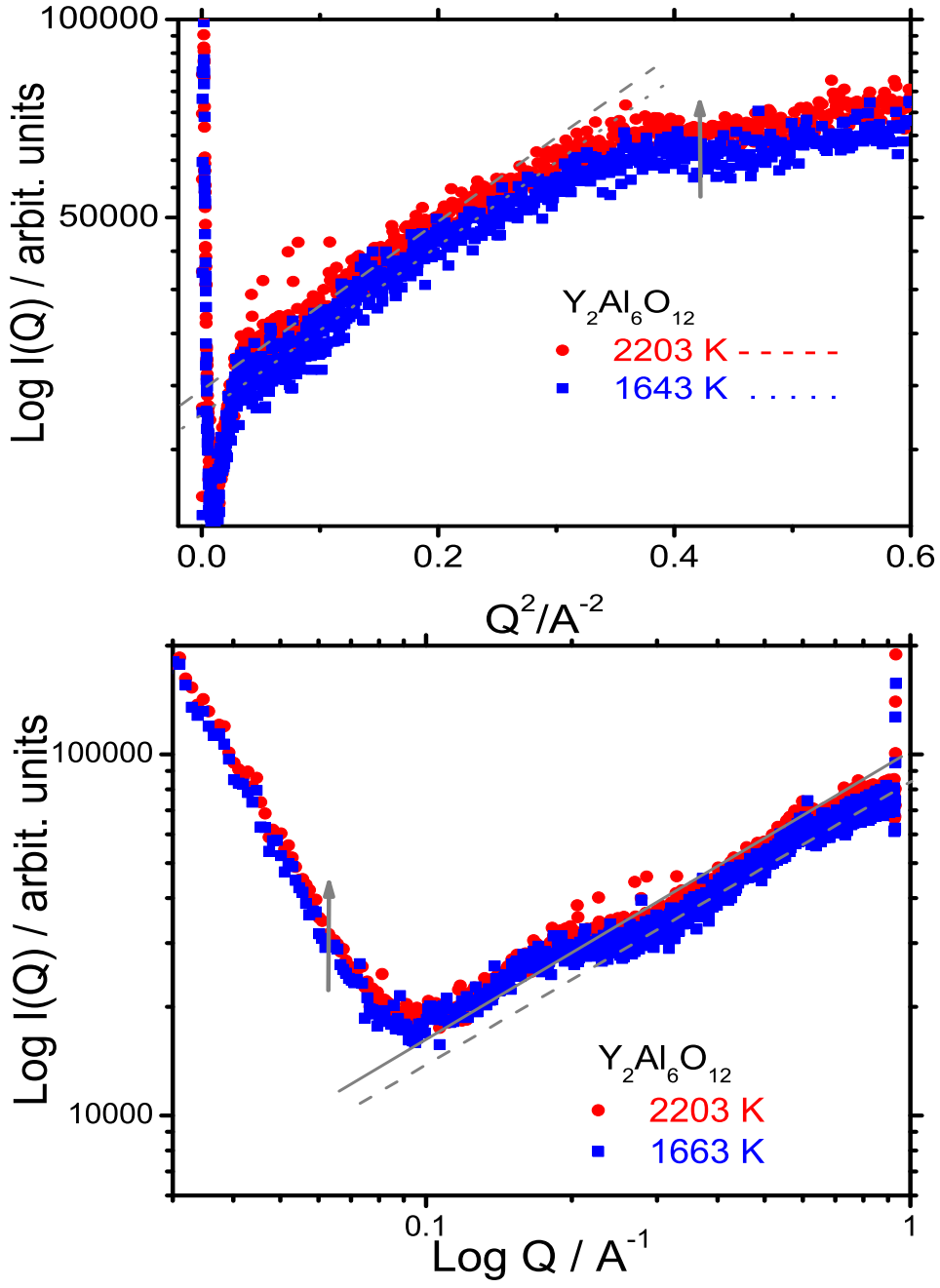

Figure 5.3: Density fluctuations and their temperature dependence of molten and supercooled liquids $Y_2Al_6O_{12}$ [16]. LogI(Q) is plotted *vs* Q^2 in (a) where the linear region applies between $0.17 < Q < $ Å^{-1}; (b) is shown the plot of log$I(Q)$ *vs* log$Q$

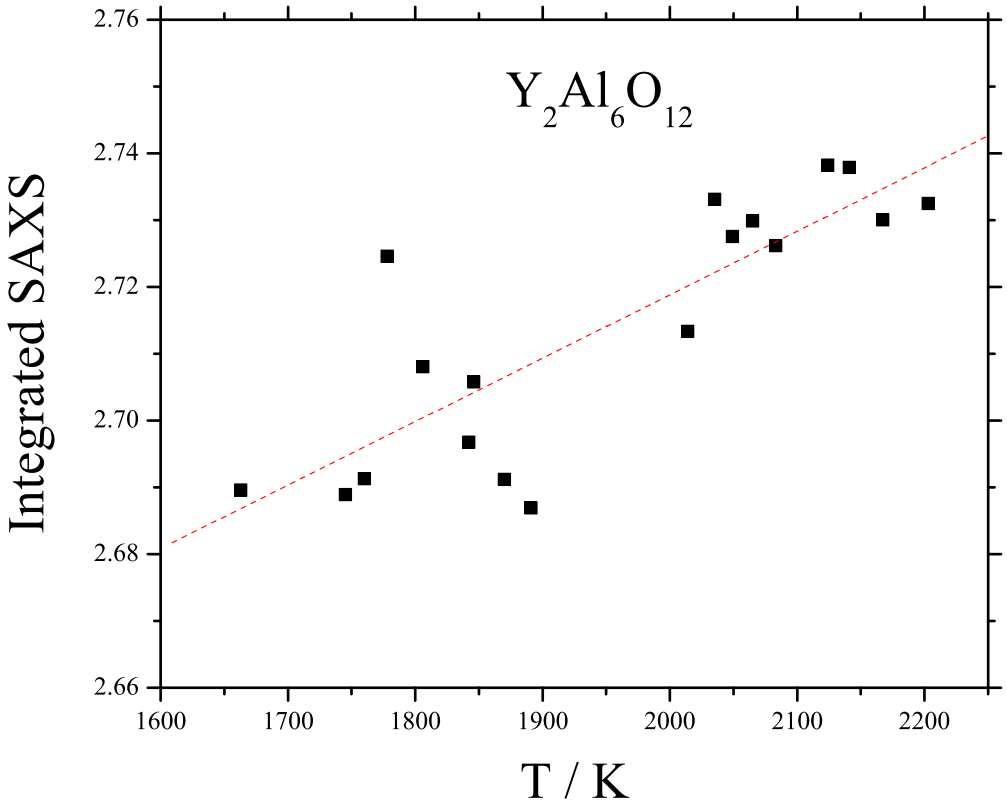

Figure 5.4: Intergrating of SAXS intensity $Y_2Al_6O_{12}$, indicates a linear raise with temperature due to the thermal fluctuation in density

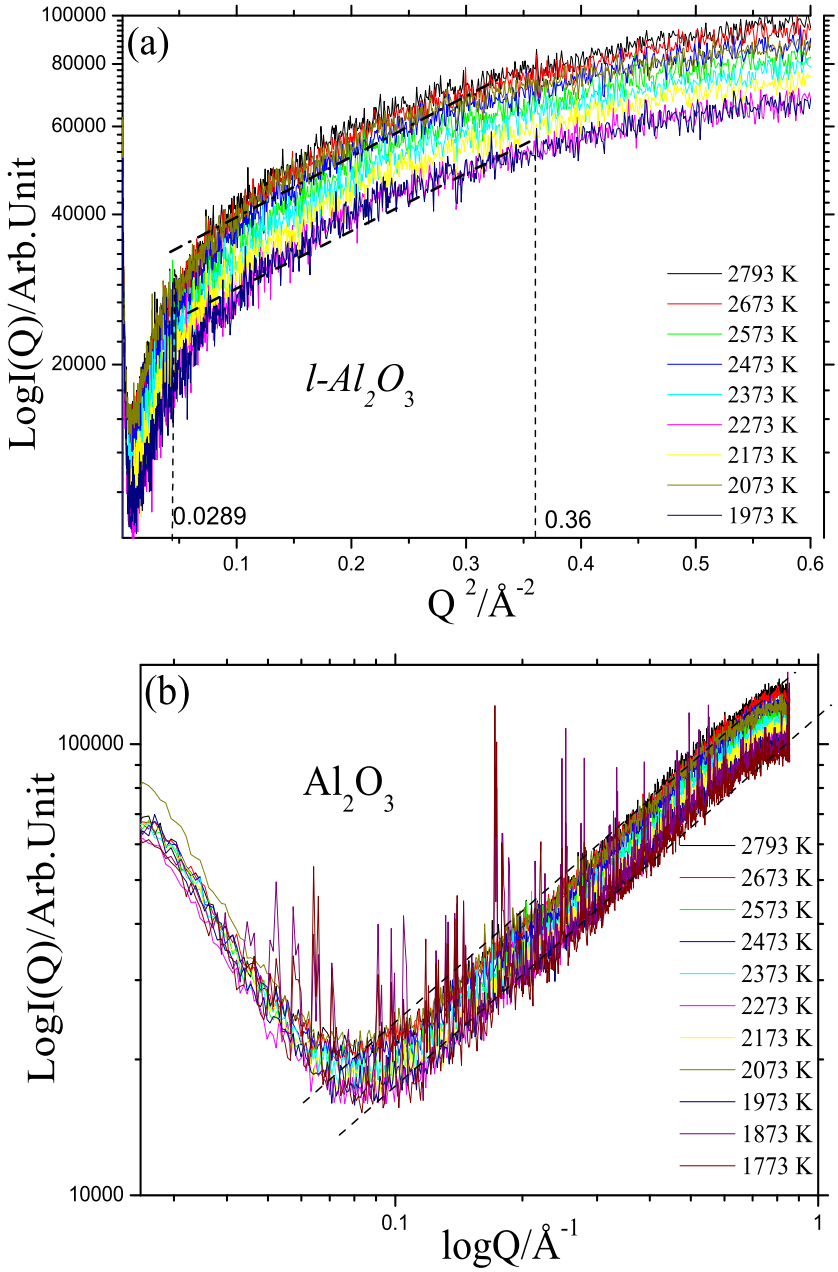

Figure 5.5: SAXS measurements for molten and supercooled liquids alumina plotted as log$I(Q)$ *vs* Q^2. Minimum between interatomic structure factor, $S(Q)$, and the raise in scatter from density fluctuations occurs at Q=0.078 Å

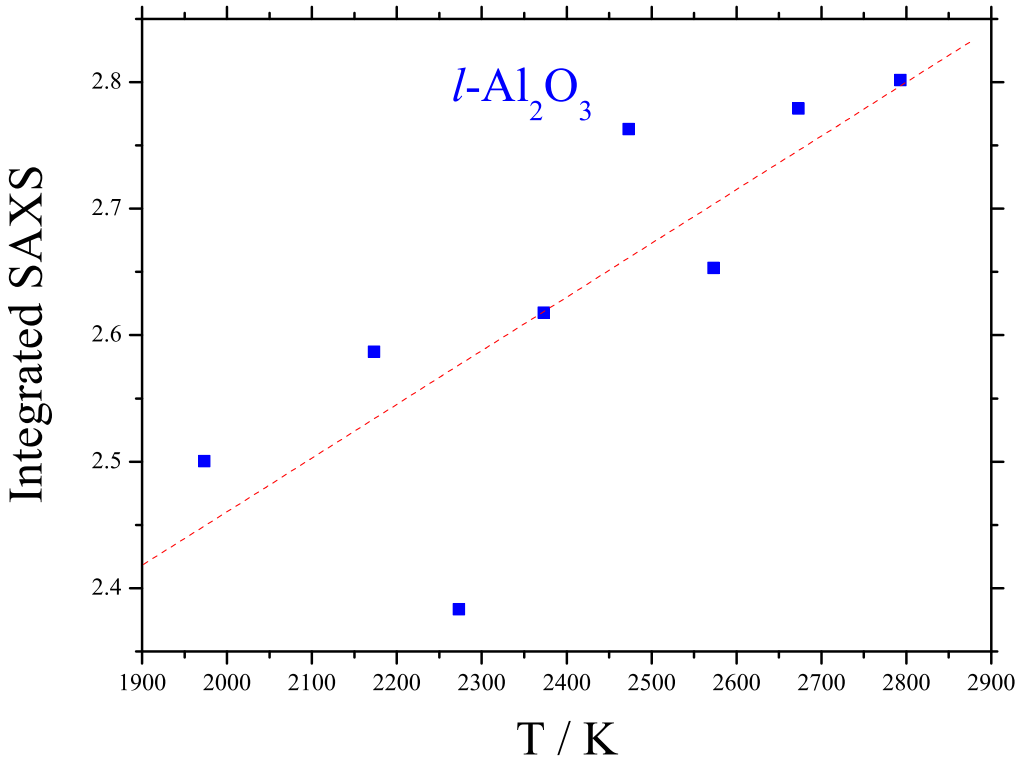

Figure 5.6: The integration has been calculated as $\int_{0.025}^{Q_{min}=0.078\,\mathring{A}} I_{SAXS} Q^2 dQ$ within Q range, 0.025 Å-0.078 Åbefore the contribution of structure factor $S(Q)$. The increase is linear with temperature indicating the inhomogeneities in density of molten and supercooled liquid alumina.

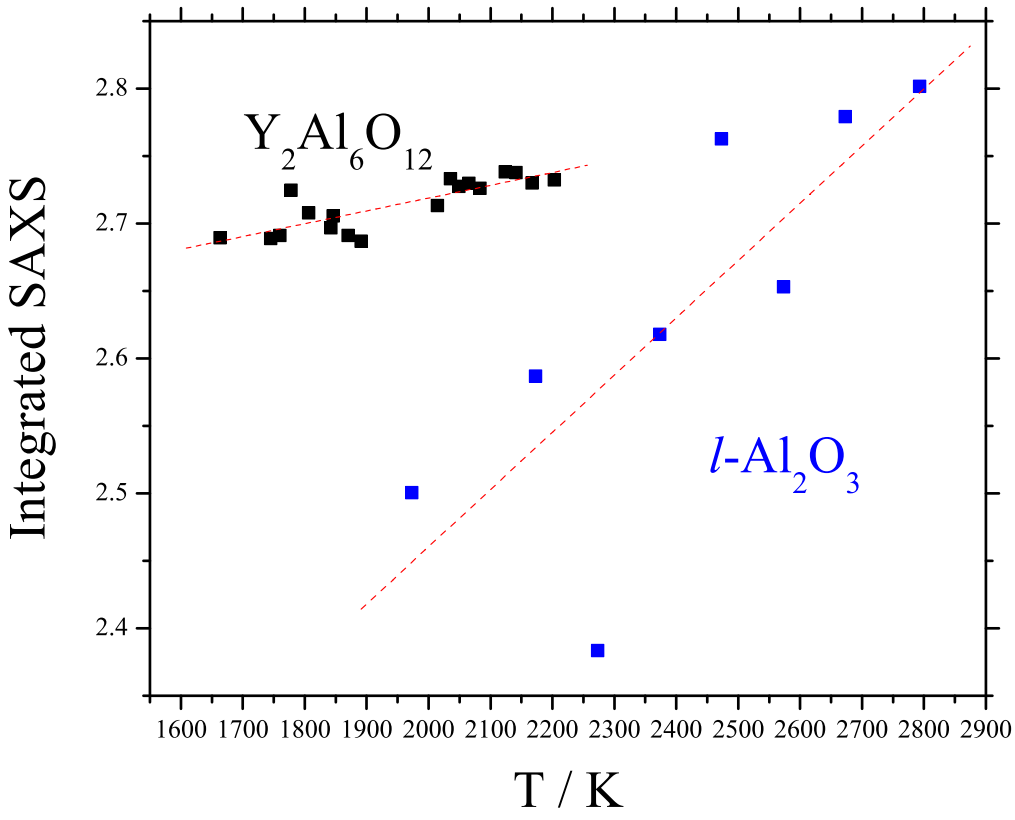

Figure 5.7: Comparition of $\int I_{SAXS} Q^2 dQ$ versus T for liquid alumina and liquid yttrium aluminates

Chapter 6

Calorimetry for Levitated Liquids Using Optical Pyrometry

6.1 Introduction

Phase transitions occur whenever the entropy and density of condensed matter change. This is usually considered in physical transformations at specific temperature T, pressure, P. Phase transitions are divided into first and second order. In a first order phase transition, latent heat, H, is involved, and the transition generally obeys the Clausius-Clapeyron equation:

$$\frac{dT}{dP} = \frac{\Delta V}{\Delta S} \tag{6.1}$$

Consider melting transition as an example of the first order transition where liquid (L) and crystalline (C) phases coexist. Equation 6.1 defines the melting curve, dT/dP, where $\Delta V = V_L - V_C$ and $\Delta S = S_L - S_C$ are the differences in molar volume and entropy respectively between the liquid and the crystal. Second phase order transitions do not have accompanying latent heats, but an abrupt change in compressibility K_T, heat capacity C_p, thermal expansion coefficient α etc. All these variations indicate phase transitions and can usually be detected by thermal analysis techniques. In case of levitated liquids under contactless conditions, an optical pyrometer is suitable for measuring the enthalpy change associated with phase transition. We have measured the heat of fusion during recrystallisation of alumina on cooling and enthalpy of liquid-liquid transition of $(Y_2O_3)_{0.2}(Al_2O_3)_{0.8}$

liquid.

6.2 Differential scanning calorimetry

Calorimetry methods measure changes in enthalpy, *H*. Differential Scanning Calorimetry (DSC) is a technique which is part of a group of techniques called Thermal Analysis (TA). Thermal Analysis is based upon the measurement of changes in enthalpy or specific heat of a sample with temperature. DSC measures the energy necessary to establish a nearly zero temperature difference between a substance and an inert reference material. The reference usually has its melting temperature higher than that of the sample. It can provide qualitative and quantitative information about physical and chemical changes. These changes might involve change in heat capacity or endothermic and exothermic processes whose heat is absorbed or released. There are two types of DSC: heat-flow

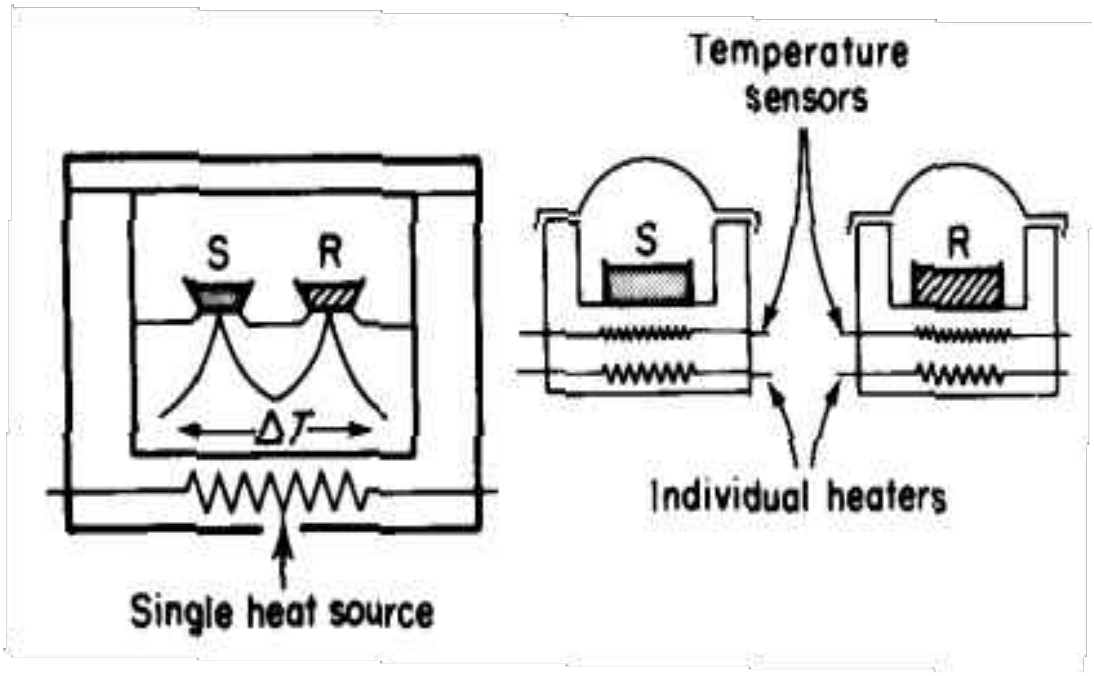

Figure 6.1: Two type of DSC systems: (a) heat-flow and (b) power-compensation

and power-compensation (figure 6.1). In power-compensation DSC, the temperature of the sample and reference are controlled independently in two separate, identical furnaces.

Their temperatures are maintained as equal and the energy needed to do that is a measure of enthalpy or heat capacity in the sample relative to the reference. In heat-flow DSC, the sample and reference are connected by one low-resistance heat-flow path. They are enclosed in a single furnace. Enthalpy or heat capacity changes in the sample will cause a difference in temperature relative to that of reference. The temperature difference is recorded and related to enthalpy change in the sample using calibration experiments. One advantage of DSC is that it only needs a small amount of sample. The sample can be encapsulated in an inert atmosphere that ensures uniform temperature and prevents oxidation.

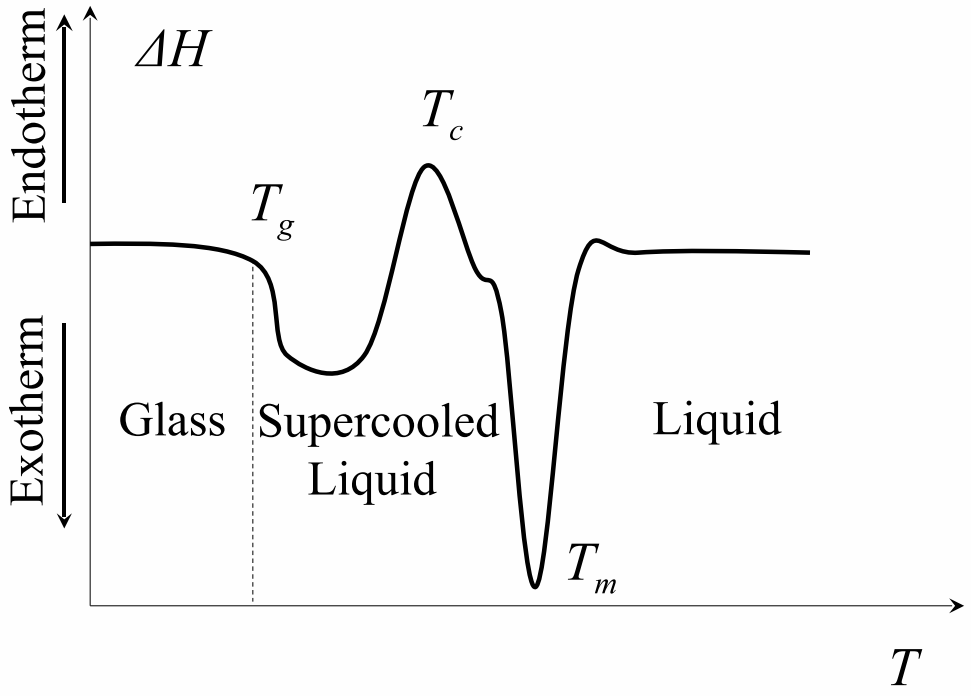

Figure 6.2: Schematic illustration of a DSC result on melting: the first transition at T_g, glass transition, then crystallisation at T_c and finally melting at T_m.

DSC measures the heat-flow $d(Q)/dt$ associated with phase transitions in materials as a function of time t and temperature T as the temperature is raised at constant rate

dT/dt. The sample and the reference have the same mass m. Heat capacity is given by:

$$C_p = E\frac{dQ/dt}{mdT/dt} \tag{6.2}$$

where E is the calibration factor. Enthalpy change of the sample between the starting temperature, T_{LL}, and the temperature, T can be calculated from the integration of the heat capacity, C_p:

$$H = \int_0^T CpdT \tag{6.3}$$

The change in enthalpy, H, associated with annealing glass, forming a ceramic and melting a crystal are illustrated schematically in figure 6.2. Accordingly, DSC can be used for measuring:

- Glass transition temperature, T_g in glasses and polymers
- Change heat capacity, ΔC_p and configurational entropy, S_{config}
- Melting temperature, T_m and heat of fusion during melting, H_{fusion}
- Crystallisation temperature above T_g and heat of fusion of crystallisation, H_{cryst} in glass ceramics.

If the sample was completely isolated from its surroundings, crystallisation would cause the temperature to rise sharply and then fall, a phenomenon called recalescence.

6.3 Recalescence

Recalescence is a sudden increase in temperature on cooling of a material through the supercooled range as illustrated in figure 6.4. It is caused by the liberation of the latent heat of recalescence due to total crystallisation. Using the levitator furnace and pyrometer, it is possible to measure the latent heat of recalescence *in situ* in the laboratory by following the free cooling of Al_2O_3 below T_m.

An optical pyrometer is used for high temperature measurement. The Luxtron Accufibre10 pyrometer operates at a wavelength, λ, of 950 nm. The focal length is 15.2 cm allowing the pyrometer to be placed far enough away from the very high temperature sample, avoiding any damage by the heat radiated from the sample. The pyrometer views a spot on the sample about 1 mm in diameter. The pyrometer head collects optical radiation emitted from the sample via an optical fibre. Data are taken every 100 ms. In order to obtain the true value of sample temperature, it is important to know the sample emissivity (a measure of how well a real body can radiate energy as compared with a blackbody) as a function of temperature at the pyrometer effective wavelength, λ.

Wien's law was used to obtain the temperature T of the sample via the apparent temperature read from the pyrometer, T_a using the following expression:

$$\frac{1}{T} - \frac{1}{T_a} = \frac{\lambda}{C_2} ln\epsilon \tag{6.4}$$

where $C_2 = 1.438810^7 nmK$ is Plank's second constant; ϵ is the emissivity of alumina. Emissivity ϵ which has been used in calibrating the temperature T equals 0.92 [57] [68]. Figure 6.3 shows the corrected temperature of alumina spheres of three different sizes in the free cooling process. Each sample was measured ten times and the average temperatures are shown. The recalescence peak can be seen to be smaller and occurring earlier in the smaller sphere.

Figure 6.4 shows the calibrated temperature quenching scans of alumina spheres of 2 mm in diameter in the inset with the average shown in the main part of the figure. At point 1, the laser was switched off from 32 W where the sample has already reached a steady-state temperature 2400 K just above the melting temperature T_m=2323 K. The liquid samples were spherical and did not show any obvious vibration. In the absence of input energy, the sample cooled mainly radiatively. Without nucleation at T_m, which

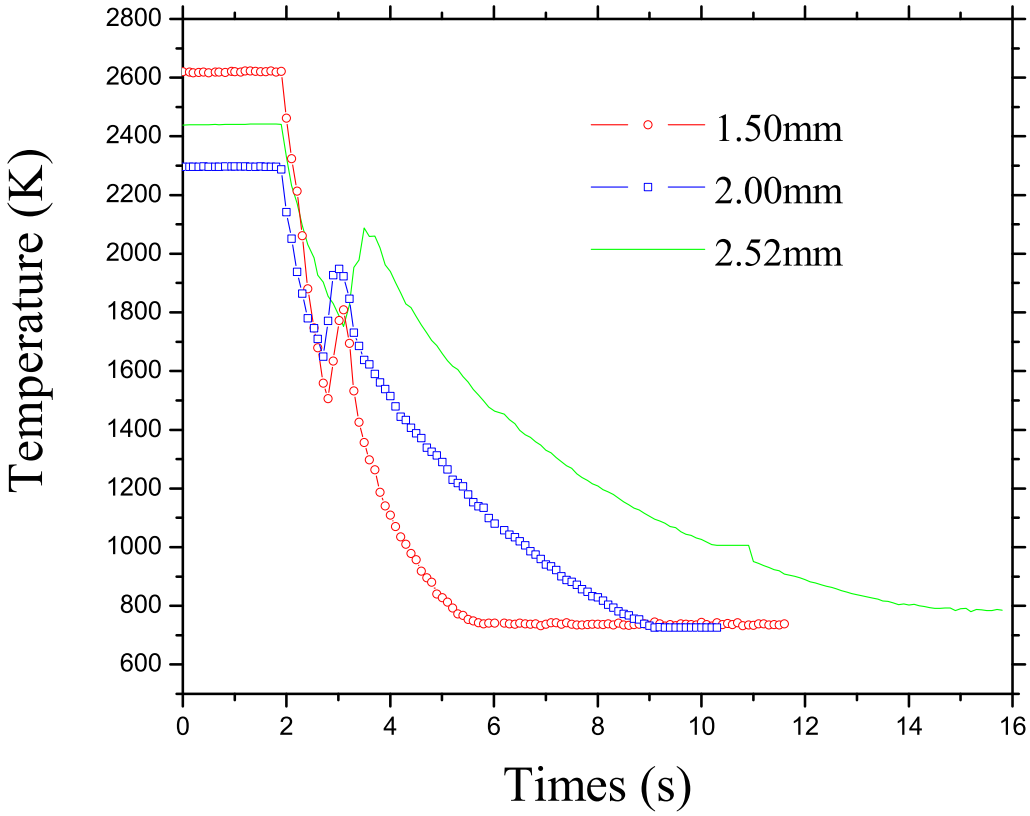

Figure 6.3: Temperature measurement during free cooling through supercooled range for different sizes of alumina spheres. The recalescence peaks indicate where recrystallisation takes place.

would otherwise occur heterogeneously due to the contact with the container, the levitated sample remained liquid and continued to cool below T_m until point 2 where the homogeneous crystallisation started at an average recalescence temperature , T_{recal}, at 1710 K. Thus the samples were in the supercooled state for 500 degrees below T_m. Solidification progresses rapidly and the sample temperature rises up to T_3=2131 K due to the release of the latent heat of recalescence, H_{recal}. At this stage, the sample vibrated strongly due to the liquid-solid phase transition. Afterwards, the temperature of sample in the solid state fell again to room temperature. Point 4 is the limit of accurate temperature measurement

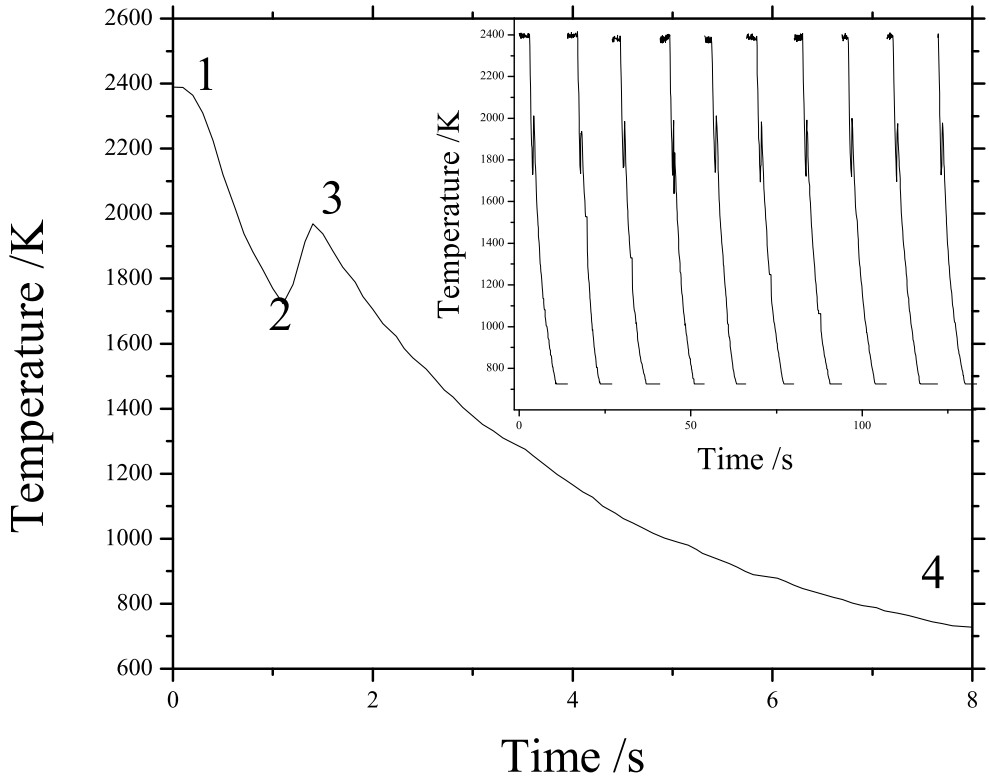

Figure 6.4: Temperature measurement during free cooling. The temperature is the average of 10 measurements shown in the inset

of the optical pyrometer (around T_4=1000 K).

The optical pyrometer and the levitator furnace have been used as a calorimeter in order to obtain the latent heat of recalescence, H_{recal}, and to compare this with the latent heat of fusion, H_{fusion} which is 111.4 $kJmol^{-1}$. The heat released from the sample can be calculated by integrating the power as a function of temperature with respect to time, provided all losses are accounted for. The radiative power, P_{rad} is obtained from Stefan's law: $P = \epsilon\alpha ST^4$ where $\alpha = 5.67.10^{-8} Js^{-1}m^{-2}K^{-4}$ is the Stefan-Boltzmann constant [58]; S is the surface area of alumina sphere and ϵ is the sample emissivity. The value of radiative power was calculated for each section of the cooling cycle with the corresponding value of sample area S and emissivity ϵ. S was estimated from the sample mass m=16.6mg

which had a diameter of $2mm$ given the sample densities in the liquid and solid states.

With the small focusing beam of laser on the sample ($\approx 1mm^2$), all incident laser power can be absorbed by the sample. Therefore, the incident laser power, P_{laser} is equal to the sum of radiative power measured by Stefan's law, $P_{rad} = \epsilon\alpha ST^4$ and the power loss, P_{loss}, by conduction and convection between the sample, the cold gas jet and water-cooled nozzle:

$$P_{laser} = P_{rad} + P_{loss} \tag{6.5}$$

The released heat without recalescence on free cooling between point 1 and 4 can be expressed by:

$$\int_{T_1}^{T_4} mC_p dT \approx m\bar{C}_p \int_{T_1}^{T_4} dT = m\bar{C}_p(T_1 - T_4) \tag{6.6}$$

where $\bar{C}_p = 1280 Jkg^{-1}K^{-1}$ is the average constant pressure heat capacity of alumina between 2400 K and 1000 K. However, when recalescence occurs during free cooling, the heat released also includes the heat of recalescence H_{recal}, i.e.

$$m\bar{C}_p(T_4 - T_1) + mH_{recal} = \int_{t_1}^{t_4} (\epsilon\alpha ST^4 + P_{loss})dt \tag{6.7}$$

where t_1 and t_4 are the time values at point 1 and 4 respectively. Hence

$$H_{recal} = \frac{1}{m}\int_{t_1}^{t_4} (\epsilon\alpha ST^4 + P_{loss})dt - \bar{C}_p(T_1 - T_4) \tag{6.8}$$

The first term in the right-hand side of the equation 6.8 is the total radiative energy during the free cooling process of the sample corrected for thermal loss. The second term is the released energy without recalescence within a temperature interval $\Delta T = T_1 - T_4$.

We have used the data from the temperature measurement of $(Y_2O_3)_{0.2}(Al_2O_3)_{0.8}$ (or *AY20*) at different temperatures made separately [59] in order to estimate the power loss which is approximately independent of the sample material. The power loss is the difference of the incident laser power with the radiative power measured by the pyrometer. Figure 6.5 shows the power loss at different temperatures. The inset indicates the laser

power and the radiative power. As we use two aluminium mirrors, with the reflectivity of 0.99, for focusing the laser beam figure 4.4. The incident laser power absorbed by the sample is 0.98%, which is the square of aluminium reflectivity, of the laser power before the optics. It appears that the power loss levels out below 1780 K. The power loss is

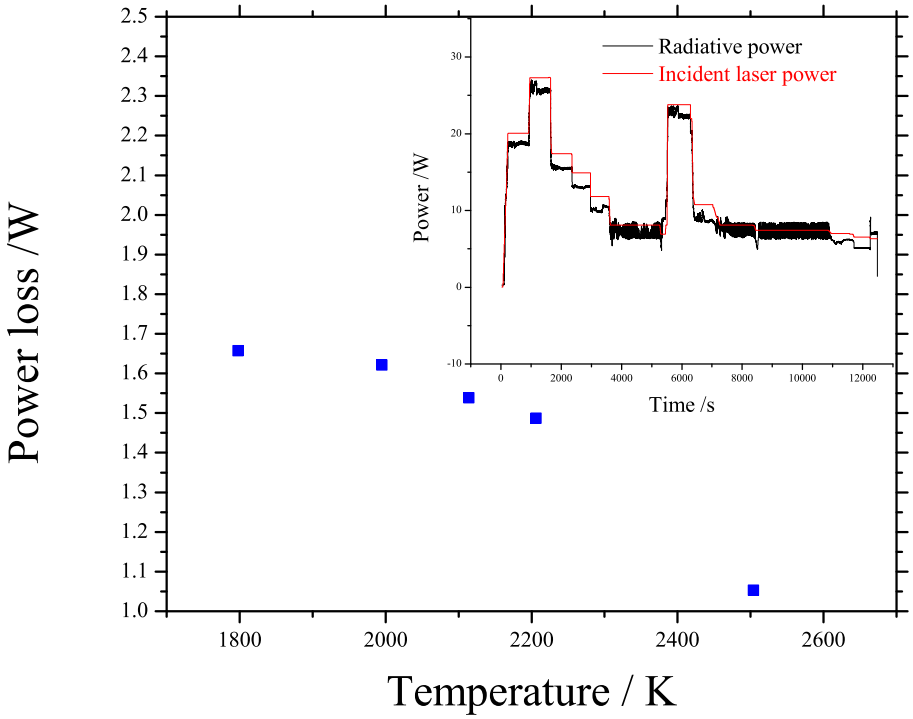

Figure 6.5: Estimation of power loss by conduction between the sample and the cold gas jet at different temperatures of 2.25 *mm* sphere *AY20*. Inner set shows the laser power in red which is greater than the radiative power.

greater at lower temperatures compared to higher ones. This can be attributed to the separation between the sample and the nozzle. It is large at the melting temperature and smaller at lower supercooled temperatures.

In order to use the equation 6.8, from figure 6.4, we have redrawn the power loss as a function of time instead of temperature. Figure 6.6 represents the resulting power loss and includes a feature at recalescence temperature, T_{recal} when the temperature rises and falls.

Video images indicated that the sample height remains approximately constant during recalescence, therefore we removed the feature at recalescence with an assumsumption that the power loss has a constant value during recalescence. Using this estimation we can calculate the latent heat of recalescence, H_{recal} of alumina sample during free cooling.

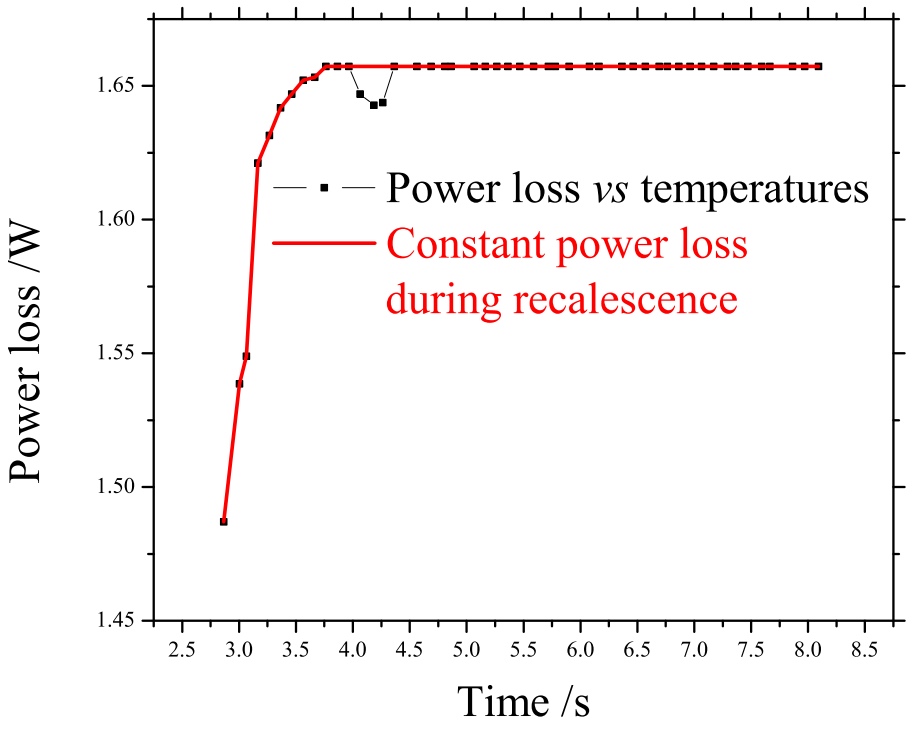

Figure 6.6: Power loss due to conduction and convection versus time. This is derived from figure 6.4 and 6.5. It assumes that temperature and time are directly correlated. The small feature at T_{recal} is removed as shown.

The radiative power measured by the optical pyrometer and the power that corrected thermal loss against time are shown in figure 6.7.

The heat released during recalescence is calculated from equation 6.8 and equals 16.4 J. The number of mols in 16.6 mg Al_2O_3 is $n = 16.610^{-3}/102 = 1.6110^{-4}\,mol$. The latent heat of recalescence for 2 mm alumina spheres is $16.4/1.61\ 10^{-4} = 101.8\,kJmol^{-1}$. Return-

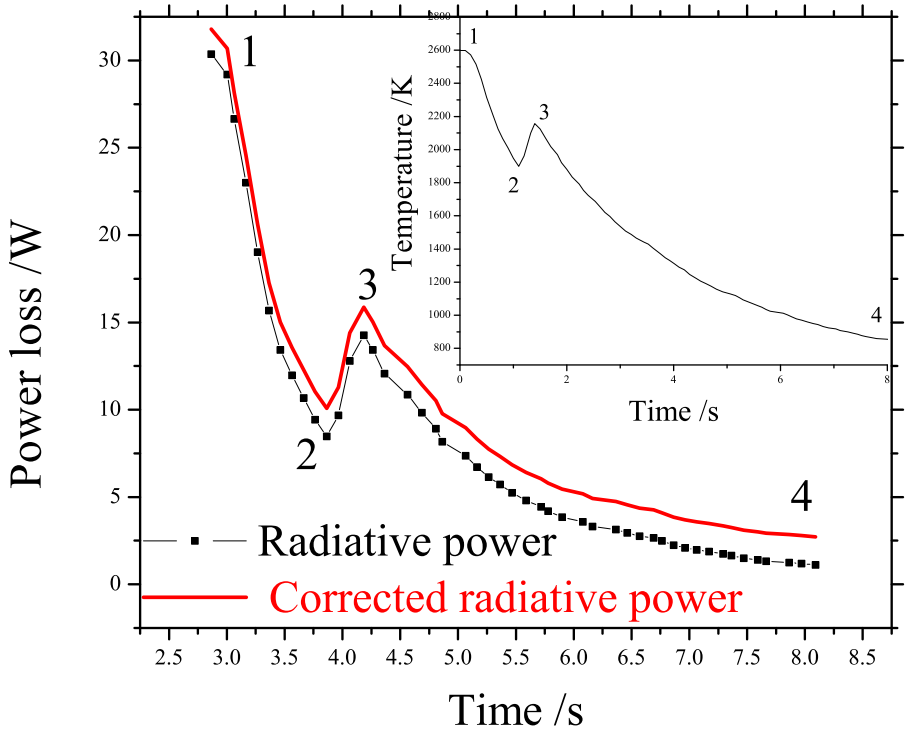

Figure 6.7: Radiative power from 2 mm alumina spheres during free cooling. The radiative power calculated from Stefan's law, $P = \epsilon\alpha ST^4$. The inset shows the temperature measured from optical pyrometer. Sample is in stable liquid between point 1 and point 2 where the free cooling starts. Recalescence occurs at point 2 and the temperature reaches the maximum at point 3. Point 4 indicates the sample in crystalline state. The solid red line shows the radiative power corrected for thermal loss obtained from figure 6.6.

ing to the equation 6.8 , the error in the latent heat, $\Delta H_{recal}/$ is related to the temperature measurement, where $\Delta T/T \approx \pm 0.005$. The error in the first term in equation 6.8 is governed by T^4 and therefore $\approx \pm 0.02$. The error with power loss and reflector loss will also be ± 0.03. Finally the error in the background heat in the third term will be $\approx \pm 0.005$, giving a total error $\Delta H_{recal}/H_{recal} \approx \pm 0.055$. Our value of the latent heat of recalescence is therefore $102 \pm 6\, kJmol^{-1}$. The latent heat of recalescence in this calorimetric method is lower compared to the latent heat of fusion in the literature 111.4 $kJmol^{-1}$ [60]. This can be attributed to the reduction in configurational entropy between T_m and

T_{recal} expected in the supercooled range as shown schematically in figure 2.1.

6.4 Endotherm - exotherm in liquid $Y_2Al_8O_{15}$

Using the optical pyrometer as a calorimetry tool, we have also studied the endotherm and exotherm in $Y_2Al_8O_{15}$ (AY20), which could be explained by the existence of liquid-liquid transition between high density (HDL) and low density liquid (LDL) [59]. In our experiment with (AY20), the laser power is fixed which usually maintains a constant temperature. However, in the vicinity of 1788 K, where the liquid-liquid transition is observed, the pyrometer reading oscillates (figure 6.8). These regular fluctuations are interpreted as repetitive exotherm-endotherm pairs. There is an amount of heat emitted by the sample (exotherm) for the HDL-LDL transition which is then reabsorbed (endotherm) when LDL-HDL transition occurs. This happens repeatedly over a given time. It results in the thermal cycling and dynamic oscillations in the sample. In our aerodynamic levitator furnace, the laser beam is directed on the top of the sample where the optical pyrometer is also focused. The thermal cycle of AY20 is a continuous displacement of the LDL phase from the bottom to the top. This then converts to HDL in the laser beam. When the temperature in the nozzle falls below the transition temperature T_{LL}, the LDL phase created can return to the top and switches back to the HDL phase.

Specifically, the temperature of the HDL phase in the bottom is reduced each time by contact with the cool gas flow and conduction to the water-cooled nozzle. From the video recording, the thermal cycles have a frequency of about $0.25Hz$. In ref [59], the equation of motion of a split sphere is $d^2\theta/dt^2 = Qsin\theta$, where θ is the angular displacement from vertical and $Q = A(\Delta\rho/\rho)g/a$. A is a constant approximately equal to the fraction of the sphere converted to LDL ($\approx 1/3$), $\Delta\rho/\rho$ is the density contrast between HDL and LDL and g is the acceleration due to gravity ($9.8\,ms^{-2}$).

The fluctuations in temperature of (AY20) shown in figure 6.8 include two distinguished processes, endotherm and exotherm, that can be modelled separately. The model is used to quantify the radiated power, from which the enthalpy change ΔH_{LL} and hence the entropy change $S_{LL} = \Delta H_{LL}/T_{LL}$, associated liquid-liquid transition can be obtained. Here we describe how we can use the calorimetric method described earlier (section 6.3).

In the exotherm, the sample releases energy associated with liquid-liquid transition.

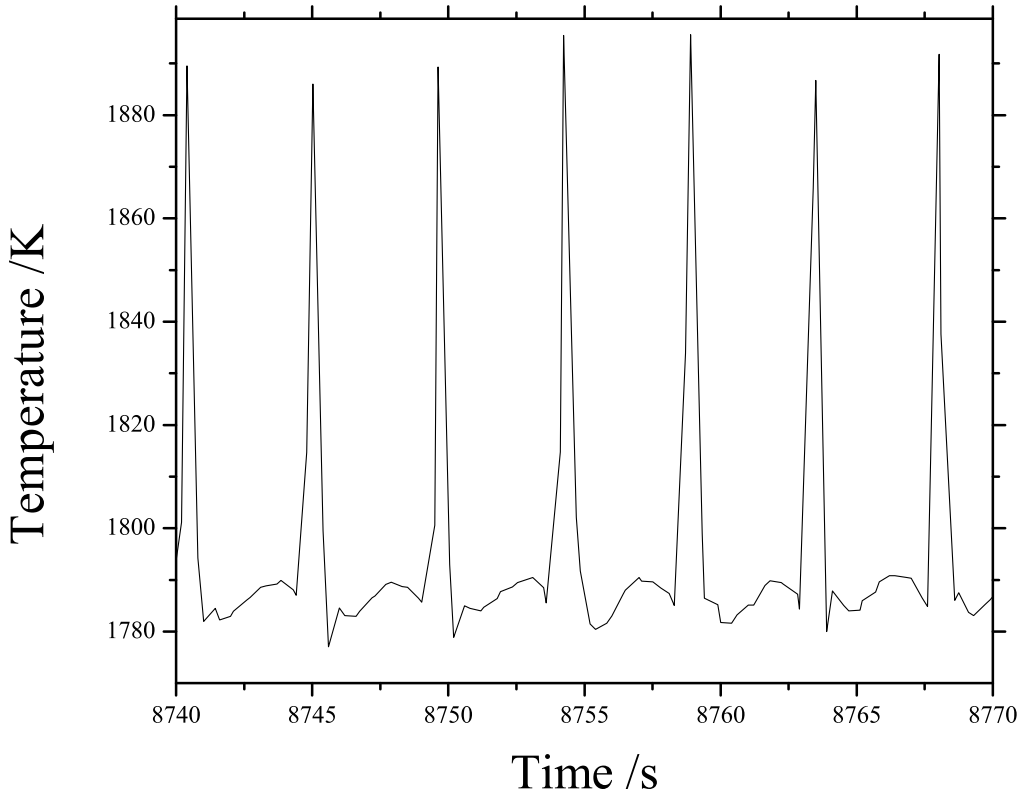

Figure 6.8: Fluctuation in temperature of AY20 measured when the transition HDL-LDL occurs around T_{LL}=1788 K.

Its temperature increases to T_1 around 1888 K and then decreases back to T_{LL}=1788 K.

The derivative of the heat transfer has the expression:

$$\frac{dQ}{dt} = \epsilon\alpha S T^4 - \epsilon\alpha S T_{LL}^4 \tag{6.9}$$

where $T_1 > T > T_{LL}$. Since

$$\frac{dQ}{dt} = \frac{dQ}{dT}\frac{dT}{dt} \tag{6.10}$$

and $dQ/dT = nC_p$, n is the number of mol of the sample and C_p is the specific heat for one mol of material, dT/dt can also be obtained. The equation 6.9 can be rewritten as:

$$nC_p\frac{dT}{dt} = \epsilon\alpha S(T^4 - T_{LL}^4) \tag{6.11}$$

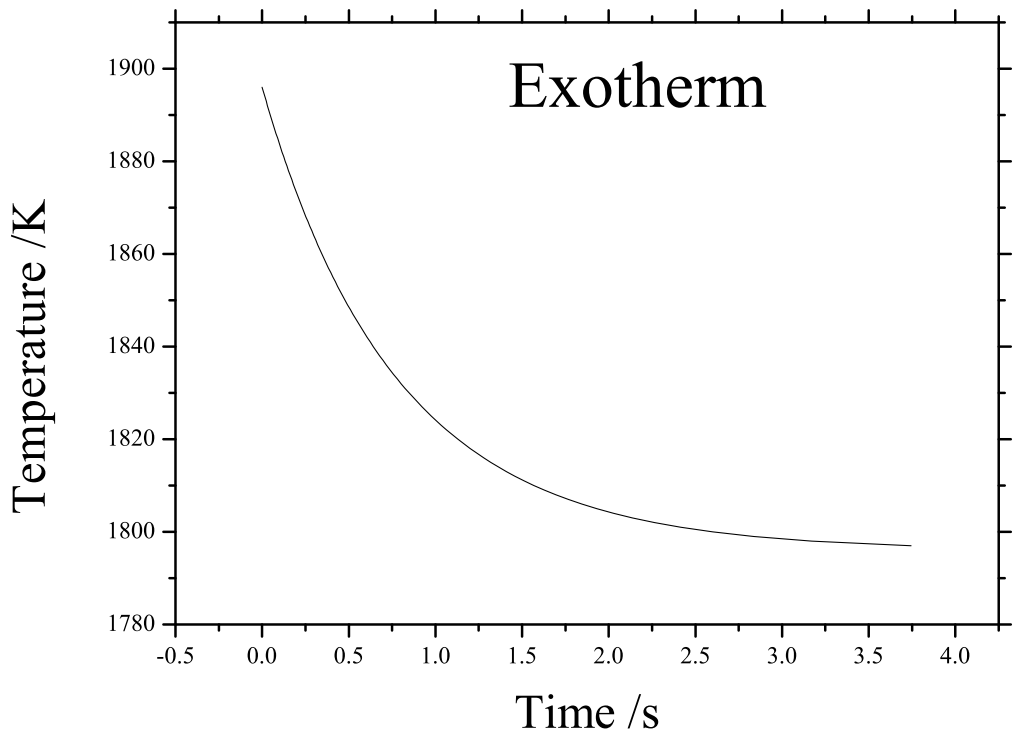

Figure 6.9: Exotherm curve plotted from equation 6.15

$$dt = \frac{nC_p}{\epsilon\alpha S}\frac{dT}{(T^4 - T_{LL}^4)} \tag{6.12}$$

$$\int_0^t dt = \frac{nC_p}{\epsilon\alpha S}\int_{T_1}^{T_{LL}} \frac{dT}{(T^4 - T_{LL}^4)} \tag{6.13}$$

The term $1/(T^4 - T_{LL}^4)$ can be written in small power terms such as:

$$\frac{1}{(T^4 - T_{LL}^4)} = \frac{1}{2T^2}\frac{1}{T^2 + T_{LL}^2} + \frac{1}{4T_{LL}^3}(\frac{1}{T + T_{LL}} + \frac{1}{T - T_{LL}}) \tag{6.14}$$

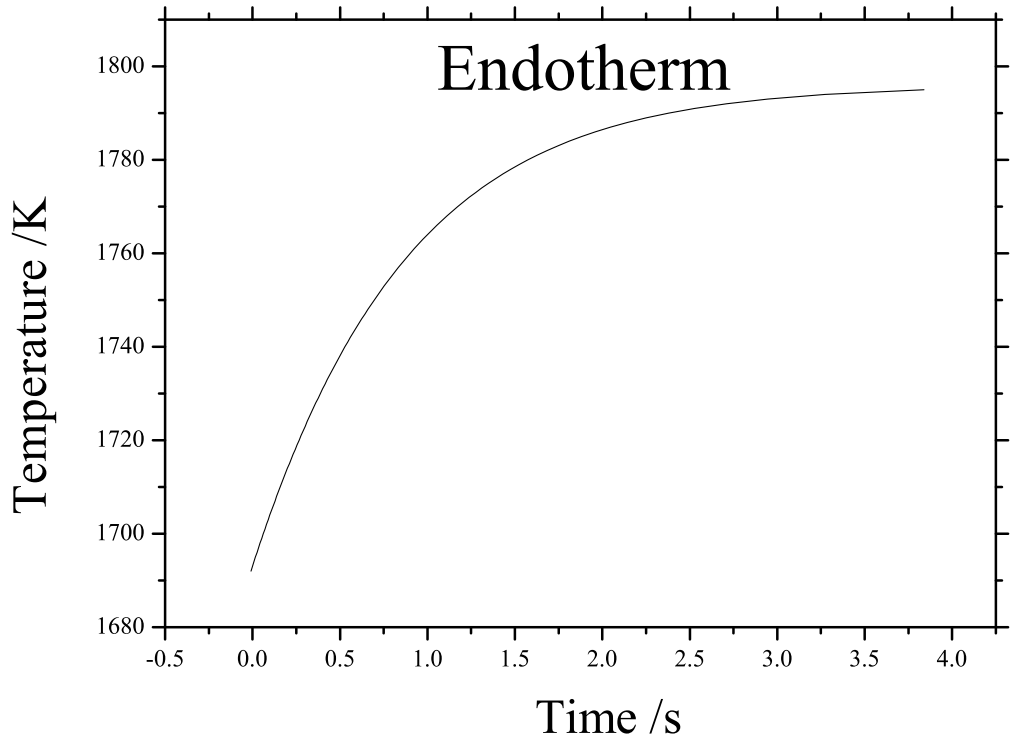

Figure 6.10: Endotherm curve plotted from equation 6.16

This equation represents the time dependence of temperature during the exotherm process, namely:

$$t = \frac{nC_p}{2\epsilon\alpha S T_{LL}^3}\left[arctan\frac{T}{T_{LL}} + \frac{1}{2}ln(T + T_{LL}) - \frac{1}{2}ln(T - T_{LL}) - 2.6\right] \tag{6.15}$$

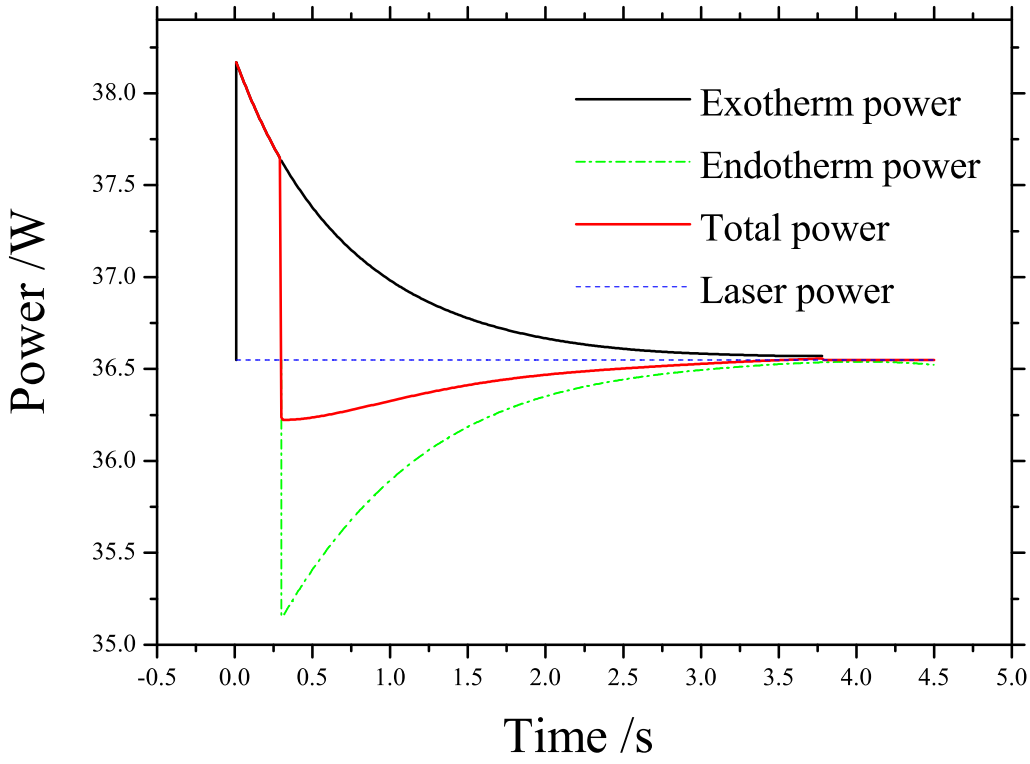

Figure 6.11: Modelled power of AY20 using Stephan's law, $P = \epsilon\alpha ST^4$. The endothermic process occurs $0.3s$ after the exothermic one. The sum of both endothermic and exothermic powers give the total power of the sample.

Figure 6.9 shows the modelled exotherm curve when the temperature decreases from $T_1 = 1888K$ to $T_{LL} = 1788K$ using equation 6.15. The temperature rises again from $T_2 = 1639K$ to $T_{LL} = 1788K$ during the endotherm process and a similar calculation as above applies, the endotherm curve has the function as shown in figure 6.10 using equation 6.16.

$$t = \frac{nC_p}{2\epsilon\alpha ST_{LL}^3}\left[arctan\frac{T}{T_{LL}} + \frac{1}{2}ln(T_{LL}+T) - \frac{1}{2}ln(T_{LL}-T) - 2.6\right] \quad (6.16)$$

At temperatures close to melting $C_p = 3R$, where R is the gas constant, i.e. $C_p = 24.96kJmol^{-1}$. The enthalpy associated with HDL-LDL transition can be modelled in fig-

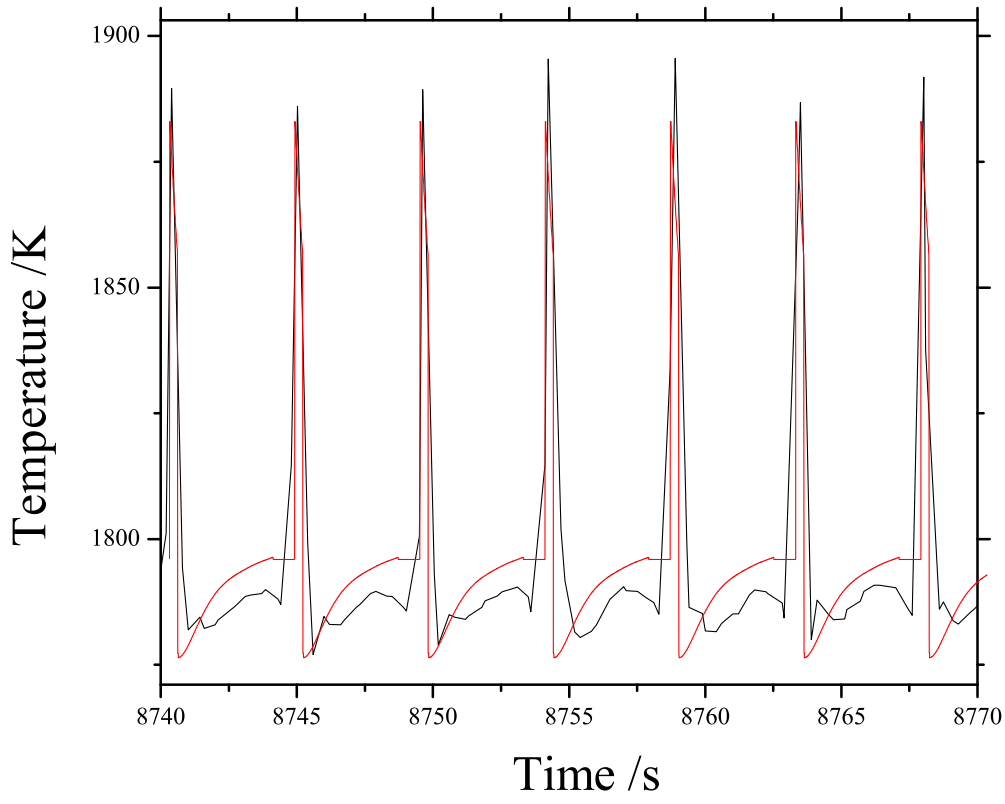

Figure 6.12: Model of fluctuating temperature of AY20 calculated inversely from Stephan's law and the total power.

ure 6.11, where the endotherm process occurs $0.3s$ after the exotherm. The temperature oscillations are shown in figure 6.12 and the modelled temperatures fit well with measurements using the optical pyrometer. The enthalpy for polyamorphic transition has a value of $\Delta H_{LL} = 34 \pm 8 kJmol^{-1}$ and therefore the entropy in the transition, $S_{LL} = \Delta H_{LL}/T_{LL}$. has a value of $19 \pm 4 Jmol^{-1}K^{-1}$.

6.5 Conclusion

DSC is used for heat of fusion measurements. However, it is not suitable in the supercooled regime due to the crystallisation that results from nucleation by contact between the

sample and the sample container. The optical pyrometer has been used to quantify the latent heat of recalescence in alumina on free cooling and also the liquid-liquid transition enthalpy and entropy in AY20.

Chapter 7

Debye-Waller Factor in Molten and Supercooled Liquid Alumina

7.1 Introduction

The Debye-Waller factor is the temperature factor that describes the decrease in scattering intensity (either from X-rays or neutron scattering) due to the thermal motion of the atoms, or due to static disorder. Debye-Waller factor increases with temperature. This is illustrated in figure 7.1 where the powder diffraction patterns (section 3.4) from α-Al_2O_3 are shown between room temperature and the melting point [17]. The sharp Bragg peaks at low temperature reduces in intensity as the temperature rises, in the following equation:

$$I_{hkl} \propto \exp -\frac{<\mu^2> Q^2}{3} \tag{7.1}$$

where $<\mu^2>$ is the temperature-dependent, average mean-square displacement and Q is the momentum transfer of incoming radiation.

In the molten state, the diffraction is replaced by diffuse scattering (section 3.5) where the interatomic oscillations become more damped with temperature. In this case, the Debye-Waller factor is $<\mu_{ij}^2>$, the correlated average mean square displacement of atoms i and j.

The relative Debye-Waller factor of molten and supercooled liquid alumina has been obtained from structure factor measurements over a large temperature range, 1723-2423

K, using the aerodynamic levitator and *in situ* X-ray diffraction. The value of $< \mu_{ij}^2 >$ in liquid alumina is correlated with the average $< \mu^2 >$ from the Debye model (section 2.4) which is important in interpreting the physical properties of crystals and liquids. In chemically complex materials, the relative Debye-Waller factors are usually measured by extended X-ray absorption fine structure (EXAFS) which records the difuse scattering around a particular type of atom. In EXAFS analysis, where the plane wave approximation is similar to the Debye equation, a ratioing technique has been used in the past to obtain $< \mu_{ij}^2 >$ with respect to a particular element [61, 62]. In this chapter, the same approach is used, applying the structure factors of supercooled liquid alumina at different temperatures.

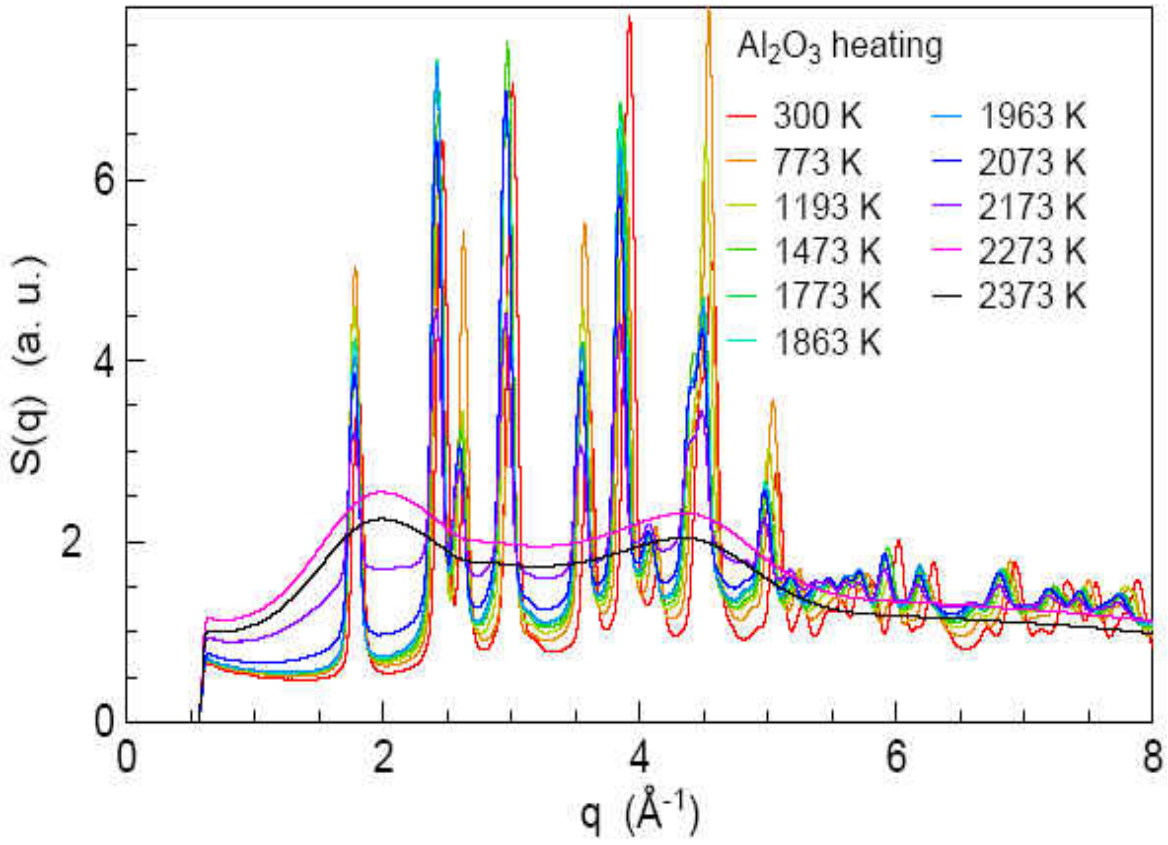

Figure 7.1: Structure factors for α-Al_2O_3 measured on heating through the melting point [17]

7.2 Method

The Debye expression for diffuse scattering from an element liquid/glass is:

$$Q(S(Q)-1)=\sum_i\sum_j N_{ij}f_i(Q)f_j(Q)\frac{sinQr_{ij}}{r_{ij}}\exp(-\frac{Q^2\mu_{ij}^2}{2}) \tag{7.2}$$

where *S(Q)* is the structure factor (section 3.5), N_{ij} is the coordination number of j^{th} shell around the i^{th} atom, r_{ij} is the interatomic distance and u_{ij}^2 is the variance in r_{ij}, and is the correlated Debye-Waller factor [63].

For an AB alloy, scattering from the nearest neighbours is given by:

$$Q(S(Q)-1)=N_{AB}\frac{f_AQf_BQ}{4}\frac{sinQr_{AB}}{r_{AB}}\exp-(\frac{Q^2\mu_{AB}^2}{2}) \tag{7.3}$$

For the case of liquid Al_2O_3 where scattering is also mainly from the nearest neighbours:

$$Q(S(Q)-1)=N_{Al-O}0.4f_{Al}0.6f_O\frac{sinQr_{Al-O}}{r_{Al-O}}\exp-(\frac{Q^2\mu_{Al-O}^2}{2}) \tag{7.4}$$

If we ratio the structure factor at one temperature as reference, $S(Q)_{ref}$ with the structure factor at different temperatures T, $S(Q)_T$, we obtain:

$$\frac{S(Q)_T-1}{S(Q)_{ref}-1}=\frac{N_{Al-O}(T)}{N_{Al-O}(ref)}\frac{r_{Al-O}(ref)}{r_{Al-O}(T)}\exp-\left\{\frac{Q^2}{2}\left[\mu_{Al-O}^2(T)-\mu_{Al-O}^2(ref)\right]\right\} \tag{7.5}$$

If there is only one local configuration or the mix of configurations does not change appreciably, i.e. r_{Al-O} is approximately constant, and:

$$ln\frac{S(Q)_T-1}{S(Q)_{ref}-1}=ln\left\{\frac{N_{Al-O}(T)}{N_{Al-O}(ref)}\right\}-\left\{\frac{Q^2}{2}\left[\mu_{Al-O}^2(T)-\mu_{Al-O}^2(ref)\right]\right\} \tag{7.6}$$

Accordingly, $ln\frac{S(Q)_T-1}{S(Q)_{ref}-1}$ versus Q^2 should give a straight line with a slope equal to $\frac{\left[\mu_{Al-O}^2(T)-\mu_{Al-O}^2(ref)\right]}{2}$ and an intercept of $ln\left\{\frac{N_{Al-O}(T)}{N_{Al-O}(ref)}\right\}$. This will give the relative change in the correlated Debye-Waller factor with temperature that we expect to see. If the

average values of N_{Al-O} and r_{Al-O} do not change over the temperature range we are looking at, the straight line will go through the origin, otherwise from the intercept we will be able to judge any changes in 4 to 5-fold coordination. This approach has been used before in EXAFS analysis, where the plane wave approximation is similar to the Debye equation[64, 61].

7.3 Results

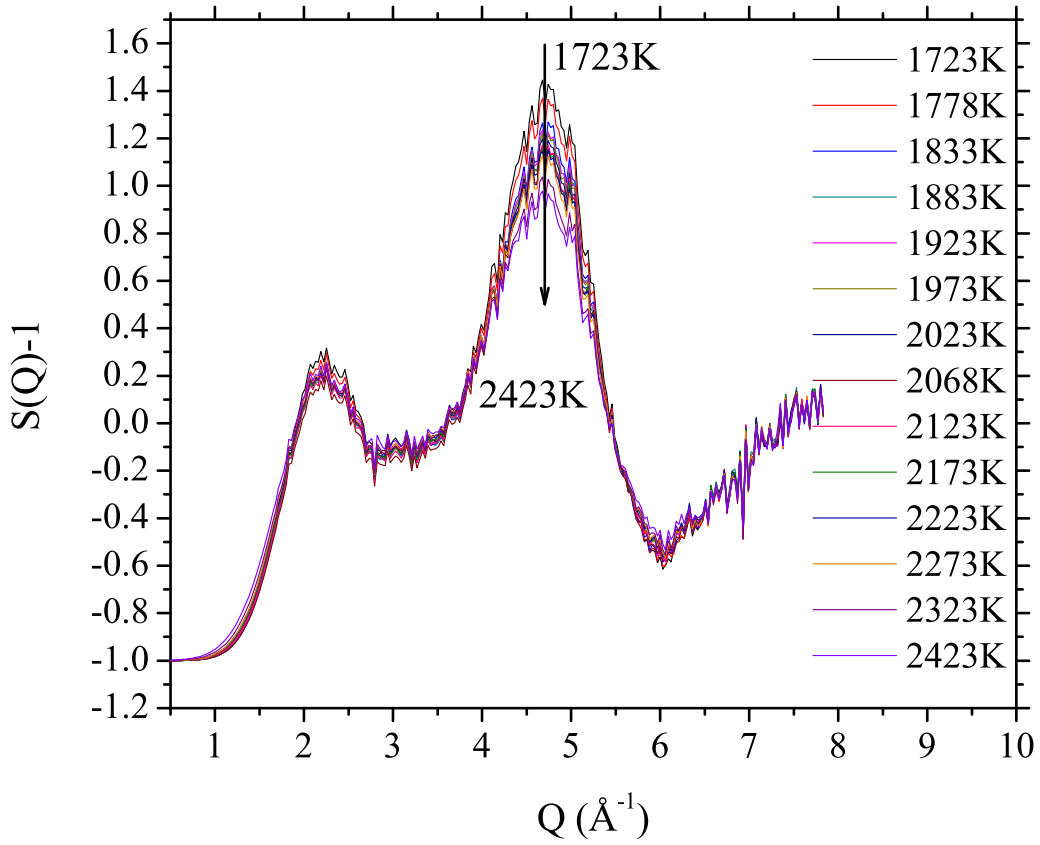

Figure 7.2: Structure factors of molten and supercooled liquid alumina over a wide range of temperature from above melting, 2423 K to recalescence T_R=1723 K., obtained from raw data as described in section 3.5

The structure factors at different temperatures of molten and supercooled liquid alu-

mina using wide angle X-ray techniques have been plotted in figure 7.2. The temperatures range from 2423 K in molten state through to recalescence temperature T_R=1723 K in supercooled liquid.

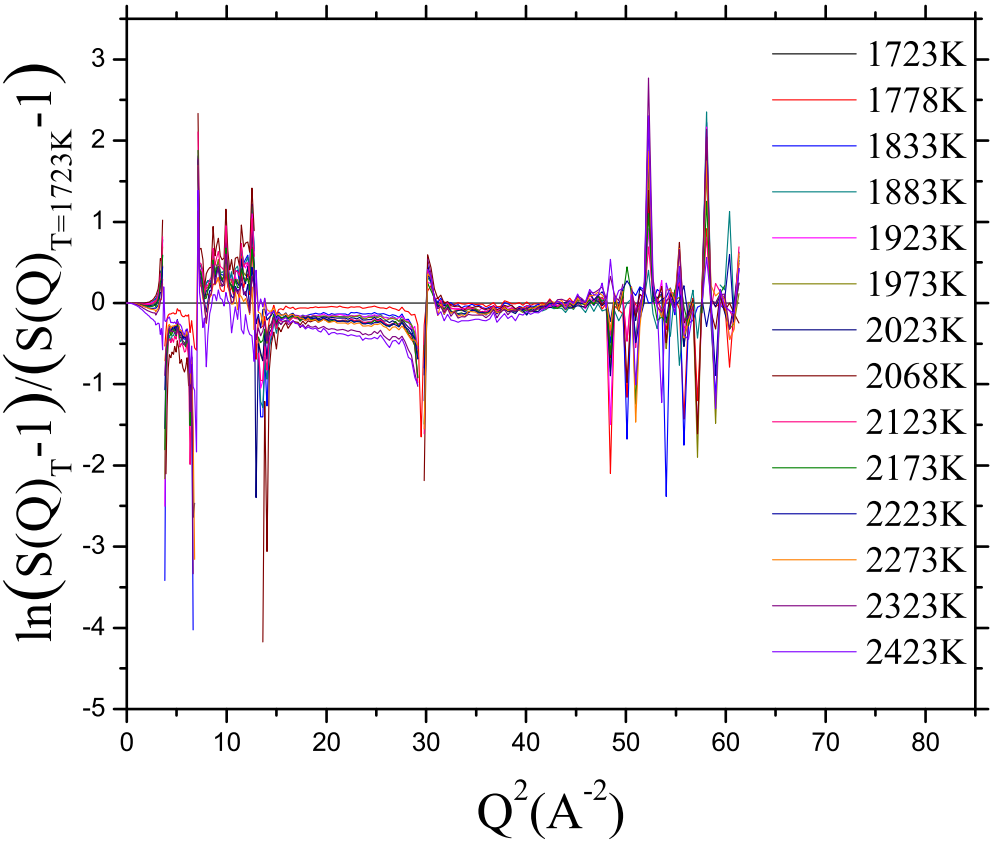

Figure 7.3: *In situ* X-ray diffraction *S(Q)'s* for molten and supercooled liquid alumina ratioed against *S(Q)* at 1723 K using equation 7.6.

Using equation 7.6, experimental *S(Q)'s* from figure 7.2 for molten and supercooled liquid alumina are plotted as $ln((S(Q,T)-1)/(S(Q,1723\,K-1)))$ versus Q^2 in figure 7.3. The plots do not show a clear series of slopes as we would expect to see. This is because the (*S(Q)*-1) profiles are not exactly in phase (they do not osscilate around 0 at the same Q value). This method therefore does not work for whole Q range because the

structure factor *S(Q)* is not the partial structure factor of Al-O but contains significant contributions from O-O and Al-Al correlations.

However, if we consider just the second peak of *S(Q)-1* (the peak around 4.9 Å^{-1}), we can still have an idea about the interaction of Al-O as this peak is mainly due to the contribution of Al-O. We take the value of *S(Q)-1* and the peak position value of Q (Q_{max}) which are obtained by using a Gaussian fit for each temperature. We then calculate $\Delta\mu^2_{Al-O} = \mu^2_{Al-O}(T) - \mu^2_{Al-O}(T_{ref})$ from those *S(Q)s-1* at Q_{max} using equation 7.6. We assume little change in local order between the molten and supercooled liquids over 700 degrees, i.e. $\mathrm{N}_{Al-O}(T_R) r_{Al-O}(T) \approx \mathrm{N}_{Al-O}(T) r_{Al-O}(T_{1723\,K})$ or $ln\left\{\frac{N_{Al-O}(T)}{N_{Al-O}(1723\,K)}\right\} = 0$. The table 7.1 shows the value of Q_{max}, *S(Q)-1*, together with the calculated $\Delta\mu^2_{Al-O}$ values at the second peak for each temperature. If μ^2_{Al-O} is Q-independent, these calculated $\Delta\mu^2_{Al-O}$ can be applied for the whole Q range of the experiment.

The statistical error in *S(Q)*-1 in figure 7.2 is 5% which dominates the uncertainty in $\Delta\mu^2_{Al-O}$. It also includes precise Q_{max} values which increase by 1 to 2% between 2423 K and 1723 K. Within the present approximation needed for equation 7.6, it is assumed that for all temperatures: Q_{max} =4.65±0.03. Taking literature values for atom form factor [71], this approximation would introduce a systematic error of less than 1%.

Figure 7.4 shows the temperature dependence of the relative correlated Debye-Waller factor, $\Delta\mu^2_{Al-O}$ obtained from Q_{max}, and *S(Q)-1* using equation 7.6 . From this result, if the value of the correlated Debye-Waller factor at one temperature $< \mu^2_{Al-O}(T) >$ is known, others can be calibrated. We use the Debye model to make this calibration at one temperature and then compare the dependence over the whole temperature range of the experiement with the model.

From the Debye model, the mean-square displacement or variance of the average atom

T	Q_{max}	*(S(Q)-1*	$\Delta\mu^2_{Al-O}$
1723 K	4.68	1.404	0
1778 K	4.68	1.336	0.00452
1833 K	4.68	1.234	0.01176
1883 K	4.65	1.193	0.01503
1923 K	4.68	1.203	0.01407
1973 K	4.48	1.186	0.01677
2023 K	4.65	1.161	0.01754
2068 K	4.65	1.161	0.01914
2123 K	4.65	1.161	0.01996
2173 K	4.65	1.12	0.02086
2223 K	4.65	1.117	0.02111
2273 K	4.65	1.091	0.02328
2323 K	4.65	0.997	0.0316
2423 K	4.62	0.943	0.03723

Table 7.1: Momentum transfer values, Q_{max}, and *S(Q)-1* profiles at the peak position together with relative correlated Debye-Waller factors $\Delta\mu^2_{Al-O}$ obtained by using equation 7.6.

of mass $\bar{m}$, $<\mu^2>$, is given by:

$$<\mu^2>= 9T\hbar^2/k_B\bar{m}\Theta_D^2 \tag{7.7}$$

where k_B is Boltzmann constant, Θ_D is the Debye temperature that relates with density, ρ, and speed of sound, namely:

$$\Theta_D = \frac{h}{k_B}\left\{\frac{4\pi V}{9}\left(\frac{1}{v_l^3}+\frac{2}{v_t^3}\right)\right\}^{-1/3} \tag{7.8}$$

where V is the molar volume and v_l, v_t are longitudinal and transverse speeds of sound.

For crystalline α-Al_2O_3, $v_l = 12,050 ms^{-1}$ and $v_t = 6400 ms^{-1}$ at room temperature [65]. From the density (3.98 gcm^{-3}) and the molar volume $V = 25.5 cm^3$, the Debye temperatures Θ_D is 1044 K. Using equation 7.7 and the average atomic mass $\bar{m} = 102/5 = 20.4g$, the variance of the average atom, $<\mu^2>$, for α-Al_2O_3 falls from 0.046 Å^2 at the melting point T_m=2323 K to 0.035 Å^2 at the recalescence temperature T_R =1723 K where supercooled liquid alumina crystallises. Since the average interatomic distance for α-Al_2O_3 using the Debye model ($\bar{r} = (V/5N_A)^{1/3}$) is 2.04 $\mathring{A}$, $\sqrt{<\mu^2>}/\bar{r} \approx 10\%$ is in line

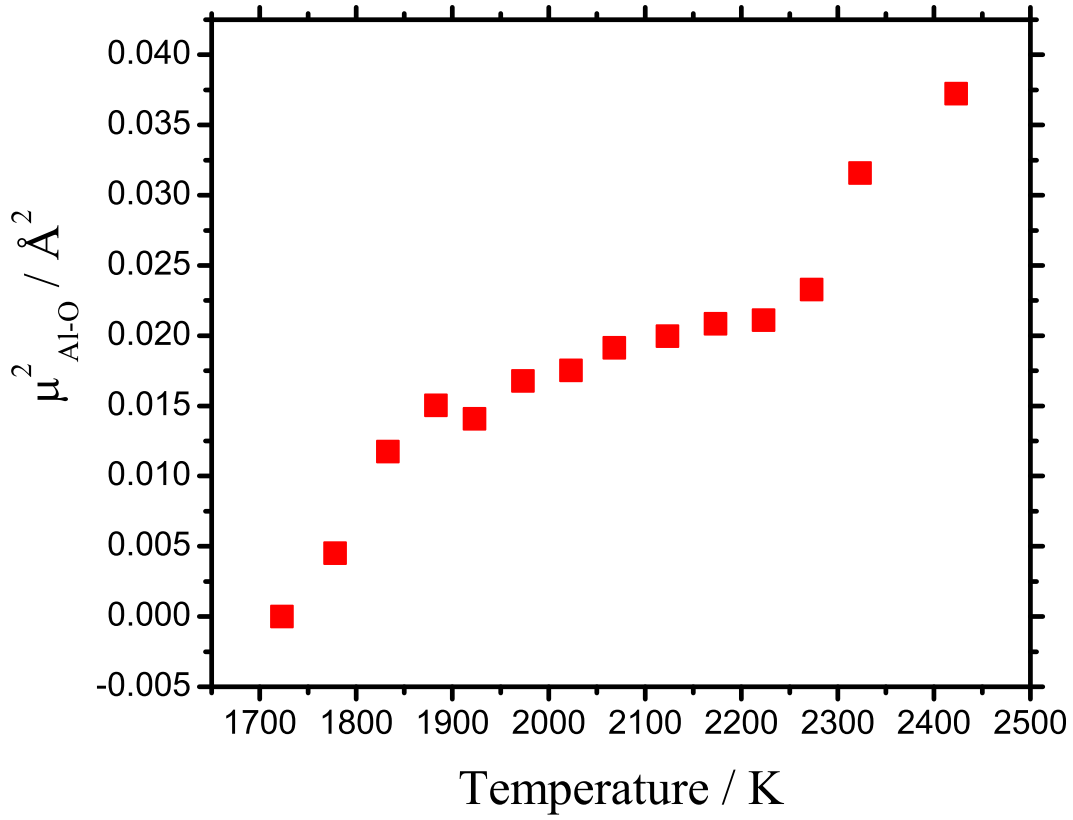

Figure 7.4: Relative correlated Debye-Waller factor , $\Delta\mu^2_{Al-O}(T)$ versus T from molten to supercooled liquid alumina temperature. The origin at the lowest temperature, 1723 K, is set to zero.

with Lindemann's law [20].

Turning now to liquid alumina, the measured longitudinal speed of sound at the melting temperature T_m[66], $v_l = 7352ms^{-1}$. Making an assumption for liquid alumina of v_l/v_t=1.9, which is similar to silica, the transverse speed of sound is $v_t = 3856ms^{-1}$. From the density of molten and supercooled liquid alumina (section 4.5.1), the Debye temperature Θ_D for liquid alumina is 565 K. The variance of the average atom, $< \mu^2 >$, decreases from 0.101 Å^2 at the melting temperature T_m to 0.088Å^2 at the crystallisation point T_R. The difference in Debye temperatures between crystalline and liquid alumina

reflects the change in local structure on melting from N_{Al-O}= 6 and N_{O-Al}= 4 to N_{Al-O}= 4.1 and N_{O-Al} = 2.8 on melting [67]. The variance of the average atom versus temperature for crystalline, molten and supercooled liquid alumina in Debye model is shown in figure 7.5.

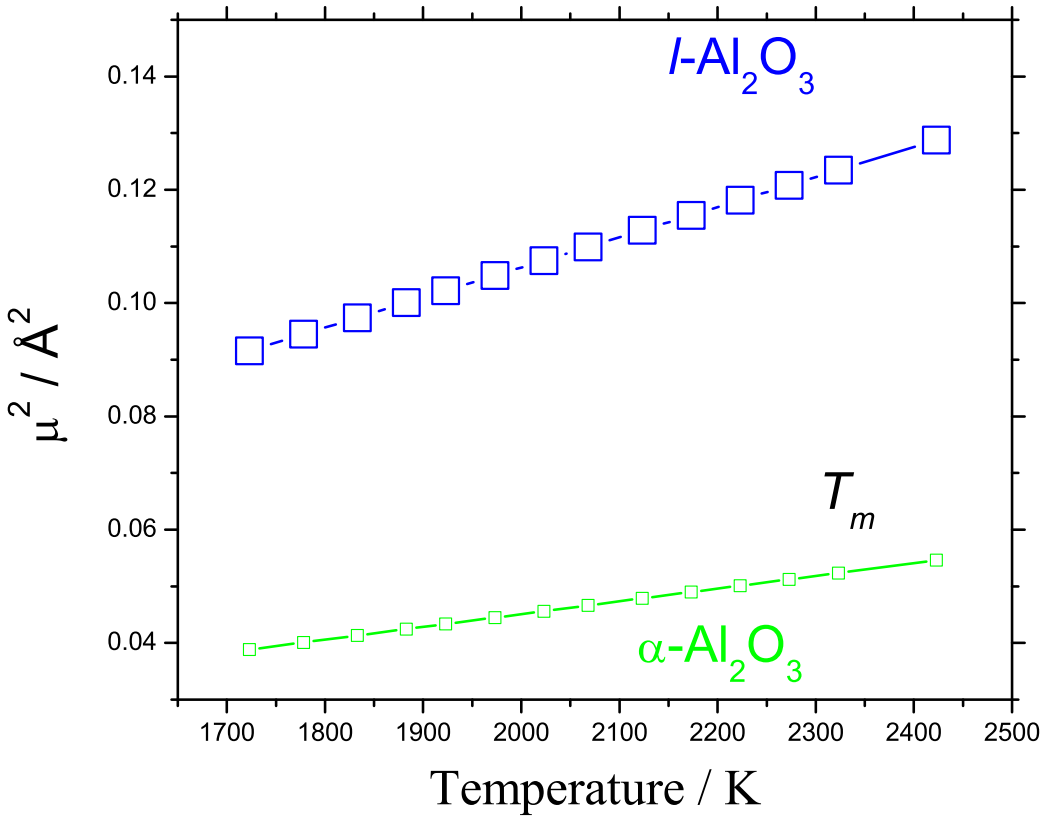

Figure 7.5: Variance of the average atom versus T for crystalline, molten and supercooled liquid alumina and in the Debye model

In ionic and covalent solids, thermal displacements are found to be approximately 40% correlated [62]. As a result, the correlated Debye-Waller factor,$< \mu_{ij}^2 >$, is less than the value of $2< \mu^2 >$, expected if the atom motion is completely random. Estimates give $< \mu_{ij}^2 >$=1.2$< \mu^2 >$ for maintaining neighbour distances [62]. Applying to crystalline, molten and supercooled state of alumina, the nearest neighbour correlated Debye-Waller

factor, $< \mu^2_{Al-O} >$, should be related to the average atom Debye-Waller factor, $< \mu^2 >$ by:

$$< \mu^2_{Al-O} >= 1.2 < \mu^2 > \tag{7.9}$$

Hence μ^2_{Al-O} at T_R should be given by $\mu^2_{Al-O} = 1.2 < \mu^2 >$ (liquid). Using the variance of the average atom from figure 7.5 and equation 7.9 to calibrate the correlated Debye-Waller factors given in figure 7.4 obtained from equation 7.6 and table 7.1. Thermal disorder in crystalline and molten, supercooled liquid alumina between 2423 K and 1723 K is compared in figure 7.6 where the calibrated correlated Debye-Waller factors, $< \mu^2_{Al-O} >$, are used. The $< \mu^2_{Al-O} >$ for l-Al_2O_3 from experiment rises with temperature approximately at the same rate predicted by the Debye model using the value of v_l and v_t taken from inelastic X-ray scattering [66] and the atomic value V taken from density measurement (section 4.5). The large difference compared to crystalline alumina is due to the difference in density and speed of sound related to the atomic configurations.

7.4 Conclusion

Using structure factors measured by X-ray diffraction, we have estimated the relative Debye-Waller factors of molten and supercooled liquid alumina. Applying correlated motion theory [62], experimental values have been calibrated by the Debye-Waller factor for liquid alumina at the crystallisation temperature 1723 K. These values are also compared with crystalline, molten and supercooled liquid alumina in the Debye model. Measured correlated $< \mu^2_{Al-O} >$ values fit well with the Debye model for liquid and are significantly higher than for crystalline alumina.

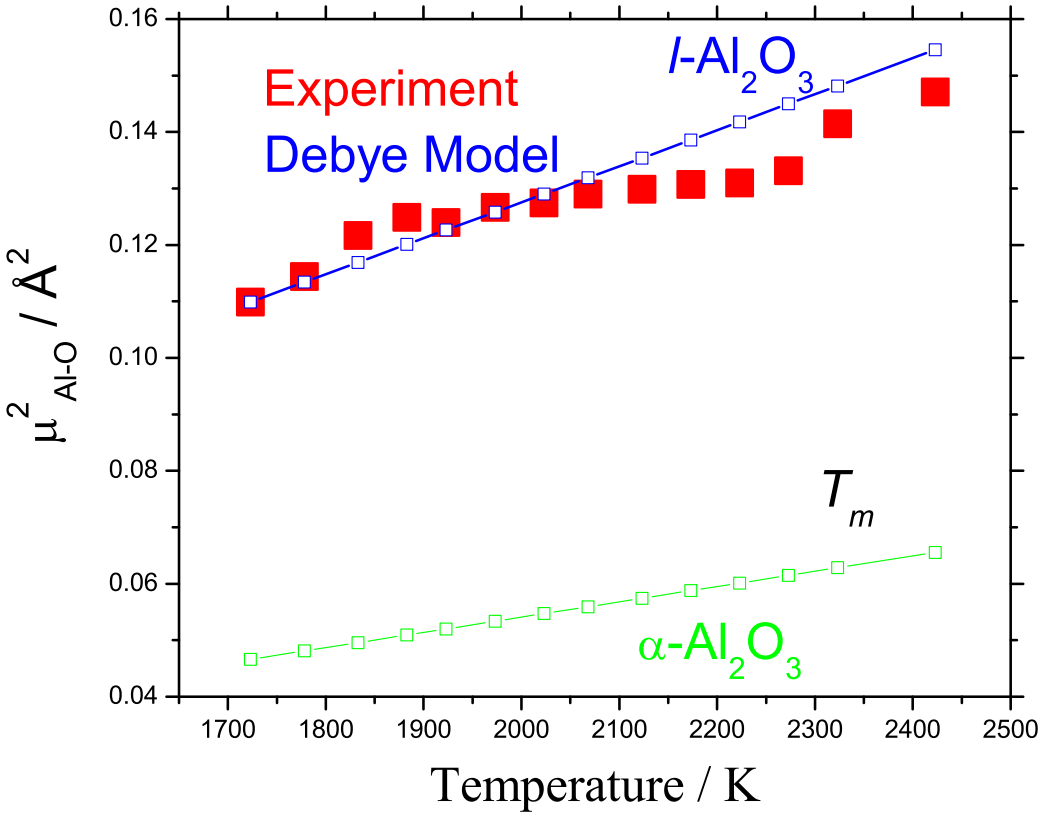

Figure 7.6: Measured relative Debye-Waller factor versus T for molten and supercooled liquid alumina and $\alpha - Al_2O_3$ compared to Debye model values.

Chapter 8

Conclusion and Further Work

8.1 Conclusion

In this work, we have explored and developed *in situ* experiments using our aerodynamic levitator combined with X-ray scattering to characterise dynamical, rheological and thermal properties of molten and supercooled liquid alumina. The density of alumina has been measured in both solid and liquid state through high-speed camera imaging with a good agreement with the literature in the molten and supercooled range of temperature. Our temperature range in supercooled liquid has reached down to 1910 K, close to the recalescence point. Below this point, the sharp rise in temperature has been used to obtain the enthalpy of crystallisation, $102 \pm 6\,kJmol^{-1}$, less than the enthalpy of fusion $111.4\,kJmol^{-1}$. We have also used the high-speed camera to record sample images while exciting the sample by variable frequency acoustic waves. This has enabled the viscosity of sample drops to be measured at different temperatures and to compare liquid alumina with other liquids using the Angell plot. The present viscosity measurements are in agreement with literature values at the melting point and extend into the supercooled region. The Tamann-Vogel-Fulcher analysis points to a fragility of $m \approx 180$. The surface tension is however lower than expected at lower temperatures. This might be due to the synchronisation between the high-speed camera and the frequency generator.

Small-angle X-ray scattering has been used to detect the inhomogeneity in molten and

supercooled liquid alumina. The results are also compared with yttrium aluminates that have been investigated independently in our group. The degree of density fluctuations exhibits linearity of the SAXS signal plotted as $\log I_{SAXS}$ *vs* Q^2 over a limited range of Q. This linearity in liquid alumina is less obvious, however, than in yttrium aluminates and also in silica liquid. Plotted as $\int I_{SAXS} Q^2 dQ$ versus T, there is an increase with temperature for liquid alumina and the increase is greater than for yttrium aluminates.

From the structure factor measurements in wide-angle X-ray scattering, relative correlated Debye-Waller factors of molten and supercooled liquid alumina have been estimated. If one of these values is known, the rest can be calibrated. We have returned to the Debye model, where the atomic motions are approximately harmonic, and used density and speed of sound to calculate the mean-square displacement of the average atom. Using the results of correlated motion theory, the correlated Debye-Waller factors have been calculated. These values are then used to calibrate the relative values from measurements. The slope in experimental values with temperature fits with the Debye-Waller model.

8.2 Future work

The thermal and rheological properties such as density, viscosity and surface tension of alumina as well as other oxide liquids can be done using our sample imaging methods that have been demonstrated during the course of these experiments. This should add significantly to the whole picture of refractory material properties in the molten and supercooled states. In the future we would hope to measure viscosity and surface tension over a wider range of temperature to assist the statistic of TVF analysis, as well as to examine other liquids. Further investigations should also focus on the relation between the Debye-Waller factor and density fluctuations in the liquid state. Our ambition is to develop a full understanding of the relation between the thermal, rheological and dynam-

ical properties of glass-forming liquids with the structural and dynamical properties of their glass counterparts. It will also be useful to develop a new design for the aerodynamic levitator that will enable properties of new materials of low melting point, such as polymer or biological materials, to be investigated.

Publications

Papers:

1. V. Cristiglio, G. J. Cuello, I. Pozdnyakova, M. R. Johnson, H. E. Fisher, D. Zanghi, **Q. Vu Van**, M. C. Wilding, G. N. Greaves and D. L. Pride. Structural of molten yttirum aluminates: a neutron diffraction study. *Journal of Physics: Condensed Matter*, 19:415105 (41pp), 2007.

2. G. N. Greaves, M. C. Wilding, S. Fearn, D. Langstaff, F. Kargl, **Q. Vu Van**, L. Hennet, I. Pozdnyakova, O. Majérus, R. J. Cernik, and C. M. Martin. *In situ* structural studies of alumina during melting and freezing. *Advances in Synchrotron Radiation*, (in press 2008).

3. G. N. Greaves, M. C. Wilding, S. Fearn, D. Langstaff, F. Kargl, S. Cox, **Q. Vu Van**, O. Majérus, C. J Benmore, R. Weber, C. M Martin, L. Hennet. *In situ* Detection of the variables defining first order liquid-liquid phase transitions. *Science*, (under review 2008).

Conferences:

1. **Q. Vu Van**, G. N. Greaves, M. C. Wilding, S. Fearn, C. M. Martin. The thermal disorder and melting in supercooled alumina. *SRMS-5, Chicago July 2006* (Poster contribution).

2. G. N. Greaves, M. C. Wilding, **Q. Vu Van**, O. Majérus, L. Hennet. Characterising density fluctuations in liquid yttria aluminates with small-angle X-ray scattering. *SRMS-6, Brasil July 2008* (Oral contribution).

Bibliography

[1] W. H. Zachariasen. The atomic arrangement in glass. *J. Amer. Chem. Soc*, 54:3841–3851, 1932.

[2] G. N. Greaves. EXAFS and the structure of glass. *J. Non-Cryst Solids*, 71:203–217, 1985.

[3] A. Einstein. *Ann.Physik*, 22:180, 1907.

[4] R. Bohmer and C. A. Angell. *Disorder Effects on Relaxational Processes*. Springer-Verlag, Berlin, 1994.

[5] M. Wilding, P. F. McMillan, and A. Navrotskyc. Thermodynamic and structural aspects of the polyamorphic transitioninyttrium and other rare-earth aluminate liquids. *Physica A*, 314:379–390, 2002.

[6] T. Ishikawa, P. F. Paradis, T. i Itam, and S. Yoda. Non-contact thermophysical property measurements of refractory metals using an electrostatic levitator. *Meas. Sci. Technol*, 16:443–451, 2005.

[7] D. Holland-Moritz, T. Schenk, P. Convert, T. Hansen, and D. M. Herlach. Electromagnetic levitation apparatus for diffraction investigations on the short-range order of undercooled metallic melts. *Meas. Sci. Technol*, 16:372–380, 2005.

[8] A. Kavourasa and G. Krammer. Ultrasonic levitation for the examination of gas/solid reactions. *Rev. Sci. Instrum*, 74:4468–4473, 2003.

[9] C. C. Tang, C. M. Martin, D. Laundy, S. P. Thompson, G. P. Diakun, and R. J. Cernik. X-ray beam characteristics on MPW6.2 at the SRS. *Nucl. Instr. And Meth. B*, 222:659–666, 2004.

[10] G. N. Greaves. Glass in class. *Physics Education*, 40:422–429, 2005.

[11] P. Aldebert and J. P. Traverse. α-Al_2O_3: A high-temperature thermal expansion standard. *High Temperatures - High Pressures*, 16:127–135, 1984.

[12] B. Glorieux, F. Millot, R. C. Riffler, and J. P. Coutures. Density of superheated and undercooled liquid alumina by a contactless method. *International Journal of Thermophysics*, 20:1805–1094, 1999.

[13] P. F. Paradis, T. Ishikawa, and S. Yoda. Non-contact property measurements of liquid and supercooled ceramics with a hybrid electrostatic-aerodynamic levitation furnace. *Meas. Sci. Technol*, 16:452–456, 2005.

[14] G. N. Greaves and S. Sen. Inorganic glasses, glass-forming liquids and amorphizing solids. *Advances in Physics*, 56:1–166, 2007.

[15] R. Bruning, C. Levelut, A. Faivre, R. LeParc, J. P. Simon, F. Bley, and J. L. Hazemann. Characterization of the glass transition in vitreous silica by temperature scanning small-angle x-ray scattering. *Europhys.Lett*, 70:211–217, 2005.

[16] G.N. Greaves, M.C. Wilding, S. Fearn, L. Hennet, and R. Weber. 2008 (in preparation).

[17] G. N. Greaves, M. C. Wilding, S. Fearn, D. Langstaff, F. Kargl, Q. Vu Van, L. Hennet, I. Pozdnyakova, O. Majerus, R. J. Cernik, and C. Martin. *in situ* structural studies of alumina during melting and freezing. *Advances in Synchrotron Radiation*, (in press 2008).

[18] W. Kauzmann. The nature of the glassy state and the behavior of liquids at low temperatures. *Chem. Rev*, 43:219–256, 1948.

[19] J. M. Ziman. *Principles of the theory of solids*. Cambridge University Press, 1969.

[20] F. A. Lindemann. *Z. Phyzik*, 11:609, 1910.

[21] L.D. Landau and E.M. Lifshitz. *Statistical Physics*. Addison-Wesley, Reading MA, 1969.

[22] M. Tomozawa and R. H. Doremus, editors. *Treatise on materials science and technology*. Academic press, NY, 1977.

[23] W. K. Rhim, M. Collender, M. T. Hyson, W. T. Simms, and D. D. Elleman. Development of an electrostatic positioner for space material processing. *Rev. Sci. Instrum*, 56:307–317, 1985.

[24] A. J. Rulison, J. L. Watkins, and B. Zambrano. Electrostatic containerless processing systemrulison97els. *Rev. Sci. Instrum*, 68:2856–2863, 1997.

[25] P. F. Paradis and W. K. Rhim. Thermophysical properties of zirconium at high temperature. *J. Mater. Res*, 14:3713–3719, 1999.

[26] P. F. Paradis and W. K. Rhim. Non-contact measurements of thermophysical properties of titanium at high temperature. *J. Chem. Thermodyn*, 32:123–133, 2000.

[27] W. K. Rhim, S. K. Chung, A. J. Rulison, and R. E. Spjut. Measurements of thermophysical properties of molten silicon by a high-temperature electrostatic levitator. *Int. J. Thermophys*, 18:459–469, 1997.

[28] W. K. Rhim and T. Ishikawa. Thermophysical properties of molten germanium measured by a high-temperature electrostatic levitator . *Int. J. Thermophys*, 21:429–443, 2000.

[29] S. K. Chung, D. B. Thiessen, and W. K. Rhim. A non-contact measurement technique for the density and thermal expansion coefficient of solid and liquid materials. *Rev. Sci. Instrum*, 67:3175–3181, 1996.

[30] A. J. Rulison and W. K. Rhim. A non-contact measurement technique for the specific heat and total hemispherical emissivity of undercooled refractory materials. *Rev. Sci. Instrum*, 65:695–700, 1994.

[31] W. K. Rhim, K. Ohsaka, and P. F. Paradis. Non-contact technique for measuring surface tension and viscosity of molten materials using high temperature electrostatic levitations. *Rev. Sci. Instrum*, 70:2796–2799, 1999.

[32] W. K. Rhim and T. Ishikaw. Non-contact electrical resistivity measurement technique for molten metals. *Rev. Sci. Instru*, 69:3628–3633, 1998.

[33] G. Lohöfer. Electrical resistivity measurement of liquid metals. *Meas. Sci. Technol*, 16:417–425, 2005.

[34] C. Notthoff, H. Franz, M. Hanfland, D. M. Herlach, D. Holland-Moritz, and W. Petry. Electromagnetic levitation apparatus for investigations of the phase selection in undercooled melts by energy-dispersive x-ray diffraction. *Rev. Sci. Instru*, 71:3791–3796, 2000.

[35] E. H. Trinh and C. J. Hsu. Acoustic levitation methods for density measurements. *J. Acoust. Soc. Am*, 80:1757–1761, 1986.

[36] A. Biswas. Solidification of acoustically levitated o-terphenyl crystals: a raman study. *J. Cryst. Growth*, 147:155–164, 1995.

[37] S. Ansell, S. Krishnan, J. K. R. Weber, J. J. Felten, P. C. Nordine, M. A. Beno, D. L. Price, and M. L. Saboungi. Structure of liquid aluminum oxide. *Phys. Rev. Lett*, 78:464 – 466, 1997.

[38] C. Landron, X. Launay, J. C. Rifflet, P. Echegut, Y. Auger, D. Ruffier, J. P. Coutures, M. Lemonier, M. Gailhanou, M. Bessiere, D. Bazin, and H. Dexpert. Development of a levitation cell for synchrotron radiation experiments at very high temperature. *Phys. Res. B*, 124:627–632, 1997.

[39] C. Landron, L Hennet, J. P. Coutures, T. Jenkins, C. Aletru, N. Greaves, A. Soper, and G. Derbyshire. Aerodynamic laser-heated contactless furnace for neutron scattering experiments at elevated temperatures. *Rev. Sci. Instrum*, 71:1745–1751, 1999.

[40] A. Guinier and G. Fournet. *Small-angle scattering of X-rays*. John Wiley & Sons, Inc. New York, 1955.

[41] H. Lamb. *Hydrodynamics*. Cambridge University Press, Cambridge, 1932.

[42] I. Egry, G. Lohöfer, and G. Jacobs. Surface tension of liquid metals: Results from measurements on ground and in space. *Phys. Rev. Lett*, 75:4043–4046, 1995.

[43] M. Perez, L. Salvo, and M. Suery. Contactless viscosity measurement by oscillations of gas-levitated drops. *Phys. Rev. E*, 61:2669–2675, 2000.

[44] L. Rayleigh. On the capillary phenomena of jets. *Proc. R. Soc*, 29:71–97, 1879.

[45] B. Glorieux, F. Millot, and J. C. Rifflet. Surface tension of liquid alumina from contactless techniques. *Int. J. Thermophys*, 23:1249–1257, 2002.

[46] G. Urbain. Vicosite de l'alumine liquide. *Rev. Int. Hautes Temp. Refract. Fr*, 19:55–57, 1982.

[47] YAG viscosity values obtained from M. Wilding (private conversation).

[48] W. Götze. *Liquids, Freezing and Glass Transition*. North Holland, Amsterdam, 1991.

[49] W. Götze and M. Sperl. Logarithmic relaxation in glass-forming systems. *Phy. Rev. E*, 66:011405 (1–17), 2002.

[50] T. Scopigno, G. Ruocco, F. Sette, and G. Monaco. Is the fragility of a liquid embedded in the properties of its glass. *Science*, 302:849–852, 2003.

[51] C. Levelut, A. Faivre, R. LeParc, B. Champagnon, J. L. Hazemann, C. David, L.and Rochas, and J. P. Simon. Influence of thermal aging on density fluctuations in oxide glasses measured by small-angle x-ray scattering. *Journal of Non-Crystalline Solids*, 307:426–435, 2002.

[52] J. Zarzycki. *Glasses and the Vitreous State*. Cambridge University Press, 1991.

[53] G.N. Greaves, M.C. Wilding, F. Kargl, L. Hennet, and O. Majérus. Liquids, glasses, density fluctuations and low frequency modes. *Advanced Materials Research*, 39-40:3–12, 2008.

[54] P. F. McMillan, M. Wilson, M. C. Wilding, D. Daisenberger, M. Mezouar, and G. N. Greaves. Polyamorphism and liquid–liquid phase transitions: challenges for experiment and theory. *Journal of Physics: Condensed Matter*, 19(41):415101 (41pp), 2007.

[55] R. J. Cernik, P. Barnes, G. Bushnell-Wye, A. J. Dent, G. P. Diakun, J. V. Flaherty, G. N. Greaves, E. L. Heeley, W. Helsby, S. D. M. Jacques, J. Kay, T. Rayment,

A. Ryan, C. C. Tang, and N. J. Terrill. The new materials processing beamline at the SRS Daresbury, MPW6.2. *J. Synchrotron. Rad*, 11:163–170, 2004.

[56] W. Brasa, G.E. Derbyshirea, A.J. Ryana, G.R. Manta, A. Feltona, R.A. Lewisa, C.J. Halla, and G.N. Greaves. Simultaneous time resolved saxs and waxs experiments using synchrotron radiation. *Nucl. Instr. and Methods*, 326:587–591, 1993.

[57] V. Sarou-Kanian, J. C. Rifflet, and F. Millot. IR Radiative properties of solid and liquid alumina: Effects of temperature and gaseous environment. *International Journal of Thermophysics*, 26:1263–1275, 2005.

[58] Edward A. Desloge. *Thermal physics.* Holt, Rinehart & Winston, Inc, 1968.

[59] Greaves et al. 2008 (in preparation).

[60] D. R. Lide, editor. *Handbook of chemistry and physics.* CRC Press, 2003-2004.

[61] G. N. Greaves, A. J. Dent, B. R. Dobson, S. Kalbitzer, S. Pizzini, and G. Müller. Environments of ion-implanted As and Ga impurities in amorphous silicon. *Phys. Rev. B*, 45:6517–6533, 1992.

[62] W. Bohmer and P. Rabe. Temperature dependence of the mean square relative displacements of nearest-neighbour atoms derived from exafs spectra. *J. Phys. C*, 12:2465–2474, 1979.

[63] S. R. Elliott. *Physics of amorphous materials.* Longman Sience and Tech; 2 Sub edition, 1990.

[64] D. E. Sayers, E. A. Stern, and F. W. Lytle. New method to measure structural disorder: Application to GeO_2 glass. *Phys. Rev. Lett*, 35(9):584–587, Sep 1975.

[65] O. L. Anderson. *Equations of stat of solids for geophysics and ceramic science*. Oxford University Press, 1995.

[66] H. Sinn, B. Glorieux, L. Hennet, A. Alatas, M. Hu, E. E. Alp, F. J. Bermejo, D. L. Price, and M. L. Saboungi. Microscopic dynamics of liquid aluminum oxide. *Science*, 299:2047–2049, 2003.

[67] C. Landron, L. Hennet, T. E. Jenkins, G. N. Greaves, J. P. Coutures, and A. K. Soper. Liquid alumina: Detailed atomic coordination determined from neutron diffraction data using empirical potential structure refinement. *Phys. Rev. Lett*, 86(21):4839–4842, May 2001.

[68] Additionally a correction should also be made for the curvature of the sample as the emissivity is obtained for a flat geometry. This can be accomodated by a small addition to the calibrated temperature scale.

[69] A.K. Soper. Empirical potential Monte Carlo simulation of fluid structure. *Chem. Phys* 202: 295-306, 1996

[70] C.A Catlow and G.N Greaves. Application of Synchrotron radiation. Blackie (Glasgow and London), 1990.

[71] http://physics.nist.gov/PhysRefData/FFast/html/form.html